UNIVERSITY OF CALIFORNIA, SAN DIEGO

Symmetry Breaking and Synchronization at Small Scales

A dissertation submitted in partial satisfaction of the
requirements for the degree
Doctor of Philosophy

in

Engineering Sciences (Mechanical Engineering)

by

Gwynn J. Elfring

Committee in charge:

Professor Eric Lauga, Chair
Professor Jurijs Bazilevs
Professor John F. Brady
Professor Alison Lesley Marsden
Professor Stefan G. Llewellyn Smith
Professor William Roy Young

2012

The dissertation of Gwynn J. Elfring is approved, and it is acceptable in quality and form for publication on microfilm and electronically:

_____

_____

_____

_____

_____

_____
Chair

University of California, San Diego

2012

DEDICATION

To my mother.

EPIGRAPH

I gaped into the bleakness of my own days;
I had an awful long way to go too.
—Jack Kerouac

TABLE OF CONTENTS

ACKNOWLEDGEMENTS

First of all I'd like to thank my advisor Eric Lauga. I have loved every moment of my Ph.D. and that is in large part due to him. He is an extraordinary scientist, mentor, friend and person. Eric is who I want to be when I grow up.

I'd like to thank all my committee members for agreeing to guide me on this journey and to spend time with my ponderous work. All of them are scientists I deeply respect and admire.

I'd like to thank all the officemates I've had the utter pleasure of sharing my long days with. Foremost among them, my very good friend On Shun Pak, with me from the start to the end, through all the ups and downs. Talking with On Shun about science has been one of the great joys of my life and I'll miss it dearly. Also, Dr. Art Evans and Dr. Saverio Spagnolie, who have now gone but are still good friends. I looked at them in awe when I first arrived at UCSD and I still do, but for manifold reasons. Now that I realize how foolish my questions once were I admire them even more. And lately, my newer officemates Greg Wagner and Man Yi for allowing me that senior sage feeling and Dr. Mario Sandoval and Dr. Rodrigo Vélez for reminding me of home. Finally, all the members of Team France for teaching me to be young again.

I'd like to thank my MAE 107 class for surviving me teaching and writing my dissertation at the same time.

I'd also like to thank my old friends who chose similarly to pursue an academic life, Simmer, Brendan and Derek, for giving me an outlet and for not letting me be the only starving and unemployed one in the group.

I thank all my friends and family (old and new) for being proud of me.

Finally I thank my wife Tracy, for everything... for happiness.

Chapter 3, in part, is a reprint of the material as it appears in Physical Review Letters 2009. Elfring, Gwynn J.; Lauga, Eric, the American Physical Society, 2009. The dissertation author was the primary investigator and author of this paper.

Chapter 3, in part, is a reprint of the material as it appears in Physics of Fluids 2011. Elfring, Gwynn J.; Lauga, Eric, the American Institute of Physics, 2011. The dissertation author was the primary investigator and author of this paper.

Chapter 5, in part, is a reprint of the material as it appears in the Journal of Fluid Mechanics 2011. Elfring, Gwynn J.; Lauga, Eric, Cambridge University Press, 2011. The dissertation author was the primary investigator and author of this paper.

Chapter 6, in small part, is a reprint of the material as it appears in the Journal of Fluid Mechanics 2010. Elfring, Gwynn J.; Pak, On Shun; Lauga, Eric, Cambridge University Press, 2010. The dissertation author was the primary investigator and author of this paper.

Chapter 7, in part, is a reprint of the material as it appears in the Journal of Fluid Mechanics 2010. Elfring, Gwynn J.; Pak, On Shun; Lauga, Eric, Cambridge University Press, 2010. The dissertation author was the primary investigator and author of this paper.

Chapter 8, in part, is a reprint of the material as it appears in Physics of Fluids 2012. Elfring, Gwynn J.; Lauga, Eric, the American Institute of Physics, 2012. The dissertation author was the primary investigator and author of this paper.

Chapter 4 and chapter 6 contain the results of ongoing work that is, as of yet, unpublished.

Not appearing in this dissertation, but part of the author's Ph.D. experience was the work published in Physica D entitled "Taylor's Swimming Sheet: Analysis and Improvement of the Perturbation Series" by Sauzade, Martin; Elfring, Gwynn J.; Lauga, E. The dissertation author was a primary investigator and author of this paper.

The author thanks David Woolley for allowing the reproduction of the experimental picture used in this dissertation.

Funding by the NSF (CBET-0746285) and NSERC (PGS D3-374202) and the University of California Kaplan Dissertation Year Fellowship is gratefully acknowledged. The author also acknowledges the tremendous pleasure it was to be a University of California Graduate Teaching Fellow.

VITA

2005	B. Eng. in Mechanical Engineering and Mathematics *with distinction*, University of Victoria
2007	M. A.Sc. in Mechanical Engineering, University of Victoria
2012	Ph. D. in Engineering Sciences, University of California, San Diego

PUBLICATIONS

G.J. Elfring, E. Lauga, "Buckling instability of squeezed droplets", *Physics of Fluids*, **24**, (2012) 072102.

M. Sauzade, G.J. Elfring, E. Lauga, "Taylor's swimming sheet: Analysis and improvement of the perturbation series", *Physica D* **240** (2011) 1567-1573.

G.J. Elfring, E. Lauga, "Synchronization of flexible sheets", *Journal of Fluid Mechanics* **674** (2011) 163-173.

G.J. Elfring, E. Lauga, "Passive hydrodynamic synchronization of two-dimensional swimming cells", *Physics of Fluids* **23** (2011) 011902

G.J. Elfring, O.S. Pak, E. Lauga, "Two-dimensional flagellar synchronization in viscoelastic fluids", *Journal of Fluid Mechanics*, **646** (2010) 505-515.

G.J. Elfring, E. Lauga, "Hydrodynamic phase locking of swimming microorganisms", *Physical Review Letters*, **103** (2009) 088101. (Editors' Suggestion)
-also selected for Virtual Journal of Biological Physics Research (August 15 2009).

G.J. Elfring, H. Struchtrup, "Thermodynamics of pore wetting and swelling in Nafion", *Journal of Membrane Science*, **315** (2008) 125-132.

H. Struchtrup, G.J. Elfring, "External losses in high-bypass turbo fan air engines", *Int. Journal of Exergy*, **5** (2008) 400-412.

G.J. Elfring, H. Struchtrup, "Thermodynamic considerations on the stability of water in Nafion", *Journal of Membrane Science*, **297** (2007) 190-198.

ABSTRACT OF THE DISSERTATION

Symmetry Breaking and Synchronization at Small Scales

by

Gwynn J. Elfring

Doctor of Philosophy in Engineering Sciences (Mechanical Engineering)

University of California, San Diego, 2012

Professor Eric Lauga, Chair

This thesis is devoted to the theoretical description of two experimentally observed phenomena which occur at small scales.

We first address the synchronization of swimming microorganisms. Motile microorganisms swim in a fluid regime where inertia is unimportant and viscous stresses dominate. In this limit the flow field due to a swimmer affects the motility of nearby cells, a fact which is biologically important as microorganisms such as spermatozoa are often found in high-density suspensions. A particular consequence of these fluid-based interactions is the synchronization of the flagella of some microorganisms, and in particular spermatozoa, observed to occur when these cells are swimming in close proximity. Using theoretical analysis it is demonstrated that

two infinite sheets passing waves of a prescribed shape, will not synchronize in a Newtonian fluid if the shape of the waveforms has sufficient symmetry because of the kinematic reversibility of the Stokes equations. The sinusoidal waveforms of Taylor's swimming sheet fall into this category, and will thus not dynamically synchronize in a Newtonian fluid. It has been observed that excess symmetry similarly curbs synchronization in other models. For a sinusoidal sheet, a geometric perturbation must therefore be added to break the necessary front/back symmetry, and give rise to a time-evolution of phase toward the synchronized state. Alternatively, instead of a geometric symmetry-breaking, it is also shown that synchronization can occur if the kinematic reversibility of the field equations is removed, as is the case for a viscoelastic fluid. In such a scenario the phase always evolves to a stable in-phase conformation where the energy dissipated by the swimmers is minimized. Finally it is shown that finite size effects act to bring swimmers closer together and then we show in this regime that elastic deformations caused by fluid structure interactions play a dominant role in synchronization dynamics.

Additionally, motivated by recent experiments, we consider theoretically the compression of droplets pinned at the bottom on a surface of finite area. We show that if the droplet is sufficiently compressed at the top by a surface, it will always develop a shape instability at a critical compression. When the top surface is flat, the shape instability occurs precisely when the apparent contact angle of the droplet at the pinned surface is π, regardless of the contact angle of the upper surface, reminiscent of past work on liquid bridges and sessile droplets as first observed by Plateau. Past the critical compression, the droplet transitions from a symmetric to an asymmetric shape. The force required to deform the droplet peaks at the critical point then progressively decreases indicative of catastrophic buckling. We characterize the transition in droplet shape using illustrative examples in two dimensions followed by perturbative analysis as well as numerical simulation in three dimensions. When the upper surface is not flat, the simple apparent contact angle criterion no longer holds, and a detailed stability analysis is carried out to predict the critical compression.

Chapter 1

Introduction

As the title of this dissertation suggests we investigate here two beautiful physical events, synchronization and symmetry breaking, in fluids at small scales, and demonstrate how they can be intimately correlated.

1.1 Why?

An often observed yet surprising physical phenomenon is the synchronization of the pendulums of grandfather clocks. When two such clocks are located in close proximity, forces transmitted through a medium connecting the two clocks can lead to their beating in perfect synchrony [1]. Similar synchronization can easily be obtained at home using two connected metronomes, with spectacular results. Still more fascinating are the many examples of synchrony which occur in the natural world, from pacemaker cells in a heart [2] to synchronously flashing fireflies [3].

One particularly interesting example of synchronization occurring in nature is the observed phase locking of the flagella of swimming eukaryotes such as spermatozoa [5, 6, 7, 4]. These cells, typically tens of microns long, actuate slender flagella beating periodically in order to propel themselves in viscous fluids [8, 9, 10]. As illustrated in Fig. 1.1 in the case of two bull spermatozoa, when two such cells swim in close proximity, their flagella are often observed to beat in synchrony – so much so that in Fig. 1.1C the two flagella cannot even be distinguished [4].

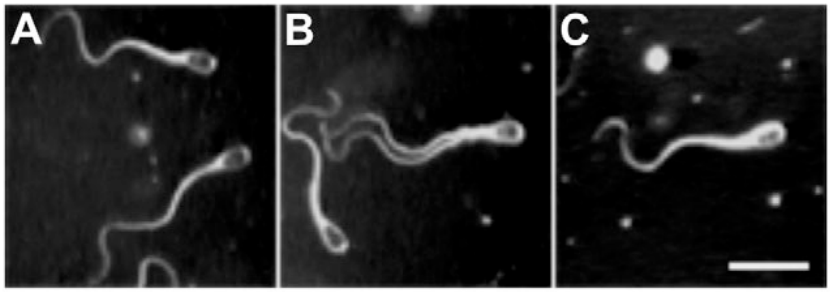

Figure 1.1: (A to C) Time-sequence showing the synchronization of two swimming bull spermatozoa. Scale bar is $25\mu m$. Reproduced / adapted with permission from Woolley et al. [4].

This synchronization is biologically significant because it is observed to lead to an increased swimming speed for the co-moving cells, thereby providing a competitive advantage over cells which are not synchronized [11, 4]. This behavior can arise purely passively, as is the case with the pendulums, but here the medium transmitting the forces is the fluid between the cells.

This interaction between the two cells through the fluid is a very rich event. In particular, what we demonstrate is how symmetry in the shapes of the swimmers is intimately correlated with the evolution of the system to a synchronized state. Too much symmetry and no relative motion can occur at all. Yet nature provides many intrinsic symmetry breaking mechanisms which we investigate here, from the front/back asymmetry provided by the genetic payload, to memory effects of polymers in the fluid.

Finally we conclude this dissertation by investigating how droplets, which we very often find with rotational symmetry, can become asymmetric when compressed. The fascinating result is that the mechanical properties of the droplet can be completely altered by such a symmetry-breaking transition and, in cases of squeezed droplets, can lead to buckling type events.

1.2 How?

This dissertation is divided between the study of the synchronization of swimming microorganisms in chapters 2–7, while symmetry breaking and buckling

of droplets is discussed in chapter 8.

The section on sychronization is organized as follows:

- In chapter 2, we present a brief introduction to the fundamentals of Stokes flow used throughout the rest of this thesis.

- In chapter 3, using a simplified model (two infinite, parallel, two-dimensional waving sheets), we show that phase-locking arises from hydrodynamic forces alone, and has its origin in the front-back asymmetry of the geometry of their flagellar waveform. The time-evolution of the phase difference between co-swimming cells depends only on the nature of this geometrical asymmetry, and microorganisms can phase-lock into conformations which minimize or maximize energy dissipation.

- In chapter 4 we explore finite size effects by introducing a three-dimensional model for swimming microorganisms. Finite size effects are shown to yield synchronizing fields. However, we find that attractive dipole interactions dominate the dynamics and force the organisms together on time scales much faster than the evolution of the phase.

- In chapter 5 we inquire about a physical mechanism responsible for symmetry-breaking in nature. Returning to a two-dimensional model, we demonstrate that flexible sheets with symmetric internal forcing deform when interacting with each other via a thin fluid layer in such a way as to systematically break the overall waveform symmetry, thereby always evolving to an in-phase conformation where energy dissipation is minimized. This dynamics is shown to be mathematically equivalent to that obtained for prescribed waveforms in viscoelastic fluids, emphasizing the crucial role of elasticity in symmetry-breaking and synchronization.

- Motivated by the fact that most biological fluids possess a polymeric microstructure, chapter 6 serves to introduce non-Newtonianian fluids and presents a few extensions to established results for swimming in viscoelastic fluids.

- In chapter 7 we address synchronization in a viscoelastic fluid analytically. Using a two-dimensional infinite sheet model we show that the presence of polymeric stresses removes the geometrical asymmetry constraint, and therefore even symmetric swimmers synchronize. Such synchronization occurs on asymptotically faster time scales than in a Newtonian fluid, and the swimmers are seen to be driven into a stable in-phase conformation minimizing the energy dissipated in the surrounding fluid.

Finally we conclude the dissertation with a brief foray into the world of small droplets.

- In chapter 8, we address theoretically the experimentally observed buckling instability of pinned droplets. We demonstrate that a pinned droplet compressed by a flat surface will always develop a shape instability if sufficiently compressed, regardless of the contact angle of the upper surface. The transition from axisymmetry to asymmetry is also shown to yield the onset of a catastrophic buckling instability.

Chapter 2

Stokes flow

Everything in this dissertation can be considered very small. We are concerned with swimming microorganisms whose length scales are typically on the order of microns, in a regime where inertia plays no role and likewise we are interested in droplets small enough that gravity plays no role.

If we non-dimensionalize the Navier-Stokes equations by a typical length scale L, and velocity scale U, we obtain

$$\mathrm{Re}\frac{D\mathbf{u}^*}{Dt^*} = -\frac{L}{\mu U}\boldsymbol{\nabla}^* p + \nabla^{*2}\mathbf{u}^*, \tag{2.1}$$

where $\mathbf{u}$ is the velocity field p is the pressure field. The Reynolds number $\mathrm{Re} = \rho U L/\mu$ is the ratio of the inertial terms to the viscous terms (*'s indicate dimensionless terms). When the length scale is very small (and typically for microogranisms the swimming speed is roughly on the order of a body length per second and so also very small) a vanishing Reynolds number indicates the lack of import of the inertial terms. In the zero Reynolds number limit we have hence no inertial terms.

To gain further insight we look at the Green's function for Stokes flow. For a singularly forced flow we may write

$$\boldsymbol{\nabla}\cdot\boldsymbol{\sigma} = -\boldsymbol{\nabla}p + \mu\nabla^2\mathbf{u} = -\mathbf{F}^e\cdot\delta(\mathbf{x}), \tag{2.2}$$

where $\boldsymbol{\sigma}$ is the stress tensor, $\mathbf{F}^e$ is a force on the fluid (conveniently centered at the origin, else $\mathbf{x}\to(\mathbf{x}-\mathbf{x}_0)$). We use here an e to denote force on the fluid as later we will use $\mathbf{F}$ to denote fluid force on a body. Finally we mention that we will use

lower case to denote force density while upper case for force, related by $\mathbf{F} = \int_S \mathbf{f} dS$.

The resulting flow field from (2.2) is

$$\mathbf{u} = \frac{1}{8\pi\mu}\mathbf{G}\cdot\mathbf{F}^e \tag{2.3}$$

where the tensor $\mathbf{G}$ is known as the Stokeslet and given by

$$\mathbf{G}(\mathbf{x}) = \frac{\mathbf{I}}{|\mathbf{x}|} + \frac{\mathbf{xx}}{|\mathbf{x}|^3}\ . \tag{2.4}$$

Another singular solution is obtained by taking the Laplacian of the Stokeslet. We obtain $\mathbf{D} = \frac{1}{2}\nabla^2\mathbf{G}$ which is a potential dipole and

$$\mathbf{D}(\mathbf{x}) = \frac{\mathbf{I}}{|\mathbf{x}|^3} - 3\frac{\mathbf{xx}}{|\mathbf{x}|^5}, \tag{2.5}$$

and $\mathbf{u} = \mathbf{D}\cdot\mathbf{\Gamma}/8\pi\mu$ is the flow due to the potential dipole of strength $\mathbf{\Gamma}$.

The sum of a Stokeslet and a potential dipole occurs frequently. Hence we write

$$\mathbf{S}(\mathbf{x};\beta) = \mathbf{G}(\mathbf{x}) + \beta\mathbf{D}(\mathbf{x}). \tag{2.6}$$

The flow due to a sphere of radius a centered at $\mathbf{x}_0$ pulled by an external force $\mathbf{F}^e$ through an otherwise quiescent field is given by $\mathbf{u} = \frac{1}{8\pi\mu}\mathbf{S}(\mathbf{x}-\mathbf{x}_0, \frac{a^2}{3})\cdot\mathbf{F}^e$.

One might also be tempted to take the curl of the Stokeslet. If we do so we obtain the rotlet $\mathbf{\Omega} = \frac{1}{2}\boldsymbol{\nabla}\times\mathbf{G} = \epsilon_{ijk}\mathbf{x}_k r^{-3}$. We note the following relation

$$\mathbf{\Omega}\cdot\mathbf{T}^e = \mathbf{T}^e \times \frac{\mathbf{x}}{|\mathbf{x}|^3}. \tag{2.7}$$

The flow $\mathbf{u} = \mathbf{\Omega}\cdot\mathbf{T}^e/8\pi\mu$ is that which results in a point torque of strength $\mathbf{T}^e$ at the origin. Note that $\boldsymbol{\nabla}\times\mathbf{D} = \frac{1}{2}\nabla^2\boldsymbol{\nabla}\times\mathbf{G} = \nabla^2\mathbf{\Omega} = \mathbf{0}$ because the vorticity field of a Stokes flow is harmonic and $\nabla^2\mathbf{D} = \frac{1}{2}\nabla^4\mathbf{G} = \mathbf{0}$ because the velocity field is biharmonic. Finally note that $\boldsymbol{\nabla}\times\mathbf{\Omega} = \frac{1}{2}\boldsymbol{\nabla}\times\boldsymbol{\nabla}\times\mathbf{G} = \frac{1}{2}\boldsymbol{\nabla}\boldsymbol{\nabla}\cdot\mathbf{G} - \frac{1}{2}\nabla^2\mathbf{G} = -\mathbf{D}$.

Chapter 3

Synchronization of swimming sheets

3.1 Introduction

Large systems of many interacting bodies are often too complicated to address rigorously, and idealizations such as the Kuramoto model [12] must be employed from the start. In contrast, in this chapter we investigate a very simple model for a pair of co-swimming cells. Namely we consider them to be two-dimensional and infinite sheets. The simplicity of the model allows us to solve for the interactions via the fluid field exactly, both analytically and numerically. We ultimately find the occurrence of passive hydrodynamic synchronization for all but the most symmetric flagellar waveforms.

G.I. Taylor first studied synchronizing flagellated cells by modeling them as two-dimensional sheets propagating sinusoidal waves of transverse displacement [13]. With this model, he found that, for a given swimming gait, swimming in-phase synchronously is the conformation in which the cells swim while doing the least amount of work against the surrounding fluid. Left open was the question of whether the synchronization would occur passively from a random initial phase shift between co-swimming cells. Subsequent numerical works using an immersed boundary method and multiparticle collision dynamics seem to indicate that indeed

synchronization could occur due to hydrodynamic forces alone [14, 15, 7].

The phase locking of flagellated microorganisms is closely related to another important observed synchrony in nature, that of eukaryotic cilia. Cilia are short flagella typically lining the surface of a larger body and are found to beat in unison with a small constant phase difference giving rise to a collective motion described as metachronal waves [9]. This motion provides various biological functionality including fluid transport and locomotion [16]. Several models with varying complexity have indicated that the synchronization which manifests as metachronal beating can occur due to fluid forces alone [17, 18, 19, 20] although, since individual cilia are not free-swimming but are attached to a substrate, synchronization can only occur with a load-dependent force generation. Similarly to cilia, there is an observed synchronization of the pairs of flagella used for propulsion on the alga *Chlamydomonas* [21]. Beyond eukaryotic flagella and cilia, hydrodynamic interactions in bacterial flagella lead to the creation of flagella bundles propelling the cells forward as they swim, as well as the disruption of such bundles when the cells change their swimming direction [22, 23, 24].

In this chapter we return to the two dimensional model first proposed by Taylor (detailed in Sec. 3.2), to describe the phase locking of swimming flagellated cells. The simplicity of such a model allows one to address the problem analytically, to extract the relevant properties that such waves must possess in order to give rise to synchronization, and to determine precisely what states of dynamic equilibrium will occur. We first present geometrical arguments which show that Taylor's purely sinusoidal sheet cannot dynamically synchronize due to an excess of symmetry which, when coupled with the kinematic reversibility of the Stokes equations, prevents any relative motion between free-swimming cells (Sec 3.3). Real flagella possess a front-back asymmetry and we show that this feature leads to the occurrence of synchronization. We accomplish this by allowing the sheets to pass completely general waveforms in our model. We then solve the problem analytically for two asymptotic limits, first when the amplitude of the waves is much smaller than their wavelength (Taylor's limit, Sec. 3.4), and then when the mean distance between the waves is much smaller than the wavelength (lubrica-

tion limit, Sec. 3.5). We also solve the problem numerically using the boundary integral formulation of the Stokes equations to demonstrate the validity of the analytic formulae and to address the synchronization of large-amplitude waveforms (Sec. 3.6).

Our results show precisely how the geometry of the waveforms governs the synchronizing dynamics of the system (Sec. 3.7). We obtain simple formulae that dictate the time-evolution of the phase and the energy dissipation, and which indicate that while swimming in-phase results in a minimum of viscous dissipation it does not necessarily coincide with an equilibrium state, and indeed a dynamically stable state may maximize energy dissipation. In addition to the geometry of the waveforms, we demonstrate the importance of the separation of the sheets on the dynamics of the system. We show that the stable conformations (and the number of them) may change with the distance between the cells. Notably, swimming cells with front-back asymmetry are shown to synchronize into either a stable in-phase or opposite-phase conformation when in close proximity, while some cells when further apart are shown to synchronize with a fixed finite phase difference, reminiscent of ciliary phase locking. A discussion and summary of these results is offered in Sec. 3.8.

3.2 Setup

Our system, as illustrated in Fig. 3.1, consists of two parallel and identical infinite sheets, which we will call swimmers, separated by a mean distance $\bar{h}$. The sheets both propagate waves of transverse displacement in the positive z direction, with amplitude a and speed $c = \omega/k$, where ω is the wave frequency and k is the wavenumber, and have an initial phase difference $\phi_0 = k\Delta z_0$ (denoted positive when the bottom sheet is shifted by ϕ_0 along the positive z direction with respect to the top sheet). By passing these waves the swimmers propel themselves in the $-z$ direction [13]. We consider the frame of reference moving with the bottom sheet, at speed U, and write the relative speed of the top sheet in the z direction as U_Δ.

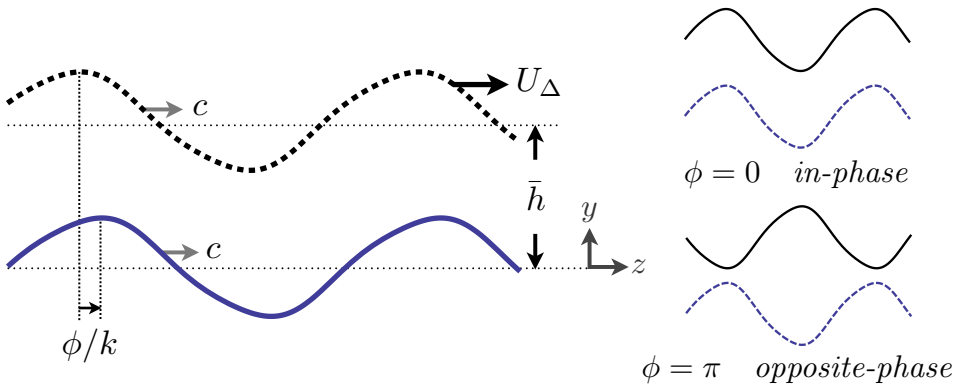

Figure 3.1: System of parallel and identical two-dimensional infinite sheets in a frame moving with the lower sheet. The sheets are separated vertically by a mean distance $\bar{h}$. The top sheet, behind the bottom sheet by a phase ϕ as measured along the z axis, moves to the right with a relative velocity U_Δ.

The instantaneous positions of the bottom (y_1) and top (y_2) sheets are thus given by

$$y_1 = ag\Big(k[x - ct]\Big), \tag{3.1}$$

$$y_2 = \bar{h} + ag\left(k\left[x - ct + \Delta z_0 - \int_0^t U_\Delta(t')dt'\right]\right), \tag{3.2}$$

where g a function describing the arbitrary waveform of the swimmers, and z is the axial coordinate in a frame moving with the lower sheet. We use the following dimensionless variables $x^* = xk$, $t^* = t\omega$, $u^* = u/c$, $v = v/\epsilon c$, with the ratio of the amplitude of the waves to their wavelength given by $\epsilon = ak$. For convenience we use the wave variable $z^* = x^* - t^*$ and the instantaneous phase difference $\phi = \phi_0 - k\int_0^{t^*} U_\Delta^*(t')dt'$. Consequently the positions of the sheets in the moving frame are given simply by

$$y_1^* = \epsilon g(z^*), \tag{3.3}$$

$$y_2^* = \bar{h}^* + \epsilon g(z^* + \phi), \tag{3.4}$$

where the arbitrary 2π-periodic function g can be written using Fourier series as

$$g(z^*) = \sum_{n=1}^{\infty} \alpha_n \cos(nz^*) + \sum_{n=1}^{\infty} \beta_n \sin(nx^*). \tag{3.5}$$

Since we are concerned with the synchronization of microorganisms, we are in a low Reynolds number regime (Re $\sim 10^{-4}$ for the bull spermatozoa in Fig. 1.1)

where the fluid between the sheets is inertia free, and thus mechanical equilibrium for the stress tensor, $\boldsymbol{\sigma}^*$, is written as $\nabla \cdot \boldsymbol{\sigma}^* = \mathbf{0}$. Assuming an incompressible Newtonian flow we obtain the Stokes equations for the dimensionless velocity field, $\mathbf{u}^* = (u^*, v^*)$, and dynamic pressure, $p^* = p\epsilon^2/\mu\omega$, as

$$\nabla^2 \mathbf{u}^* = \nabla p^*, \tag{3.6}$$

$$\nabla \cdot \mathbf{u}^* = 0. \tag{3.7}$$

Physically, if the sheets are not permitted to move relative to one another, i.e. if we set $U_\Delta^* = 0$, then there may arise a horizontal hydrodynamic force F_x acting on the swimmers. Conversely, if we let the sheets move freely under the constraint that they are force free then there may be a nonzero evolution of the phase in time, given geometrically as $U_\Delta^* = -d\phi/dt$. These two problems are of course related, as we will see, by the mobility $\mathcal{M}$, as $U_\Delta = \mathcal{M}F_x$. In the case of a purely sinusoidal swimmer (i.e. $\beta_1 = 1$, $\beta_n = 0$ $n > 1$ and $\alpha_n = 0$ $\forall n$), G.I. Taylor [13] derived the swimming speed of a single sheet (the outer problem) and obtained

$$U^* = -\frac{1}{2}\epsilon^2 \left(1 - \frac{19}{16}\epsilon^2\right) + \mathcal{O}(\epsilon^6). \tag{3.8}$$

In the rest of the chapter we drop the * notation for convenience.

3.3 Symmetry

Before calculating the hydrodynamic forces between the swimmers, it is insightful first to consider the various symmetry properties of the problem, and their consequences on force generation and synchronization.

Suppose first that we have two swimmers, g_1 and g_2, whose shapes are such that g_2 is obtained from g_1 by a vertical axis reflection plus a horizontal axis reflection and a phase shift θ (which depends on the location of the vertical axis), i.e. $g_2(x) = -g_1(-x + \theta)$. In that case there can be no horizontal hydrodynamic force acting between the swimmers, and $F_x = 0$. To prove this result, let us assume that a force $\mathbf{F}$ acts on the top sheet with $U_\Delta = 0$ (since $\nabla \cdot \boldsymbol{\sigma} = 0$ the force on the

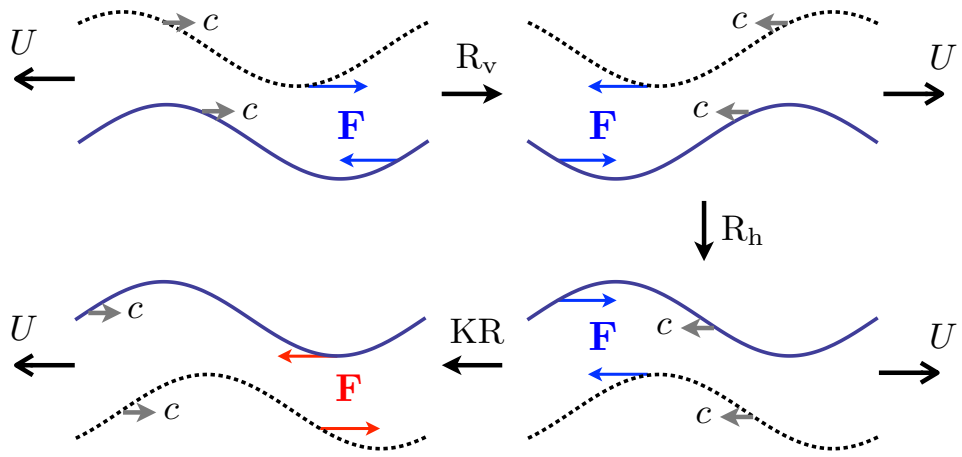

Figure 3.2: A system of two identical and parallel swimmers which has a stabilizing force (top left) becomes destabilizing (bottom left), under two reflections – first about the vertical axis (R_v) then about the horizontal axis (R_h) – combined with an application of kinematic reversibility (KR), yet the boundary conditions remain identical, hence the force must be zero. Symmetric waveforms can thus not synchronize.

bottom sheet must be equal and opposite in sign). We then perform a reflection of the entire conformation about the vertical axis then horizontal axis, followed by a reversal of the kinematics (see Fig. 3.2 for an example). The resulting system is identical except the sign of the force has reversed, $\mathbf{F} \to -\mathbf{F}$, a contradiction unless $\mathbf{F} = 0$ (then $F_x = 0$). In particular, if the sheets are identical, then there can be no synchronization if the identical shapes of the waveforms satisfy $g(x) = -g(-x+\theta)$. A subset of these shapes are sheets that are invariant under both vertical axis reflection $g(x) = g(-x + \theta)$ and horizontal axis reflection $g(x) = -g(x + \pi)$; the simplest example of such shape is a pure sinewave ($\beta_1 = 1$, $\beta_n = 0$ $n > 1$ and $\alpha_n = 0\ \forall n$), which is Taylor's original geometry [13, 14]. Since such an arrangement has both vertical and horizontal axis symmetry it will not passively synchronize in a Stokesian flow [25]. Similar excessive geometrical symmetries have also been observed to curb any phase-locking in other swimmer models [26, 27, 28].

A further generalization of the argument may be obtained by noting that in two dimensions the outer problem can balance no force and hence each side of the swimmer must be force free. This decoupling of the inner and outer problem means that it is only the fluid between the two sheets that drives synchronization,

if any. Thus if two swimmers do not phase-lock, a similar arrangement of more than two swimmers will not either – a result that cannot be obtained by symmetry alone.

In order to possibly obtain a passive synchronization between the swimmers we must therefore either (1) have a geometry such that $g(x) \neq -g(-x+\theta)$, or (2) remove the kinematic reversibility of the flow equations. Since we are considering here microorganisms in a Newtonian fluid, the latter is a property of the problem that we cannot escape. If our model were at finite Reynolds number, or in a viscoelastic fluid, then this constraint would naturally be removed and symmetric swimmers could synchronize [29]. In a Stokesian flow we must thus have a geometrical asymmetry.

Most swimming microorganisms, such as spermatozoa, possess a cell body and thus have a very natural front-back asymmetry. In addition, some spermatozoa pass waves along their flagella which increase in amplitude from head to tail, leading to another type of front-back asymmetry [30]. In contrast, swimmers whose flagellar waveforms or body is asymmetric with respect to the horizontal axis experience viscous torques, and thus cannot swim straight. It is therefore natural for us to focus on waveforms which are symmetric about the horizontal axis, but not the vertical. As a result of this horizontal axis symmetry, the horizontal component of a force between the swimmers must be an odd function of the phase ϕ, $F_x(-\phi) = -F_x(\phi)$, and thus there must always be a fixed point at $\phi = 0$, i.e. $F_x(0) = 0$. In addition, because the force is 2π-periodic, then $\phi = \pi$ must also be another fixed point, i.e. $F_x(\pi) = 0$.

As a side note, we observe that because of the kinematic reversibility of the Stokes equations, a change in the direction of wave propagation yields a reversal of forces $\mathbf{F} \to -\mathbf{F}$. Reversing the direction of wave propagation is geometrically equivalent to reversing the front-back asymmetry of the waveforms which must therefore also reverse the forces on the swimmer.

In order to gain physical intuition in the synchronization process, we now characterize the force generation and subsequent synchronization between the two sheets analytically by focusing on two asymptotic limits. We first consider in

Sec. 3.4 the limit in which the amplitude of the traveling waves is much smaller than their wavelength. The limit in which the distance between the swimmers is much smaller than their wavelength will then be considered in Sec. 3.5. Additionally we solve the problem numerically using the boundary integral formulation of the Stokes equations in Sec. 3.6 to validate our asymptotics and address large-amplitude swimming.

3.4 Small amplitude expansion

Because the model is two dimensional we may introduce the stream function formulation and write $\mathbf{u} = \{\partial\psi/\partial y, -\partial\psi/\partial x\}$. In this manner the continuity equation is automatically satisfied and the Stokes equations reduce to a biharmonic equation in the stream function

$$\nabla^4\psi = 0. \tag{3.9}$$

We assume in this section that the amplitude of the traveling wave is much smaller than their wavelength, $\epsilon \ll 1$, and look to solve this problem by seeking a regular perturbation expansion in powers of ϵ, $\psi = \sum \epsilon^m \psi_m$. Because of the symmetry of the problem there is no difference in the boundary conditions if we change $\epsilon \to -\epsilon$ as this is equivalent to taking $x \to x + \pi$. This then naturally precludes the possibility of a synchronizing force appearing at all odd powers in ϵ.

3.4.1 Boundary conditions

We wish to prescribe a wave of transverse displacement to each sheet. However, doing so requires the material composing the sheets to be extensible as material points will accelerate relative one another. If we wish to forbid this relative motion, we may require the sheet to pass waves in an inextensible fashion. This may be visualized as material points moving along a conveyor of static shape, when observing the sheet in the wave frame [31, 32].

For extensible sheets the boundary conditions are given simply by the time

derivatives of the waveforms namely

$$u\,|_{y=y_1} = 0, \tag{3.10a}$$

$$v\,|_{y=y_1} = Dy_1/Dt, \tag{3.10b}$$

$$u\,|_{y=y_2} = 0, \tag{3.10c}$$

$$v\,|_{y=y_2} = Dy_2/Dt. \tag{3.10d}$$

For inextensible inextensible sheets the boundary conditions are given by

$$u\,|_{y=y_1} = 1-\alpha\cos\theta\,|_{y=y_1}, \tag{3.11a}$$

$$v\,|_{y=y_1} = -\alpha\sin\theta\,|_{y=y_1}, \tag{3.11b}$$

$$u\,|_{y=y_2} = 1-\alpha\cos\theta\,|_{y=y_2}+U_{\Delta}, \tag{3.11c}$$

$$v\,|_{y=y_2} = -\alpha\sin\theta\,|_{y=y_2}\,. \tag{3.11d}$$

where the angle, θ, is defined by $\tan\theta = \partial y/\partial x$ hence

$$\cos\theta = \frac{1}{\sqrt{1+(y')^2}}, \tag{3.12}$$

$$\sin\theta = y'\cos\theta, \tag{3.13}$$

and the material velocity (in the wave frame), α, is ratio of the length of the sheet to its wavelength multiplied by the wave speed, or

$$\alpha = \frac{1}{2\pi}\int_0^{2\pi}\sqrt{1+\left(\frac{\partial y}{\partial x}\right)^2}\,dx. \tag{3.14}$$

3.4.2 Expansion

Since we know that an expansion can yield a synchronizing force only at even powers in amplitude one would hope to see a relative force generated at order ϵ^2. We actually show below that for any waveform $g(x)$, the force is zero at order ϵ^2, and hence a perturbation expansion must carried out to order ϵ^4 in order to obtain the synchronizing dynamics.

The solution at each order m in the expansion ($\mathcal{O}(\epsilon^m)$) is given generally by

$$\psi_m = a_{m,0}(y) + \sum_{n=1}^{\infty}\Big[a_{m,n}(y)\cos(nz) + b_{m,n}(y)\sin(nz)\Big]. \tag{3.15}$$

The mean is given by

$$a_{m0}(y) = yu_{m0} + \mathrm{D}_{m,0}y^3 + \frac{y^2\left(U_{\Delta m} - 3\mathrm{D}_{m,0}\bar{h}^2 + u_{mh} - u_{m0}\right)}{2\bar{h}}, \tag{3.16}$$

where $D_{m,0}$ is an unknown constant and where we define

$$u_{m0} = \frac{1}{2\pi}\int_0^{2\pi} \frac{\partial \psi_m}{\partial y} \mid_{y=0} dx, \tag{3.17a}$$

$$u_{mh} + U_{\Delta m} = \frac{1}{2\pi}\int_0^{2\pi} \frac{\partial \psi_m}{\partial y} \mid_{y=\bar{h}} dx, \tag{3.17b}$$

as the mean components of the horizontal boundary conditions. The vertical boundary conditions cannot have a mean component and therefore do not contribute to the zeroth Fourier mode of the solution. The mean component is of particular interest as it is the only mode at any given order to contribute to the dynamics and in turn in order to solve for $D_{m,0}$ we must employ dynamical considerations.

To compute the force on the bottom sheet we note that we are free to move the integral along the surface of the sheet S, to any surface parallel to the x axis. This can be shown by integrating $\nabla \cdot \boldsymbol{\sigma} = 0$ over the area between the sheet and any such surface and using the periodicity of the problem. Alternatively, this can be shown by expanding as follows

$$\begin{aligned} F_x &= \mathbf{e}_x \cdot \int_S \boldsymbol{\sigma} \cdot \mathbf{n} dS \\ &= \int_0^{2\pi} \left[\sigma_{xy} - \epsilon g'(x)\sigma_{xx}\right]_{y=y_1} dx \\ &= \int_0^{2\pi} \left[\sigma_{xy} + \sum_{n=1}^{\infty} \epsilon^n \frac{\partial}{\partial x}\left(\frac{n-1}{n!} g^n \frac{\partial^{n-1}\sigma_{xx}}{\partial y^{n-1}}\right)\right]_{y=0} dx \\ &= \int_0^{2\pi} \sigma_{xy} \mid_{y=0} dx. \end{aligned} \tag{3.18}$$

We will use the result given by Eq. (3.18) repeatedly throughout this chapter. We also note that due to functional dependence of $g(z)$ spatial integration is invariant in time.

Using the above we find that the force on the bottom sheet of $\mathcal{O}(\epsilon^m)$ is

$$\begin{aligned} F_{mx} \mid_{y=y_1} &= \int_0^{2\pi} \left(\frac{\partial^2 \psi_m}{\partial y^2} - \frac{\partial^2 \psi_m}{\partial x^2} \right) \mid_{y=0} dx \\ &= 2\pi a''_{m,0}(0) \\ &= -6\pi \bar{h} D_{m0} + \frac{2\pi}{\bar{h}} (U_{\Delta m} + u_{mh} - u_{m0}), \end{aligned} \tag{3.19}$$

while the force on the upper sheet is similarly

$$\begin{aligned} F_{mx} \mid_{y=y_2} &= -2\pi a''_{m,0}(\bar{h}) \\ &= -6\pi \bar{h} D_{m0} - \frac{2\pi}{\bar{h}} (U_{\Delta m} + u_{mh} - u_{m0}). \end{aligned} \tag{3.20}$$

Hence we see that only the second derivative of the zeroth Fourier mode contributes to the force.

Finally, integrating mechanical equilibrium, $\nabla \cdot \boldsymbol{\sigma} = 0$, between the two sheets leads to the equality

$$\mathbf{F} \mid_{y=y_1} + \mathbf{F} \mid_{y=y_2} = 0 \tag{3.21}$$

where $\mathbf{F} = \int_S \boldsymbol{\sigma} \cdot \mathbf{n} dS$. Taking the x-component we find $F_{mx} \mid_{y=y_1} = -F_{mx} \mid_{y=y_2}$ at all orders and in order to satisfy this relationship we must have $D_{m,0} = 0$.

The force on the upper sheet is then

$$F_{mx} = \frac{2\pi}{\bar{h}} (u_{m0} - u_{mh} - U_{\Delta m}). \tag{3.22}$$

Setting $U_\Delta = 0$ gives rise to a phase-locking force in the static case, F_x^s (we use the superscript s to avoid confusion). We show in Appendix A.1 that leading order contribution to the force arises at fourth order in amplitude and hence the static force is given by

$$F_x^s = \epsilon^4 \frac{2\pi}{\bar{h}} (u_{40} - u_{4h}) + \mathcal{O}(\epsilon^6). \tag{3.23}$$

For free-swimming we thus see that the relative swimming sped is given by

$$U_\Delta = \frac{\bar{h}}{2\pi} F_x^s. \tag{3.24}$$

Noting that $d\phi/dt = -U_\Delta$ we therefore get an equation for the time-evolution of the phase as

$$\frac{d\phi}{dt} = -\frac{\bar{h}}{2\pi} F_x^s = \epsilon^4 (u_{4h} - u_{40}) + \mathcal{O}(\epsilon^6). \tag{3.25}$$

In Sec. 3.7 these analytical results for both the phase locking force and the dynamical problem are compared with a full numerical solution using the boundary integral formulation.

3.4.3 Energy dissipation

The energy dissipation rate between two sinusoidal sheets was originally computed by Taylor at leading order in the wave amplitude [13]. Here we restate his results for a general traveling wave. The energy dissipation per unit width in the fluid is equal to the rate of work of the sheets against the fluid

$$\dot{E} = -\int_S (\mathbf{u} \cdot \boldsymbol{\sigma} \cdot \mathbf{n}) \mid_{y=y_1} dS - \int_S (\mathbf{u} \cdot \boldsymbol{\sigma} \cdot \mathbf{n}) \mid_{y=y_2} dS. \tag{3.26}$$

Expanding the integral in ϵ we find to leading order

$$\begin{aligned} \dot{E} = \epsilon^2 \int_0^{2\pi} g'(x) \left(-p_1 + 2\frac{\partial v_1}{\partial y} \right) \mid_{y=0} dx \\ - \epsilon^2 \int_0^{2\pi} g'(x+\phi) \left(-p_1 + 2\frac{\partial v_1}{\partial y} \right) \mid_{y=\bar{h}} dx. \end{aligned} \tag{3.27}$$

Expressing the pressure in terms of the stream function and integrating by parts yields

$$\begin{aligned} \dot{E} = -\epsilon^2 \int_0^{2\pi} g(x) \frac{\partial^3 \psi_1}{\partial y^3} \mid_{y=0} dx \\ + \epsilon^2 \int_0^{2\pi} g(x+\phi) \frac{\partial^3 \psi_1}{\partial y^3} \mid_{y=\bar{h}} dx. \end{aligned} \tag{3.28}$$

We already know the form of these integrals (indeed they are equal) from the analysis of the force at $\mathcal{O}(\epsilon^2)$, and we find

$$\begin{aligned} \dot{E} = \pi \epsilon^2 \sum_{n=1}^{\infty} (\alpha_n^2 + \beta_n^2) \\ \times \Big[Q_n'''(0) - 2P_n'''(h) - \cos(n\phi) \left(Q_n'''(h) - 2P_n'''(0) \right) \Big], \end{aligned} \tag{3.29}$$

which we can evaluate to get

$$\dot{E} = 2\pi\epsilon^2 \sum_{n=1}^{\infty} n^3(\alpha_n^2 + \beta_n^2)\left[A(n\bar{h}) - \cos(n\phi)B(n\bar{h})\right], \tag{3.30}$$

where

$$A(\xi) = \frac{2\xi + \sinh 2\xi}{\sinh^2 \xi - \xi^2}, \tag{3.31a}$$

$$B(\xi) = \frac{2\xi\cosh\xi + 2\sinh\xi}{\sinh^2 \xi - \xi^2}. \tag{3.31b}$$

Setting $\beta_1 = 1$ and all other coefficients to zero in the above yields Taylor's result for pure sinewaves [13].

In the limit $\xi \to \infty$, we see that $A \to 2$, $B \to 0$, and the ratio B/A decays exponentially. This tells us what we intuitively expect: When $\bar{h}$ is large, the phase difference has little effect on the energy dissipation, and also the phase difference has a weaker effect on the energy dissipated by higher Fourier modes. Conversely, we expect that when the separation is small, the phase angle would have an large influence on the rate of working of the swimmers, and indeed when $\xi \to 0$, we zee $B/A \to 1$ as both $A, B \to 12\xi^{-3}$ (keeping in mind that we have implicitly assumed $\epsilon \ll \bar{h}$).

Importantly, because A and B are both positive and monotonically decaying functions with ξ, we know that in-phase swimming, $\phi = 0$, is a global minimum for the energy dissipated in the fluid. In addition, given that we have the symmetry $g(x + \pi) = -g(x)$, this restricts us to odd Fourier modes, and thus the out-of-phase configuration, $\phi = \pi$, is a global maximum. Taylor's dissipation argument [13] extends thus to arbitrary waveforms.

3.5 Lubrication limit

A second insightful limit to consider is the one in which the sheets are so close together that their mean separation is much smaller than the wavelength of the oscillations, $\bar{h} \ll \lambda$. In this lubrication limit the Stokes equations are substantially simplified, permitting analytical solutions. The main results of this section were previously summarized in a letter by the authors [25].

3.5.1 Lubrication equations

In order to facilitate this limit we must rescale the governing equations. We nondimensionalize vertical distances by $y^* = y/\bar{h}$, and horizontal distances $x^* = kx$, while assuming that $\delta = k\bar{h} \ll 1$. The instantaneous position of the sheets is therefore given by $y_1^* = a^* g(z^*)$ and $y_2^* = 1 + a^* g(z^* + \phi)$, where $a^* = a/h$ and again $x^* = z^* - t^*$ is the wave variable. Nondimensionalizing the continuity equation we find that if the horizontal velocity is given by $u = cu^*$ then the vertical velocity must be $v = \delta c v^*$. The Stokes equations then yield the lubrication equations to leading order in δ:

$$\frac{\partial u^*}{\partial x^*} = -\frac{\partial v^*}{\partial y^*}, \tag{3.32}$$

$$\frac{\partial p^*}{\partial y^*} = 0, \tag{3.33}$$

$$\frac{dp^*}{dx^*} = \frac{\partial^2 u^*}{\partial y^{*2}}, \tag{3.34}$$

where $p^* = \delta^2 p/\mu\omega$. Forces (per unit depth) are nondimensionalized as $F^* = F\delta/\mu c$, while energy dissipation rate per unit depth is $\dot{E}^* = \delta^2 \dot{E}/\mu\omega c\bar{h}$. We note that if g approaches a singular geometry we would leave the realm of validity of the lubrication approximation [33, 34]. We now drop the * notation for convenience.

We look to solve this problem in a frame moving with the wave speed of the bottom sheet. The boundary conditions in the lubrication limit are then given by

$$u(x, y = y_1) = -1, \tag{3.35a}$$

$$v(x, y = y_1) = -y_1'(z), \tag{3.35b}$$

$$u(x, y = y_2) = U_\Delta - 1, \tag{3.35c}$$

$$v(x, y = y_2) = -y_2'(z). \tag{3.35d}$$

Hence we see that in the lubrication limit the boundary conditions are identical to those of an extensible sheet. The full problem, regardless of whether extensible or inextensible boundary conditions are used, will collapse to the following lubrication results in the limit $\delta \ll 1$.

Given the above boundary conditions, the solution for the velocity field is found to be

$$u(z,y) = \frac{1}{2}\frac{dp}{dx}(y-y_1)(y-y_2) + U_\Delta \frac{y-y_1}{y_2-y_1} - 1. \tag{3.36}$$

If one integrates the continuity equation one finds

$$\int_{y_1}^{y_2} \frac{\partial u}{\partial x} dy = y_2' - y_1', \tag{3.37}$$

which then gives

$$\frac{dQ}{dx} = U_\Delta \frac{dy_2}{dx}. \tag{3.38}$$

With no relative motion, $U_\Delta = 0$, then the flow rate Q between the sheets is constant.

3.5.2 Hydrodynamic force

We first characterize the force generated when $U_\Delta = 0$ in order to determine the location and nature of the fixed points for the phase difference between the swimmers. With $U_\Delta = 0$, $Q = \text{const.}$, and we find

$$Q = \int_{y_1}^{y_2} u dy = -\frac{1}{12}\frac{dp}{dx}h^3 - h, \tag{3.39}$$

where $h = y_2 - y_1$. We now exploit the periodicity of the system to obtain the value of Q by noting that

$$\int_0^{2\pi} \frac{dp}{dx} dx = -12 \int_0^{2\pi} \frac{1}{h^2} dx - 12Q \int_0^{2\pi} \frac{1}{h^3} dx = 0. \tag{3.40}$$

We thus have

$$Q = -\frac{I_2}{I_3}, \tag{3.41}$$

where

$$I_j = \int_0^{2\pi} h^{-j} dx. \tag{3.42}$$

The pressure gradient is therefore given by

$$\frac{dp}{dx} = 12\left(\frac{I_2}{h^3 I_3} - \frac{1}{h^2}\right). \tag{3.43}$$

The force per unit depth on the upper sheet is given by

$$F_x = \mathbf{e}_x \cdot \int_S \boldsymbol{\sigma} \cdot \mathbf{n} dS, \tag{3.44}$$

where the curve S is defined by $y = y_2$. Evaluating Eq. (3.44) gives

$$F_x = \int_0^{2\pi} \left[\frac{dy_2}{dx}\left(-p + 2\delta^2 \frac{\partial u}{\partial x}\right) - \left(\frac{\partial u}{\partial y} + \delta^2 \frac{\partial v}{\partial x}\right)\right]_{y=y_2} dx. \tag{3.45}$$

We keep only the $\mathcal{O}(1)$ terms in the lubrication limit $\delta \ll 1$ which yields

$$F_x = -\int_0^{2\pi} \left[\frac{dy_2}{dx} p + \frac{\partial u}{\partial y}\right]_{y=y_2} dx. \tag{3.46}$$

Exploiting the periodicity of the problem through integration by parts [35] allows us to recast the force as

$$F_x = \int_0^{2\pi} \left(y_2 \frac{dp}{dx} - \frac{\partial u}{\partial y}\right) |_{y=y_2}\, dx. \tag{3.47}$$

Substituting in Eq. (3.36) and Eq. (3.43), and noting any constant multiplying the pressure gradient may be discarded, we find the force to be given by

$$F_x = 6a \int_0^{2\pi} \left(\frac{I_2}{h^3 I_3} - \frac{1}{h^2}\right) \big[g(x+\phi) + g(x)\big] dx. \tag{3.48}$$

3.5.3 Fixed points

By symmetry, we found earlier that there are always fixed points at $\phi = 0, \pi$. This is easily confirmed by evaluating Eq. (3.48). For $\phi = 0$, h is constant, and thus $I_2/h^3 I_3 - 1/h^2 = 0$, leading to $F_x = 0$; for $\phi = \pi$, we have $g(x+\pi) + g(x) = 0$ by symmetry, and again $F_x = 0$.

In order to determine their stability, we can expand the force, Eq. (3.48), about these fixed points. Letting $\phi = \phi_0 + \phi'$ where $\phi' \ll 1$ we obtain near the in-phase fixed point, $\phi_0 = 0$,

$$F_{x_0} = -72a^4 \phi'^3 \int_0^{2\pi} g(x) g'(x)^3 dx + \mathcal{O}(\phi'^4). \tag{3.49}$$

In contrast, near the opposite-phase fixed point, $\phi_0 = \pi$, we get

$$F_{x_\pi} = 6a^3\phi'^3 \int_0^{2\pi} \frac{g'(x)^3}{(1-2ag(x))^4} \left(\frac{1}{(1-2ag(x))} \frac{J_2}{J_3} \right) dx + \mathcal{O}(\phi'^4), \tag{3.50}$$

where we have defined

$$J_n = \int_0^{2\pi} (1-2ag(x))^{-n} dx. \tag{3.51}$$

If we then assume $a \ll 1$ then Eq. (3.50) reduces to

$$F_{x_\pi} \approx 72a^4\phi'^3 \int_0^{2\pi} g(x)g'(x)^3 dx + \mathcal{O}(\phi'^4). \tag{3.52}$$

We see then that for small amplitude waves, and small deviations in phase about the fixed points, the force about the in-phase configuration ($\phi_0 = 0$) is equal and opposite to the force about the out-of-phase configuration ($\phi = \pi$). Unless both of them are neutrally stable (which is the case if the waveforms are too symmetric, see Sec. 3.3) we therefore obtain the important result that, for a given waveform, one fixed point will always be stable, while the other one will always be unstable. To determine which one is the stable point, one has to evaluate the geometric integral, $A = \int_0^{2\pi} gg'^3 dx$. If $A < 0$ then the fixed point at $\phi = 0$ is stable, while it is the one at $\phi = \pi$ in the case $A > 0$. Stable passive hydrodynamic synchronization thus always takes place for swimmers with asymmetric waveforms.

As a side note, we can also expand the force (3.48) in powers of $a \ll 1$, and we see that the leading order contribution is fourth order in amplitude, given for general ϕ as

$$F_x \approx -36a^4 \int_0^{2\pi} \Big(g(x+\phi) + g(x) \Big) \Big(g(x+\phi) - g(x) \Big)^3 dx, \tag{3.53}$$

plus terms at $\mathcal{O}(a^6)$. We see that in the small amplitude limit there are only two fixed points for nontrivial waveforms g. The fourth-order scaling of the hydrodynamic force, Eqs. (3.49), (3.52) and (3.53), is reminiscent of the small-amplitude calculations from Sec. 3.4 showing that no force can occur at second order in the wave amplitude, but a nonzero force does come at fourth order.

3.5.4 Energy dissipation

The energy dissipated by viscous stress in the volume V of fluid between the sheets by is given by

$$\dot{E} = \int_V \boldsymbol{\sigma} : \nabla \mathbf{u} \, dV. \tag{3.54}$$

In the lubrication limit, assuming unit width, the energy dissipation over one wavelength is then

$$\dot{E} = \int_0^{2\pi} \int_{y_1}^{y_2} \left(\frac{\partial u}{\partial y} \right)^2 dy dx, \tag{3.55}$$

and given Eq. (5.6) we have

$$\dot{E} = \frac{1}{12} \int_0^{2\pi} h^3 \left(\frac{dp}{dx} \right)^2 dx, \tag{3.56}$$

which is explicitly

$$\dot{E} = 12 \int_0^{2\pi} \frac{1}{h} \left(\frac{I_2}{I_3 h} - 1 \right)^2 dx. \tag{3.57}$$

We see the energy dissipation is non-negative and identically zero when $\phi = 0$ (i.e. when h is constant) and hence this must be a global minimum.

If we let $\phi = \phi_0 + \phi'$ where $\phi' \ll 1$, we find near the in-phase conformation, $\phi_0 = 0$

$$\dot{E}_0 = 12 a^2 \phi'^2 \int_0^{2\pi} g'(x)^2 dx + \mathcal{O}(\phi'^4), \tag{3.58}$$

and the energy increases quadratically with the slope of the wave from zero when $\phi = 0$. Near the opposite-phase conformation, $\phi_0 = \pi$, we get

$$\begin{aligned} \dot{E}_\pi = 12 \left(J_1 - \frac{J_2^2}{J_3} \right) - 12 \phi'^2 \int_0^{2\pi} \Bigg\{ & \frac{g'(x)^2}{(1 - 2ag(x))^3} \\ & \times \left[1 + \frac{6}{(1 - 2ag(x))} \frac{J_2}{J_3} \left(\frac{1}{(1 - 2ag(x))} \frac{J_2}{J_3} - 1 \right) \right] dx \Bigg\} \\ & + \mathcal{O}(\phi'^4). \end{aligned} \tag{3.59}$$

If we further assume that $a \ll 1$ we see that

$$\dot{E}_\pi \approx 12a^2 \int_0^{2\pi} \left[4g(x)^2 - g'(x)^2\phi'^2\right] dx. \tag{3.60}$$

Hence for any waveform $g(x)$ the energy dissipated between the sheets is maximum in the opposite-phase conformation, $\phi = \pi$.

Finally, if we expand the energy dissipation, Eq. (3.57), in small amplitude for general ϕ, we find

$$\dot{E} = 12a^2 \int_0^{2\pi} \left[g(x+\phi) - g(x)\right]^2 dx + \mathcal{O}(a^3). \tag{3.61}$$

We can see clearly again that the energy dissipation is a global minimum when $\phi = 0$ and maximum when $\phi = \pi$ due to the $g(x+\pi) \to -g(x)$ symmetry of the waveform; this is in agreement with the previous small amplitude results for arbitrary separation.

An important consequence of the previous results is that, although the nature of the fixed points depends on the swimmer waveform, the location of the minimum of energy dissipation does not. The conformation of minimum energy dissipation is not necessarily stable: depending on the waveform geometry, the opposite-phase conformation, $\phi = \pi$, may be stable (specifically, when $A > 0$) yet it is the one corresponding to a maximum of energy dissipation.

Experimental evidence shows that spermatozoa cells synchronize at the in-phase conformation (and indeed $A < 0$ for the linearly increasing sine waves indicated by Rikmenspoel [30]). However, we find at least one instance, in the figures in Ref. [11], which show spermatozoa flagella seemingly synchronized in opposite-phase (although no mention of phase difference is reported in the text).

3.5.5 Dynamics

After calculating the hydrodynamic force, we now look to solve for the time-evolution of the phase. We thus assume that the sheets are force free, $F_x = 0$, and find the corresponding value of U_Δ. From Eq. (5.7) we know

$$\frac{\partial}{\partial x} \int_{y_1}^{y_2} u dy = U_\Delta \frac{dy_2}{dx}. \tag{3.62}$$

Integrating in x and evaluating the integral in y gives an expression for the pressure gradient as

$$\frac{dp}{dx} = \frac{6U_\Delta - 12}{h^2} - \frac{12U_\Delta y_2 + C}{h^3}, \tag{3.63}$$

where C is a constant of integration. We find this constant by exploiting the periodicity of the pressure field, leading to

$$C = \Big(6U_\Delta(I_2 - 2K) - 12I_2\Big)/I_3, \tag{3.64}$$

where $K = \int_0^{2\pi} y_2 h^{-3} dx$.

The force on the upper sheet is given by

$$F_x = \int_0^{2\pi} \left(\frac{1}{2}\frac{dp}{dx}(y_2 + y_1) - \frac{U_\Delta}{h}\right) dx. \tag{3.65}$$

We then solve for U_Δ by enforcing that the sheets are force free. It is worth noting that when we set $U_\Delta = 0$, we retrieve the force from the static case given by Eq. (3.48), which we label here F_x^s to avoid confusion. Now since $U_\Delta = -d\phi/dt$ we find that the phase evolves in time according to

$$\frac{d\phi}{dt} = -\mathcal{M}F_x^s, \tag{3.66}$$

where the mobility, $\mathcal{M}$, is given by

$$\mathcal{M}^{-1} = \int_0^{2\pi} \Bigg\{\frac{1}{h} - \left[\frac{1}{h^2} - \frac{1}{h^3}\left(2y_2 + \frac{I_2 - 2K}{I_3}\right)\right] \times 3(y_2 + y_1)\Bigg\} \mathrm{d}x. \tag{3.67}$$

As physically expected, the rate at which the phase changes, Eq. (3.66), is proportional to the static force, F_x^s, which would be applied if the sheets where not permitted to move. The result is a first-order integro-differential equation for ϕ.

Expanding Eq. (3.66) for small amplitude, $a \ll 1$, we find

$$\frac{d\phi}{dt} \approx \frac{36a^4}{2\pi} \int_0^{2\pi} \Big(g(x+\phi) + g(x)\Big)\Big(g(x+\phi) - g(x)\Big)^3 dx, \tag{3.68}$$

plus terms at order a^6. We thus see that $d\phi/dt \sim -F_x^s/2\pi$ for small amplitude, and hence the mobility becomes $1/2\pi$ in this limit. Notably, the result given by

Eq. (3.68) is the same as the one given by Eq. (3.25) after proper dimensional rescaling.

We now expand near the fixed points by letting $\phi = \phi_0 + \phi'$ and obtain

$$\frac{d\phi'}{dt} \sim \pm \frac{36}{\pi} a^4 A \phi'^3, \tag{3.69}$$

with a positive sign for $\phi_0 = 0$, and negative $\phi_0 = \pi$. Solving this differential equation gives the exact phase dynamics for small times as

$$\phi' = \frac{\mathrm{sgn}(\phi_i')}{\sqrt{\phi_i'^{-2} \mp 72 a^4 A t/\pi}}, \tag{3.70}$$

where $\phi'(t=0) = \phi_i'$. In the case of a stable fixed point, we thus get that the typical time for synchronization scales as $t \sim 1/a^4|A|$, and thus the phase-locked state is reached faster for waves of larger amplitude (a increases), and larger asymmetry ($|A|$ increases). Note that, as a difference, the typical time for synchronization in a viscoelastic fluids scales as the inverse square of the wave amplitude [29].

3.6 Boundary integral formulation

The boundary integral method may be used to address numerically the synchronization between the swimmers for shapes of arbitrary amplitude, as well as confirm our asymptotic results. We present in this section the principle of the method and our implementation of it, which is quite similar to that given by Pozrikidis in his study of peristaltic pumping [36], and hence will be brief. The equations in the section are nondimensionalized similarly to the procedure of Sec. 3.2.

Consider any two solutions to the Stokes equations, $\{\mathbf{u}, \boldsymbol{\sigma}\}$ and $\{\tilde{\mathbf{u}}, \tilde{\boldsymbol{\sigma}}\}$ with no associated body forces for any closed surface S of outward normal $\mathbf{n}$. The Lorentz reciprocal theorem [37] gives the equality

$$\int_S (\mathbf{u} \cdot \tilde{\boldsymbol{\sigma}} - \tilde{\mathbf{u}} \cdot \boldsymbol{\sigma}) \cdot \mathbf{n} \, dS = 0. \tag{3.71}$$

If we take for $\tilde{\mathbf{u}}$ and $\tilde{\boldsymbol{\sigma}}$ in Eq. (3.71) the fundamental solutions for two-dimensional

Stokes flow

$$\tilde{\mathbf{u}}(\mathbf{x}) = \frac{1}{4\pi}\mathbf{G}(\hat{\mathbf{x}}) \cdot \tilde{\mathbf{f}}(\mathbf{x}_0), \tag{3.72}$$

$$\tilde{\boldsymbol{\sigma}}(\mathbf{x}) = \frac{1}{4\pi}\mathbf{T}(\hat{\mathbf{x}}) \cdot \tilde{\mathbf{f}}(\mathbf{x}_0), \tag{3.73}$$

for the velocity and the stress at the field point $\mathbf{x}$, due to the point force $\tilde{\mathbf{f}}$ at $\mathbf{x}_0$, where $\hat{\mathbf{x}} = \mathbf{x} - \mathbf{x}_0$ and the two-dimensional Stokeslet $\mathbf{G}$ and stresslet $\mathbf{T}$ are given by

$$\mathbf{G} = -\mathbf{I}\ln(|\hat{\mathbf{x}}|) + \frac{\hat{\mathbf{x}}\hat{\mathbf{x}}}{|\hat{\mathbf{x}}|^2}, \tag{3.74}$$

$$\mathbf{T} = -4\frac{\hat{\mathbf{x}}\hat{\mathbf{x}}\hat{\mathbf{x}}}{|\hat{\mathbf{x}}|^4}, \tag{3.75}$$

then one obtains the boundary integral formulation of the two-dimensional Stokes equations for the velocity field within the fluid domain, V, and on the boundary, S, respectively,

$$\mathbf{u}(\mathbf{x}_0)|_{\mathbf{x}_0 \in V} = \frac{1}{4\pi}\int_S \left(\mathbf{u}(\mathbf{x}) \cdot \mathbf{T}(\hat{\mathbf{x}}) \cdot \mathbf{n} - \mathbf{f}(\mathbf{x}) \cdot \mathbf{G}(\hat{\mathbf{x}})\right)\, dS(\mathbf{x}), \tag{3.76}$$

$$\mathbf{u}(\mathbf{x}_0)|_{\mathbf{x}_0 \in S} = \frac{1}{2\pi}\int_S \left(\mathbf{u}(\mathbf{x}) \cdot \mathbf{T}(\hat{\mathbf{x}}) \cdot \mathbf{n} - \mathbf{f}(\mathbf{x}) \cdot \mathbf{G}(\hat{\mathbf{x}})\right)\, dS(\mathbf{x}), \tag{3.77}$$

where we have used $\mathbf{f} = \boldsymbol{\sigma} \cdot \mathbf{n}$.

Since the problem we consider is 2π-periodic, we can reduce the domain of integration S to a single period by using an infinite sum of periodically placed Stokeslets and stresslets,

$$\mathbf{G}^p = \sum_{n=-\infty}^{\infty} -\mathbf{I}\ln(|\hat{\mathbf{x}}_n|) + \frac{\hat{\mathbf{x}}_n\hat{\mathbf{x}}_n}{|\hat{\mathbf{x}}_n|^2}, \tag{3.78}$$

$$\mathbf{T}^p = \sum_{n=-\infty}^{\infty} -4\frac{\hat{\mathbf{x}}_n\hat{\mathbf{x}}_n\hat{\mathbf{x}}_n}{|\hat{\mathbf{x}}_n|^4}, \tag{3.79}$$

where $\hat{\mathbf{x}}_n = \{\hat{x}_0 + 2\pi n, \hat{y}_0\}$ [38]. As shown in [39] these may be expressed in closed form by using the summation formula

$$B = \sum_{n=-\infty}^{\infty} \ln(|\hat{\mathbf{x}}_n|) = \frac{1}{2}\ln\left[2\cosh(\hat{y}_0) - 2\cos(\hat{x}_0)\right]. \tag{3.80}$$

We can then construct the elements of $\mathbf{G}^p$ and $\mathbf{T}^p$ using B and its derivatives as follows:

$$\begin{aligned}
G^p_{xx} &= -B - \partial_y B + 1, \\
G^p_{xy} &= y\partial_x B, \\
G^p_{yy} &= -B + y\partial_y B, \\
T^p_{xxx} &= -2(2\partial_x B + y\partial_{xy} B), \\
T^p_{xxy} &= -2(\partial_y B + y\partial_{yy} B), \\
T^p_{xyy} &= 2y\partial_{xy} B, \\
T^p_{yyy} &= -2(\partial_y B - y\partial_{yy} B),
\end{aligned} \tag{3.81}$$

where the Stokeslet and stresslet are invariant under permutation of its indices [38].

Following the approach outlined by Higdon [40], the boundary S (the surface of each sheet as the sides cancel) is discretized into $2N$ straight line elements S_n. We assume the stress $\mathbf{f}$ and the velocity $\mathbf{u}$ are linear functions over a particular interval ($\mathbf{f} \to \mathbf{f}_n$, $\mathbf{u} \to \mathbf{u}_n$) and then collocate $\mathbf{x}_0$ at each of the $2N$ segments, $\mathbf{x}_0 \to \mathbf{x}_m$, to obtain a system of N equations with N unknowns. The periodic Stokeslet and stresslet are regularized by subtracting off from them their non-periodic counterparts and then adding back the difference; the two-dimensional Stokeslet and stresslet are then integrated analytically. We hence have

$$\begin{aligned}
\mathbf{u}(\mathbf{x}_m) = \frac{1}{2\pi} \sum_{n=1}^{2N} \Bigg[& \int_{S_n} \mathbf{u}_n \cdot (\mathbf{T}^p - \mathbf{T}) \cdot \mathbf{n}_n dS_n \\
& - \int_{S_n} \mathbf{f}_n \cdot (\mathbf{G}^p - \mathbf{G})\, dS_n \\
& + \int_{S_n} \mathbf{u}_n \cdot \mathbf{T} \cdot \mathbf{n}_n dS_n - \int_{S_n} \mathbf{f}_n \cdot \mathbf{G} dS_n \Bigg].
\end{aligned} \tag{3.82}$$

The regularized integrals have a removable singularity at $\mathbf{x} = \mathbf{x}_m$ which is obtained by Taylor expansion. The boundary integral formulation is thereby reduced to a linear system that can be inverted using standard techniques to obtain the stress

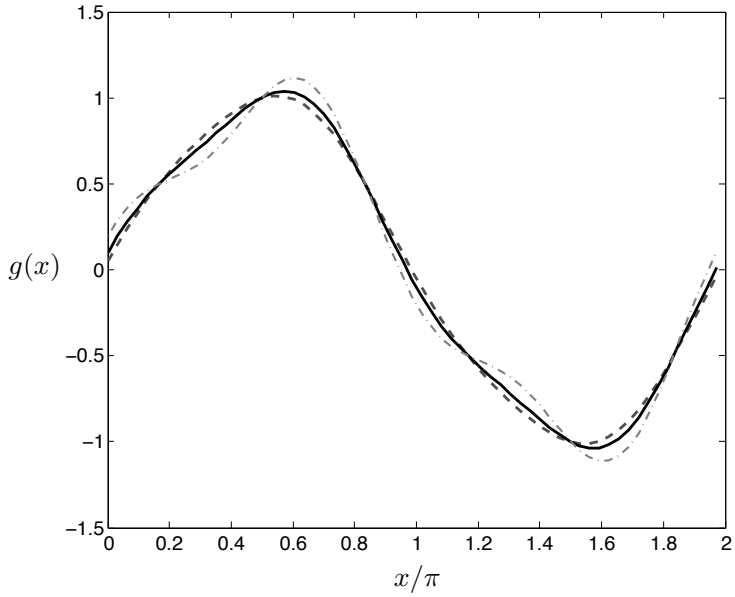

Figure 3.3: Illustration of the waveform $g(x) = \sin x + \gamma \cos 3x$ for varying asymmetry. The dashed line corresponds to $\gamma = 0.05$, solid line $\gamma = 0.1$, and dash-dot line $\gamma = 0.2$.

b. The force on the top sheet is then given by integrating the stress

$$F_x = \sum_{n=N+1}^{2N} \left[\mathbf{e}_x \cdot \int_{S_n} \mathbf{f}_n dS_n \right]. \tag{3.83}$$

In order to solve for the dynamical problem we let the boundary condition be represented by a sum of a surface deformations and an unknown rigid body motion, $\mathbf{u} \to \mathbf{u}_n + U_\Delta \mathbf{e}_x$, on the upper sheet. The additional unknown, U_Δ, is found by enforcing that the sheets are force free, $F_x = 0$.

The numerical procedure was validated through convergence tests and by reproducing previous results for shear flow over sinusoidal surfaces [39]. A large number of elements ($2N$) is needed when the sheets are close together or if they are far apart and the amplitude is small but in both these regimes in which we have asymptotic formulae from the previous sections as further verification.

3.7 Results

We now present in this section the results of both our asymptotic and numerical calculations to address the synchronization of specific waveforms. For illustrative purposes we restrict ourselves here to the family of waveforms described by the function,

$$g(x) = \sin x + \gamma \cos 3x, \tag{3.84}$$

i.e. $\beta_1 = 1$, $\alpha_3 = \gamma$, and all other modes equal to zero, as illustrated in Fig. 5.2. In essence these shapes are geometric perturbations (small for small γ) to Taylor's sinusoidal swimming sheet. They have a broken front-back symmetry when γ is nonzero. Reversing the sign of γ is equivalent to reflecting the geometry of each wave about the vertical axis, $\{\gamma \to -\gamma\} = \{x \to -x + \pi\}$, which itself is equivalent to reversing the kinematics of the problem. In other words, changing the sign of γ changes the sign of the forces on the sheets which leads to stable fixed points becoming unstable, and vice versa. In addition, the simple form of $g(x)$ allows us to obtain some explicit formulae from the general theory presented in Secs. 3.4 and 3.5.

In the lubrication limit, the geometric parameter $A = \int_0^{2\pi} g g'^3 dx = -2\pi\gamma$ controls the evolution of the phase near fixed points. We see that $\gamma > 0$ gives $A < 0$, which leads a stable fixed point at $\phi = 0$ and unstable at $\phi = \pi$. By symmetry, $\gamma < 0$ necessarily gives $A > 0$, and thereby exchanges the location of the stable and unstable fixed points. In addition, from Eq. (3.53), we have that when $a \ll 1$ the phase locking force is given by

$$F_x = 144\pi a^4 \gamma \sin^3 \phi, \tag{3.85}$$

which is linear in the asymmetry and quartic in the amplitude, and leads to a time-evolution of the phase as

$$\frac{d\phi}{dt} = -72 a^4 \gamma \sin^3 \phi. \tag{3.86}$$

The energy dissipation in the lubrication limit, for $a \ll 1$, Eq. (3.61), is

$$\dot{E} \approx 24\pi a^2 \left[1 - \cos\phi + \gamma^2 (1 - \cos 3\phi)\right]. \tag{3.87}$$

Similarly, in the small amplitude limit, Eq. (3.30) yields

$$\dot{E} \approx 2\pi\epsilon^2 \Big[A(\bar{h}) - B(\bar{h}) \cos\phi + 3^3\gamma^2 \big(A(3\bar{h}) - B(3\bar{h}) \cos 3\phi \big) \Big], \tag{3.88}$$

where the functions A and B, given by Eq. (3.31), introduce a dependance on the separation h, and Eq. (3.88) reduces to Eq. (3.87) when $\bar{h}$ is small (after accounting for the separate scalings).

We see clearly that the energy dissipation rate is invariant under $\gamma \to -\gamma$ and further, when we are assuming that γ is a small, the change in the energy dissipation due to the asymmetry is also small, $\mathcal{O}(\gamma^2)$.

3.7.1 Comparison between asymptotic and numerical methods

In the small amplitude limit (3.4) we have explicitly assumed that $\epsilon \ll 1$, and also implicitly that $\epsilon \ll \bar{h}$. The lubrication limit (3.5) effectively captures the physics of the problem when the sheets are quite close together, i.e. the limit $\bar{h} \ll 2\pi$. If we want in addition the phase, ϕ, to be able to span the range of all possible values then we also get the geometrical constraint $\epsilon < \bar{h}/2$ (or, in terms of lubrication variables, $a < 1/2$). There exists therefore a regime in which both asymptotic approaches are valid, namely the limit $\epsilon \ll h \ll 1$.

As a validation of our methods we plot the analytical results from both asymptotic limits, together with the numerical results, for such a regime in Fig. 3.4 (top). The static force on the top sheet, F_x^s, is shown for the waveform of Eq. (3.84) with an asymmetry of $\gamma = 0.1$ and wave amplitude $\epsilon = 0.01$ (in this plot the forces have been scaled for display purposes only, see caption). The solid lines represent the small amplitude limit, dashed lines the lubrication limit, and symbols are for the numerical data obtained from the boundary integral method. The results from all three methods agree quantitatively for small swimmer-swimmer separation, $\bar{h}$. As the value of $\bar{h}$ increases, the lubrication results start to deviate, but the small amplitude results remains accurate (recall that $\epsilon \ll 1$ in all cases).

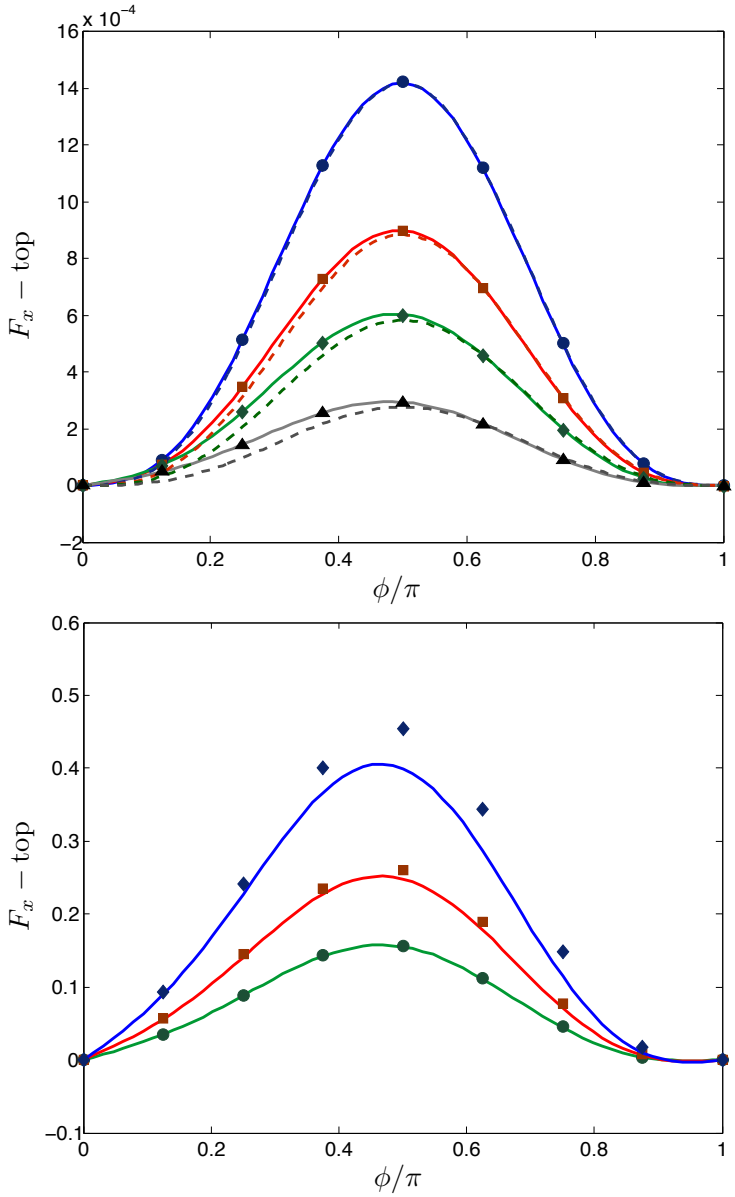

Figure 3.4: Force, F_x, vs. phase difference, ϕ, for an asymmetry of $\gamma = 0.1$, in the lubrication limit (dashed lines, top figure only), small amplitude limit (solid lines, both figures), and using the boundary integral method (symbols, both figures). Top: fixed amplitude, $\epsilon = 0.01$, and varying swimmer-swimmer distances, $\bar{h}$; circles: F_x, $\bar{h} = 0.2$; squares: $10F_x$, $\bar{h} = 0.4$; diamonds: F_x/ϵ, $\bar{h} = 0.6$; triangles: $2F_x/\epsilon$, $\bar{h} = 0.8$. Bottom: Fixed separation distance $\bar{h} = 1$ and varying waveform amplitudes; circles: $\pi F_x/\epsilon$, $\epsilon = 0.1$; squares: πF_x with $\epsilon = 0.2$; diamonds: F_x, $\epsilon = 0.4$. We observe a gradual breakdown of the lubrication approximation for increased separation, $\bar{h}$ (top), and of the small amplitude expansion for increased amplitude ϵ (bottom). Note that forces have been scaled for display purposes.

For larger values of the separation distance between the swimmers, the lubrication results cannot be applied, but the small-amplitude asymptotics, Eq. (3.23), remain valid as long as the wave amplitude is small. The value of the static force is compared to the numerical results in Fig. 3.4 (bottom) for large separation, $\bar{h} = 1$, and as function of the wave amplitude, ϵ. The agreement between the two is excellent for $\epsilon = 0.1$, but they deviate quantitatively for larger wave amplitudes (although the correct order of magnitude, and dependence on ϕ, is obtained).

3.7.2 Stability

When we introduce a variable separation between the swimmers, $\bar{h}$, and thus go beyond the small $\bar{h}$ limit from the lubrication approximation, we find that the number of fixed points and their nature does not depend solely on the waveform geometry, but actually also on the swimmer-swimmer distance. In Fig. 3.5 (top) we show the dependence of the static force on the phase, for an amplitude $\epsilon = 0.1$ and an asymmetry $\gamma = 0.1$, as we vary the separation between the swimmers $\bar{h}$ (line: small-amplitude asymptotics; symbols: boundary integral computations). A fixed point is a conformation with phase difference ϕ such that $F_x(\phi) = 0$; if the slope of the force is positive the fixed point is stable, while a negative slope indicates an unstable fixed point. What we see in Fig. 3.5 (top) is that increasing the separation between the sheets from the small $\bar{h}$ values in the lubrication limit gives rise to an additional fixed point. In the case illustrated in Fig. 3.5 (top), this new fixed point is always unstable. It first appears near $\phi = \pi$ (leading to the fixed point at $\phi = \pi$ becoming stable), moves toward $\phi = 0$ when the separation distance between the swimmers increases, and eventually merges with $\phi = 0$, which then turns to an unstable point, at a critical value of $\bar{h}$.

In Fig. 8.6 we display the location of the fixed points explicitly as a function of $\bar{h}$ in the small amplitude limit for $\gamma > 0$. In this limit, the force is linear in the asymmetry, γ, therefore the location of the fixed points is invariant under a linear scaling of the asymmetry, $\gamma \to b\gamma$ where $b > 0$, while the nature of the fixed points changes with a change of the sign of γ. The appearance of a new fixed point, described in the previous paragraph, is apparent. As $\bar{h}$ tends asymptotically to

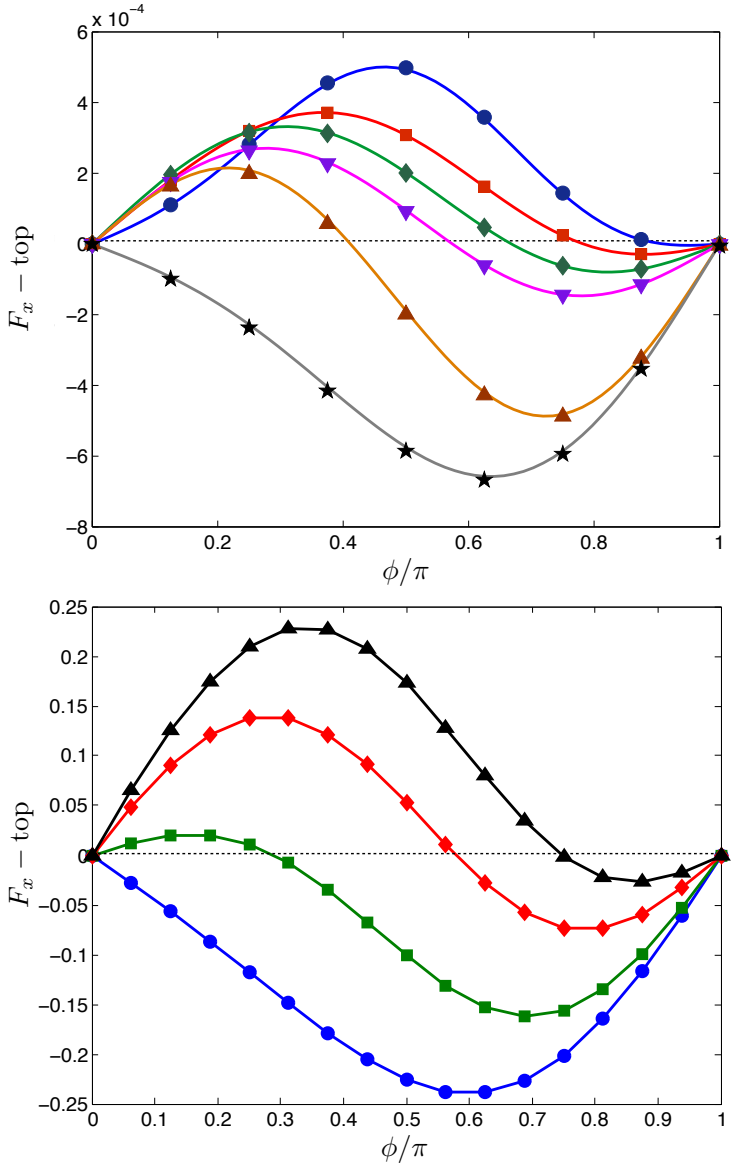

Figure 3.5: Dependence of the force, F_x, on the phase ϕ for varying separation $\bar{h}$ with an asymmetry $\gamma = 0.1$. Top: small dimensionless amplitude, $\epsilon = 0.1$. The solid lines are obtained in the small amplitude limit while symbols are for boundary integral computations; circles: ϵF_x, $\bar{h} = 1$; squares: $2F_x$, $\bar{h} = 2$; diamonds: $\pi F_x/2\epsilon$, $\bar{h} = 3$; down triangles: F_x/ϵ^2, $\bar{h} = 4$; up triangles: F_x/ϵ^3, $\bar{h} = 5$; stars: $F_x/\pi\epsilon^4$, $\bar{h} = 6$. Increasing the distance between the sheets introduces an additional fixed point not present in the lubrication limit, and its position moves with $\bar{h}$. Bottom: numerical results using the boundary integral method (solid line and symbols) in the case of high amplitude waves, $\epsilon = 1$. triangles : F_x, $\bar{h} = 3$; diamonds: $2\pi F_x$, $\bar{h} = 4$; squares: $10\pi F_x$, $\bar{h} = 5$; circles: $100F_x$, $\bar{h} = 6$. Forces have been scaled for display purposes.

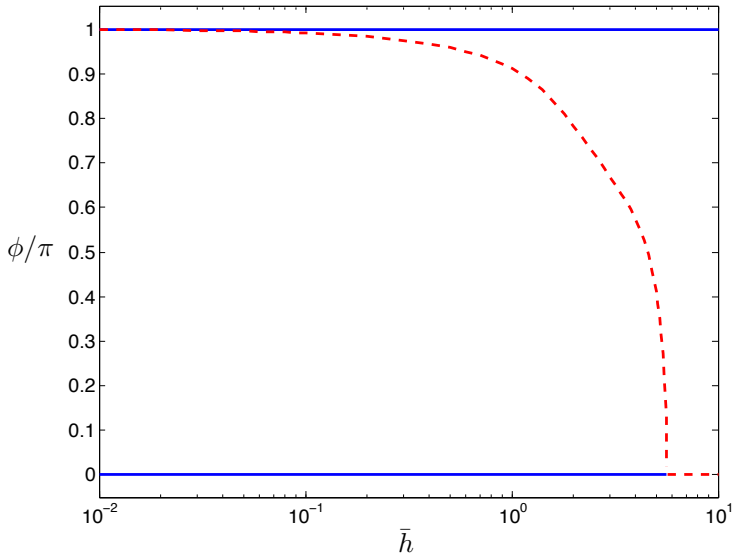

Figure 3.6: Location of the fixed points (value of the phase ϕ such that $F_x(\phi) = 0$) as a function of $\bar{h}$ as obtained in the small amplitude limit for $\gamma > 0$. The solid lines indicate a stable fixed point whereas the dashed line indicates an unstable fixed point. The position of the unstable fixed point moves with $\bar{h}$: it is created for small values of $\bar{h}$ near $\phi = \pi$, migrates to the left, and merges with $\phi = 0$ at the critical value $\bar{h} \approx 5.65$. In the opposite case where $\gamma < 0$, the stable fixed points become unstable and vice versa.

zero, $\phi = 0$ is stable (blue solid line) while $\phi = \pi$ is unstable (red dashed line), which is the lubrication result. For intermediate values of $\bar{h}$, both 0 and π are stable, and the new fixed point moves from π to 0 as $\bar{h}$ increases. It merges with $\phi = 0$ for a critical distance between the swimmers ($\bar{h} \approx 5.65$ for our choice of waveform), at which point $\phi = 0$ becomes unstable, and remains so for larger values of $\bar{h}$. As expected, upon a reversing the sign of γ, stable fixed points become unstable and vice versa.

Further analysis of the equations of motion shows that the additional fixed point that arises when $\bar{h}$ is past the lubrication limit is a direct consequence of the inextensible boundary conditions. In the lubrication limit, the boundary conditions are extensible insofar as the there is only a vertical component. However away from this limit there arises horizontal motion to maintain inextensibility, and it is precisely this horizontal motion which leads to the additional dynamic complexity. Conversely for extensible boundary conditions, Eq. (3.10), the fixed points remain unchanged from those in the lubrication limit.

Using the boundary integral formulation it is possible to extend these results to large amplitude waves. In Fig. 3.5 (bottom) we show the horizontal force on the upper sheet as a function of the phase between the swimmers for various mean swimmer-swimmer separation but now with $\epsilon = 1$. The results are qualitatively similar to those obtained in the small amplitude limit, with the occurrence of a new fixed point, unstable, and moving from $\phi = \pi$ to $\phi = 0$ as the separation increases. A difference we do observe between small and large amplitude is that the location of the fixed point is no longer invariant under a change in the asymmetry factor, γ. In Fig. 3.7 (top) we show that an increase in the asymmetry factor leads to a small, but nonzero, migration of the mobile fixed point toward π. A similar drift is obtained with an increase in the waveform amplitude (Fig. 3.7, bottom).

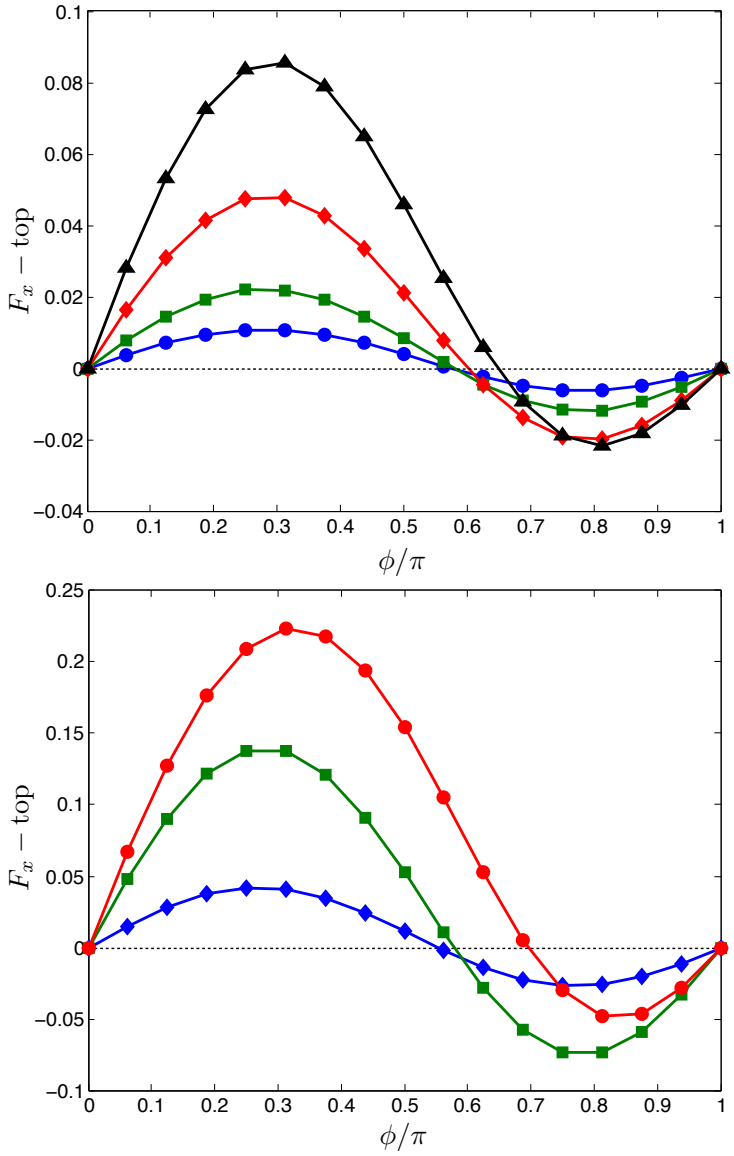

Figure 3.7: Plot of the force on the top swimmer, F_x, as a function of the phase difference, ϕ, using the boundary integral method with $\bar{h} = 4$. Top: $\epsilon = 1$ for varying asymmetry; blue circles: $\gamma = 0.05$; green squares: $\gamma = 0.1$; red diamonds: $\gamma = 0.2$; black triangles $\gamma = 0.3$. We see that for large amplitude waves the force is no longer linear with asymmetry as evidenced by the moving of the middle fixed point. Bottom: $\gamma = 0.1$ for varying large amplitude waves; blue diamonds: $10\pi F_x$, $\epsilon = 0.5$; green squares: $2\pi F_x$, $\epsilon = 1$; red circles: F_x, $\epsilon = 1.5$. We see that for $\epsilon \leq 1$ the location of the middle fixed point remains close to the small amplitude limit, while it has drifted significantly for $\epsilon = 1.5$. Forces have been scaled for display purposes.

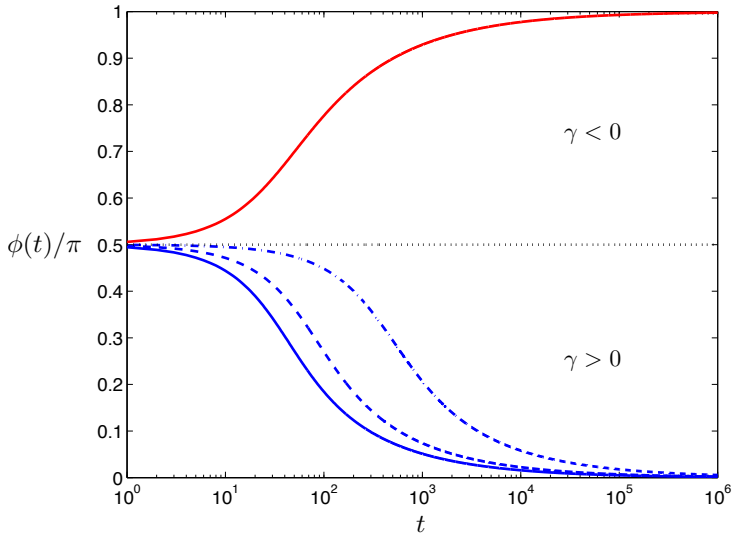

Figure 3.8: Time-evolution of the phase, from $\phi_0 = \pi/2$, in the lubrication limit with $\delta = 0.1$. The dashed line indicates $\gamma = 0$ while the solid line indicates $\gamma = \pm 0.1$, $a = 1/4$. The dashed line has $\gamma = 0.05$, $a = 1/4$ and the dash-dot line has $\gamma = 0.1$, $a = 1/8$.

3.7.3 Dynamics

The time-evolution of the phase is given in general by the integro-differential equation

$$\frac{d\phi}{dt} = -\mathcal{M}(\phi) F_x^s(\phi). \tag{3.89}$$

As noted above, in the small amplitude limit the mobility becomes independent of the phase, $\mathcal{M} = \bar{h}/2\pi$, hence in that case the dynamics is completely set by the static force. Note that the mobility is never zero so no additional fixed points arise from Eq. (3.89).

In the lubrication limit we know that there exist only two fixed points, and the location of the stable fixed point depends only on the waveform asymmetry. In Fig. 3.8 we plot the time-evolution of the phase in this limit. We see that if the system is symmetric ($\gamma = 0$), indicated by the black solid line, then the phase remains constant in time. This corresponds to the no-synchronization situation discussed in Sec. 3.3. When we introduce an asymmetry, $\gamma \neq 0$, then the two swimmers phase lock over time. When $\gamma > 0$ then $A < 0$ and the system evolves to a stable in-phase conformation, and opposite-phase for the converse. Given

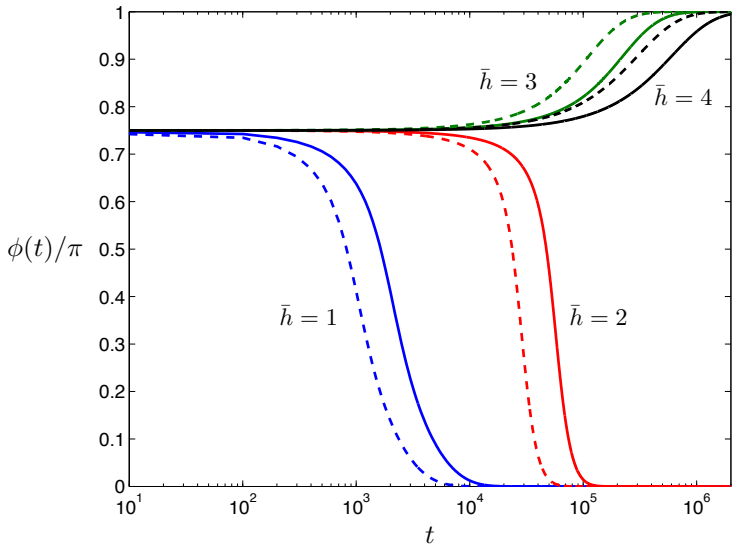

Figure 3.9: Time-evolution of the phase, from the initial condition $\phi_0 = 3\pi/4$, for $\bar{h} = [1 \to 4]$ in the small amplitude limit with $\epsilon = 0.1$. A solid line indicates $\gamma = 0.1$ while a dashed line indicates $\gamma = 0.2$.

that the amplitude, a, is reasonably small for all curves (we have the geometrical constraint $a < 1/2$), we observe roughly the same dependance of the typical time scale for phase locking, t, on the wave asymmetry and amplitude as in the small-amplitude limit (for which $t \sim a^{-4}\gamma^{-1}$, see Eq. 3.69).

We have seen above that with an increase in $\bar{h}$ comes additional fixed point, and thus we expect the phase dynamics to depend similarly on $\bar{h}$. In Fig. 3.9 we plot the time-evolution of the phase in the small amplitude limit for various values of the swimmer-swimmer distance in the case where $\gamma > 0$. Given that the phase mobility, $\mathcal{M}$, is independent of the asymmetry, and that the force is linear in γ, we find that the time scale for synchronization scales with the inverse of the asymmetry factor, i.e. $t \sim \gamma^{-1}$, as it does when $\bar{h} \ll 1$. The final stable swimmer-swimmer conformation can be understood simply by recalling the force plot in Fig. 8.6. If the initial conformation is to the left of the moving unstable point, then the sheets evolve to $\phi = 0$, while they start to the right they evolve to $\phi = \pi$. If we reverse the asymmetry of the waveforms, $\gamma < 0$, then the converse is true, the fixed point which varies with separation represents the only stable conformation for intermediate values of $\bar{h}$ and we obtain synchronization to a fixed finite phase

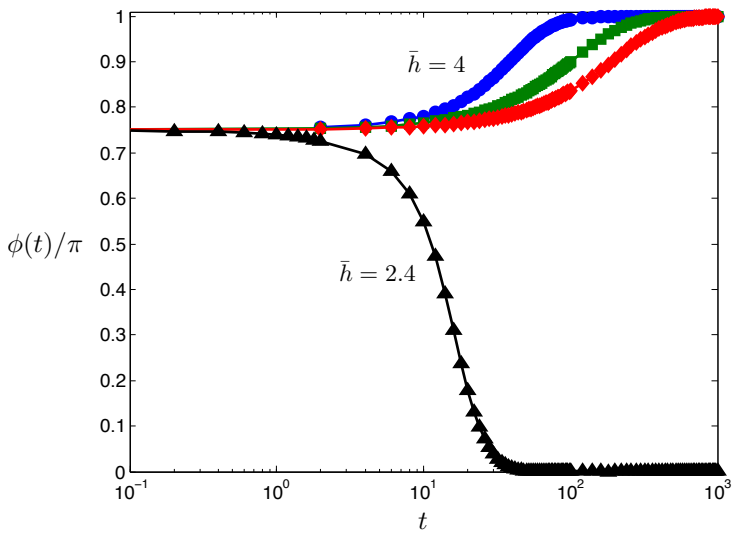

Figure 3.10: Time-evolution of the phase, from $\phi_0 = 3\pi/4$, for large amplitude waves using the boundary integral method. The circles indicate $\bar{h} = 4$, $\gamma = 0.1$, $\epsilon = 1.5$; squares: $\bar{h} = 4$, $\gamma = 0.1$, $\epsilon = 1$; diamonds: $\bar{h} = 4$, $\gamma = 0.05$, $\epsilon = 1$ and triangles: $\bar{h} = 2.4$, $\gamma = 0.1$ and $\epsilon = 1$.

difference, $0 < \phi < \pi$, as is observed in the metachronal beating of cilia.

A similar plot is shown in Fig. 3.10 in the case of large amplitude waves, using the boundary integral method, starting from an initial relative phase of $\phi = 3\pi/4$ and with a positive asymmetry, $\gamma > 0$. Again the essential physics is well captured by the small amplitude expansion: there exists a critical swimmer-swimmer separation below which the sheets evolve to the in-phase conformation. This is seen in Fig. 3.10 where with $\bar{h} = 2.4$, $\epsilon = 1$ and $\gamma = 0.1$ the sheets evolve to $\phi = 0$ (in phase) whereas when the distance is increased to $\bar{h} = 4$ the sheets evolve to $\phi = \pi$ (opposite phase). A waveform with a larger amplitude, $\epsilon = 1.5$, leads to a faster evolution of the phase than for $\epsilon = 1$ for equal asymmetry ($\gamma = 0.1$), which in turn evolves faster than for equal amplitude, $\epsilon = 1$, but lower asymmetry $\gamma = 0.05$. We note however that for large amplitude waves, the effect of increasing the amplitude on the rate of phase change is drastically reduced; in the small-amplitude limit the rate of evolution is quartic with the wave amplitude and here we see an effect which is less than cubic. Despite the reduction, the effect of amplitude is still strong and we observe drastically faster synchronization for order one amplitudes.

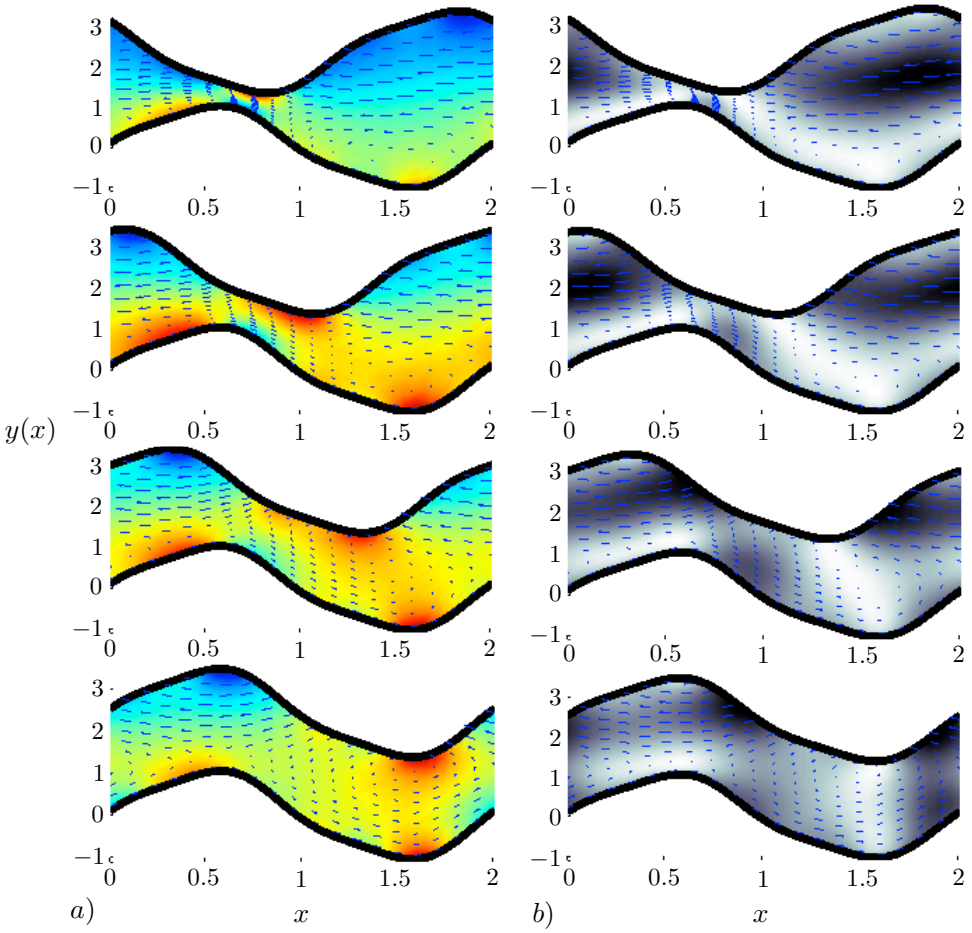

Figure 3.11: Illustration of the flow field during synchronization for $\epsilon = 1$, $\gamma = 0.1$ and $\bar{h} = 4$ using boundary integral computations; (a) flow vorticity; (b) iso values of $|\mathbf{u}|^2$. Darker regions correspond to higher velocity and vorticity, and arrows indicate instantaneous velocity vector field. The two sheets start from the initial condition $\phi_0 = 3\pi/4$ (top panel). Time increases top to bottom with the phase ϕ being equal to $\{3\pi/4, \pi/2, \pi/4, 0\}$ in the four panels.

To illustrate the flow driving the synchronizing dynamics shown in Fig. 3.10, we produce snapshots of the flow field for the $\bar{h} = 2.4$, $\epsilon = 1$, $\gamma = 0.1$ conformation in Fig. 3.11. We display the out-of-plane vorticity, ω, in Fig. 3.11a and the squared velocity field, $|\mathbf{u}|^2$, in Fig. 3.11b. Both plots are overlaid with arrows indicating the velocity vector field. The darker regions indicate higher vorticity and velocity in each plot respectively. Time increases from top to bottom, and we show the instances where the phase angle is given by $\phi = \{3\pi/4, \pi/2, \pi/4, 0\}$, corresponding to relative velocity of the sheets, $U_\Delta = \{0.0325, 0.1223, 0.1097, 0\}$.

3.8 Conclusion

3.8.1 Summary of results

In this chapter we have considered, as a model for the synchronization of flagellated cells, the relative motion of two free-swimming planar parallel sheets propagating waves of transverse displacement. We showed that due to the kinematic reversibility of the Stokes equations, waveform conformations with both vertical and horizontal axis symmetry could not yield synchronizing dynamics. When we break vertical axis symmetry, the phase of the system evolves to stable dynamic equilibria whose position is entirely dependent on the geometry of flagellar waveforms, and the distance between them.

When the swimmers are close together we are able to make use of the lubrication equations and find two fixed points, in-phase and opposite-phase. The location of the stable point depends on the nature of the asymmetry, which is measured by an integral over the waveform geometry. If the front-back asymmetry of the geometry is reversed thus is equivalent to reversing the kinematics of the problem which yields a reversal of forces. In other words, stable points become unstable and vice versa. In contrast, the energy dissipation is always a minimum for the in-phase conformation, and indicates the possibility of phase-locking into a conformation of maximum energy dissipation.

An expansion in small amplitude is utilized to introduce inextensible boundary conditions and order one distances between the organisms. In this case there

arise additional fixed points, whose location and nature depends on the cells geometry and separation. Among the possibilities is synchronization at a stable intermediate phase between in-phase and opposite-phase.

Finally, we presented numerical results for large-amplitude waves using the boundary integral method. The computational results indicate that between the lubrication limit and the small amplitude expansion, all the relevant physics can be captured analytically. However, since the phase locking force depends so strongly on waveform amplitude, we observe much faster synchronization for large amplitudes, as might be expected.

3.8.2 Two-dimensional modeling and collective locomotion

The two dimensional model used here is admittedly too simple to provide quantitative predictions for real microorganisms. However the simplicity allows analytic formulae to be derived and a mathematical structure elucidating the interaction between the bodies due to the Stokesian flow to be obtained, and gives an explicit description of the effect of symmetry breaking. The intuition garnered here may then be useful for more complex models, with finite three-dimensional bodies, that must be solved entirely numerically.

We first note that, as a result of the two-dimensional approach, the viscous mobility of the cells in the direction perpendicular to that of the wave propagation is strictly equal to zero. Additionally there is no dynamic component to the vertical force (see Appendix A.2). For real microorganisms, however, this is not the case and hence fluid forces will determine the separation between the swimmers dynamically. Since swimming cells are force-free, the far-field velocity is typically a force dipole. In particular spermatozoa have a positive force dipole (so-called pushers [10]). Far-field interactions between pushers tend to both align the major axis of pushers drive them together. Accordingly experimental evidence suggests that as spermatozoa synchronize they come together very tightly [4] (see also Fig. 1.1). In light of this, the lubrication limit is perhaps the relevant physical limit to consider for the phase locking of swimming cells. In contrast, eukaryotic cilia are attached to a substrate at a fixed distance which is varies depending on the organism [9].

In addition, the two-dimensional limit offers one particularity, which is that the fluid between the swimmers (inner problem) does not communicate with that outside the swimmers (outer problem). The outer problem, that addressed by Taylor, is purely kinematic, in the sense that the speed of the sheet relative to the flow at infinity is uniquely determined without resorting to a balance of forces, unlike the inner problem. Further to this, because the outer problem cannot impose a force on the outer surface of the sheet, the forces are individually zero for the inner problem and therefore the inner problem (or even arbitrarily many inner problems) may be solved separately because a balance with the outer problem is not required. Now if a rigid body motion $\mathbf{U} = U_{\Delta}\mathbf{e}_x$ (due to the inner problem) is added to the surface deformations of the outer problem it has the sole effect of adding a plug flow solution to the swimming problem: in the zero Reynolds number limit a rigid body motion of two dimensional surface diffuses to infinity instantaneously. An interesting consequence of this is that when there arises a nonzero relative velocity, the idea of collective motion loses meaning, even for identical sheets, as in the frame moving with lower sheet (see Fig. 7.1) we find different values for the flow at infinity, U when $y \to -\infty$ and $U + U_{\Delta}$ when $y \to \infty$. Further, if the sheets are different, then even if the inner problem demands $U_{\Delta} = 0$, the outer problem on either side produces flows at infinity (in the frame moving with the sheets) which are distinct. However, even in the three dimensional case when the swimmers are the same, synchronization is clearly driven by the forces between the bodies and those forces will dominate when the cells are close; because of this we expect to garner the leading order behavior from analysis of the inner problem.

Chapter 3, in part, is a reprint of the material as it appears in Physical Review Letters 2009. Elfring, Gwynn J.; Lauga, Eric, the American Physical Society, 2009. The dissertation author was the primary investigator and author of this paper.

Chapter 3, in part, is a reprint of the material as it appears in Physics of Fluids 2011. Elfring, Gwynn J.; Lauga, Eric, the American Institute of Physics, 2011. The dissertation author was the primary investigator and author of this paper.

Chapter 4

Finite size effects

4.1 Introduction

In the previous chapter we observed that if the shape of the swimmers was too symmetric then the kinematic reversibility of the field equations, coupled with that symmetry, would permit no evolution of the phase difference between two swimmers. Now if the swimmers are finite, swimmers propagating sinusoidal waves will, except for brief instances in time, always have a front/back asymmetry. Furthermore that asymmetry is not stationary but is time dependent as the swimmer actuates itself. It is therefore critical in understanding the nature of two-body interactions to develop a finite model and to study its properties.

In this chapter we develop a three dimensional, finite-size model using slenderbody theory hydrodynamics to describe the thin flagella. Additionally, we include a spherical head for each swimmer and include hydrodynamic interactions between each swimmer using Faxén relations. We first constrain the dynamics of the swimmers to include only relative (horizontal) translation, mimicking the two-dimensional problem from the previous chapter but here with slender filaments, to observe that finite-size effects present sufficient asymmetry (even for headless, symmetric swimmers) to produce synchronizing flow fields. When attraction and rotations are introduced we find that swimmers with heads display strong dipole-dipole interactions which lead to attraction of the swimmers on a timescale much faster than synchronization.

4.2 Kinematics

We have two swimmers, labeled 1 and 2. These swimmers are coplanar meaning that their flagella both propagate waves of transverse oscillations which are in the same plane. We note that this assumption is quite strong since swimmers certainly are less likely than not both to be propagating waves in the plane spanned by their two velocity vectors. Nevertheless, since we seek a course-grained understanding of the natural physics, we presume the approximation is reasonable as a first step. The kinematics of the swimmers are described by time dependent position vectors $\mathbf{X}_1(s-ct)$ and $\mathbf{X}_2(s-ct)$ where $\mathbf{X}(s) = [X(s), Y(s)]$ and $s \in [-L, L]$ is the arclength along the flagellum yielding a total length of $2L$ for each one of the swimmers. As mentioned we have two such organisms but we do not distinguish between them below as the same formulation will be used for both. If we define the head of the organism as $\mathbf{x}^h(t)$ then the only difference is that we take $\mathbf{x}_1^h(0) = \mathbf{0}$ for convenience while $\mathbf{x}_2^h(0) = \Delta\mathbf{x}^h(0)$, i.e. some position for example $\Delta\mathbf{x}^h(0) = h\mathbf{e}_y$ if one is directly above the other. Given that the flagella pass periodic traveling waves they satisfy

$$X(s+\lambda/\alpha) = X(s) + \lambda, \quad Y(s+\lambda/\alpha) = Y(s), \tag{4.1}$$

where λ is the wavelength and λ/α is the distance along the flagella between wavelengths. Note that here c is the wave speed along the arclength s while αc is the wave speed along X. We stipulate that the center of the head is in line with the tangent vector of the flagellum at the point where the flagellum meets the head ($s = 0$). Following [41], the entire centerline may be written as

$$\mathbf{x}(s,t) = \mathbf{x}^h(t) + \mathbf{\Theta}(t) \cdot \mathbf{R}(s,t), \tag{4.2}$$

where $\mathbf{R} = R^h\mathbf{X}_s(-L-ct) + \mathbf{X}(s-ct) - \mathbf{X}(-L-ct)$ and R^h is the radius of the head. The two-dimensional rotation operator is defined

$$\mathbf{\Theta}(t) = \begin{bmatrix} \cos\theta(t) & -\sin\theta(t) \\ \sin\theta(t) & \cos\theta(t) \end{bmatrix}. \tag{4.3}$$

At $t = 0$ the rotation operator is the identity tensor $\mathbf{\Theta} = \mathbf{I}$.

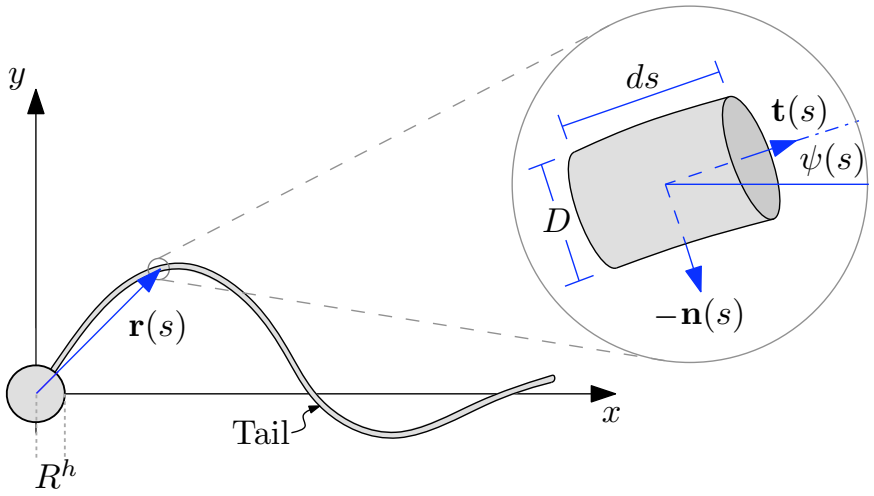

Figure 4.1: Figure for a single filament adapted from Yu et al. [42]. There is a second swimmer whose head is located at $\Delta\mathbf{x}^h$.

Now if we differentiate the position we obtain

$$\mathbf{u}(s,t) = \dot{\mathbf{x}}^h(t) + \boldsymbol{\Theta}\cdot\dot{\mathbf{R}} + \dot{\theta}\boldsymbol{\Theta}\cdot\mathbf{R}^\perp. \tag{4.4}$$

We can write $\dot{\mathbf{R}} = -cR^h\mathbf{X}_{ss}(-L-ct) - c\mathbf{X}_s(s-ct) + c\mathbf{X}_s(-L-ct)$ by exploiting the functional dependence to exchange derivatives. Furthermore our position vectors are in the plane, $\mathbf{X} = [X, Y]$ and $\mathbf{X}^\perp = \mathbf{e}_z \times \mathbf{X} = [-Y, X]$. Written compactly we have

$$\mathbf{u}(s,t) = \dot{\mathbf{x}}^h + \dot{\theta}\mathbf{r}^\perp + \dot{\mathbf{r}}, \tag{4.5}$$

where

$$\mathbf{r}^\perp = \boldsymbol{\Theta}\cdot\left\{R^h\mathbf{X}_s^\perp(-L-ct) + \mathbf{X}^\perp(s-ct) - \mathbf{X}^\perp(-L-ct)\right\}, \tag{4.6}$$

$$\dot{\mathbf{r}} = c\boldsymbol{\Theta}\cdot\left\{-R^h\mathbf{X}_{ss}(-L-ct) + \mathbf{X}_s(-L-ct) - \mathbf{X}_s(s-ct)\right\}. \tag{4.7}$$

Here we use the convention that the lower case vectors are in the lab frame and so we write, for example, the tangent vector to the flagella in the lab frame is $\mathbf{t} = \mathbf{r}_s = \boldsymbol{\Theta}\cdot\mathbf{X}_s$ while the normal $\mathbf{n} = \mathbf{t}^\perp$. We see the motion of the swimmer is comprised of three components: the translation of the head $\dot{\mathbf{x}}^h$, the rotation of the swimmer relative to the center of the head $\dot{\theta}\mathbf{r}^\perp$ and the swimming gait $\dot{\mathbf{r}}$.

We define the shape of the swimmer by specifying the tangent angle, $\psi(s,t)$, made with the X-axis

$$\psi_1(s) = \arctan\left[\frac{Y_s}{X_s}\right]. \tag{4.8}$$

In other words $\mathbf{X}_s = [\cos\psi, \sin\psi]$. We see also from this definition that $\mathbf{X}_{ss} = \mathbf{X}_s^{\perp}\psi_s$.

We then integrate these ode's to obtain

$$\mathbf{R} = R^h\mathbf{X}_s(-L-ct) + \int_{-L}^{s}\mathbf{X}_s ds. \tag{4.9}$$

We prescribe the tangent angle to be composed in terms of a Fourier basis

$$\psi(s,t) = \sum a_n \cos\left[n\frac{\pi}{L}(s-ct)\right]. \tag{4.10}$$

4.2.1 Head kinematics

The vector pointing from the center of the sphere to the point where the flagellum meets the sphere $\mathbf{r}^h \equiv \mathbf{r}(-L,t)$ may be written

$$\mathbf{r}^h = \mathbf{x}(-L,t) - \mathbf{x}^h = R^h\mathbf{\Theta}\cdot\mathbf{X}_s(-L,t). \tag{4.11}$$

The evolution of this vector in time is

$$\begin{aligned}\frac{\partial\mathbf{r}^h}{\partial t} &= (\dot\theta + \dot\psi^h)R^h\mathbf{\Theta}\cdot\mathbf{X}_s^{\perp}(-L,t),\\ &= (\dot\theta + \dot\psi^h)\mathbf{e}_z \times R^h\mathbf{\Theta}\cdot\mathbf{X}_s(-L,t),\\ &= \boldsymbol{\omega}^h \times \mathbf{r}^h,\end{aligned} \tag{4.12}$$

where $\psi^h \equiv \psi(-L,t)$. So we see that by prescribing the kinematics as we have, the rotation of the head $\boldsymbol{\omega}^h = (\dot\theta + \dot\psi^h)\mathbf{e}_z$ consists of two components, a rigid body rotation of the entire body, $\dot\theta$, along with a rotation of the head due to the prescribed gait, $\dot\psi^h$.

4.3 Hydrodynamics

4.3.1 Slender body theory

As we saw in chapter 3 the flow field in the zero Reynolds number limit may be represented exactly by an integral of single and double layer kernels over the surface of a body. However, when the body is slender one may replace the surface distribution of singularities with a line distribution along the slender body's centerline for a formulation which is asymptotically valid with accuracy dependent on the formulation and ultimately the slenderness. There have been many many derivations of the slender body equations with varying asymptotic validity [43, 44, 31, 45, 46, 47]. We follow here the formal approach developed by Götz [47] which includes a complete spectral theory for the integral operator. The force (density) on a flagella $\mathbf{f}_1$ at position $\mathbf{x}_1(s)$, parameterized by the arclength, s, of a slender body (as shown in Fig. 4.1) may be described asymptotically (using the notation of Tornberg and Gustavsson [48]) as

$$\mathbf{u}_1(\mathbf{x}_1) = \mathcal{L}_1[\mathbf{f}_1](s) + \mathcal{K}_1[\mathbf{f}_1](s) + \mathbf{u}_{\to 1f}[\mathbf{F}_1, \mathbf{F}_2, \mathbf{f}_2](s) + \mathcal{O}(\epsilon), \tag{4.13}$$

where the slenderness parameter $\epsilon = a/2L$ is a ratio of the radius of the flagella a to its total length $2L$. Note that the term $\mathbf{u}_{\to 1f}$ is our notation for the flow acting on flagellum 1. The local term is given by

$$\mathcal{L}_1[\mathbf{f}_1](s) = -\frac{1}{8\pi\mu}\left[(\mathbf{I} + \mathbf{t}_1(s)\mathbf{t}_1(s))\ln(\epsilon^{-2}) + \mathbf{I} - 3\mathbf{t}_1(s)\mathbf{t}_1(s)\right]\cdot\mathbf{f}_1(s), \tag{4.14}$$

where $\mathbf{t}(s)$ is the local tangent to the filament. We note this operator represents resistive force theory in the limit $\epsilon \to 0$.

The flagellum also interacts with its own flow field. This term is given by the nonlocal operator

$$\mathcal{K}_1[\mathbf{f}_1](s) = -\frac{1}{8\pi\mu}\int_{-L_1}^{L_1}\left[\mathbf{G}\left(\mathbf{x}_1(s) - \mathbf{x}_1(s')\right)\cdot\mathbf{f}_1(s') - \left(\frac{\mathbf{I} + \mathbf{t}_1\mathbf{t}_1}{|s - s'|}\right)\cdot\mathbf{f}_1(s)\right]ds'. \tag{4.15}$$

For a single swimmer this formulation is accurate to $\mathcal{O}(\epsilon^2 \ln\epsilon)$, where it has been assumed the radius of the flagella is given by $\rho(s) = 2\epsilon\sqrt{s(L-s)}$ [46]; however,

since we will ultimately include only the leading order interaction with the background flow in the method of reflections the accuracy of the overall scheme is reduced to $\mathcal{O}(\epsilon)$ [48].

The flow field due the the flagellum at some field point $\mathbf{x}$ which is not on the body is given simply by a distribution of Stokeslets and potential dipoles

$$\mathbf{u}_{1f} = -\frac{1}{8\pi\mu}\int_{-L_1}^{L_1} \mathbf{S}_f(\mathbf{x}-\mathbf{x}_1(s'))\cdot\mathbf{f}_1(s')ds', \tag{4.16}$$

where $\mathbf{S}_f(\mathbf{x}) = \mathbf{S}(\mathbf{x};\frac{a^2}{2})$. We note that the relevance of the potential dipole term is very small for distances much larger than a from the flagellum.

4.3.2 Heads

The translational motion of a sphere in Stokes flow is given by the equation

$$\dot{\mathbf{x}}_1^h = -\mathcal{M}_1^t\mathbf{F}_1 + \mathcal{F}_1^t\mathbf{u}_{\to 1h} + \mathcal{O}\left(\frac{R^h}{\left|\mathbf{x}_1^h-\mathbf{x}\right|}\right)^4. \tag{4.17}$$

The translational mobility for a sphere is simply $\mathcal{M}_1^t = [6\pi\mu R_1^h]^{-1}$ and the translational Faxén operator for a sphere is $\mathcal{F}_1^t = \left(1+\frac{1}{6}(R_1^h)^2\nabla^2\right)$. Here $\mathbf{F}_1$ is the hydrodynamic force on the head. The hydrodynamic interactions are included up to the first reflection via the Faxén laws. The notation $\mathbf{u}_{\to 1h}$ indicates the background flow field acting on the head of the first swimmer.

The rotational motion of a sphere is given by

$$\left(\dot{\theta}_1+\dot{\psi}_1\right) = -\mathcal{M}_1^\theta T_1 + \left(\mathcal{F}_1^\theta\mathbf{u}_{\to 1h}\right)\cdot\mathbf{e}_z + \mathcal{O}\left(\frac{R^h}{\left|\mathbf{x}_1^h-\mathbf{x}\right|}\right)^7. \tag{4.18}$$

The rotational mobility for a sphere is simply $\mathcal{M}_1^\theta = [8\pi\mu(R_1^h)^3]^{-1}$ while the rotational Faxén operator for a sphere is $\mathcal{F}_1^\theta = \frac{1}{2}\boldsymbol{\nabla}\times$. The hydrodynamic torque on the spherical head is $T_1\mathbf{e}_z$ (if this is zero then the sphere rotates with half the vorticity of the flow).

One might wonder about the effect of the hydrodynamic interactions where the tail meets the head. In this region the dropped terms, while decaying very

rapidly are still order one (not diverging). However this region is small hence on average the tail is far from the head.

The flow field created by each head (individually) is given exactly by

$$\mathbf{u}_{1h} = -\frac{1}{8\pi\mu}\left(1 + \frac{(R^h)^2}{6}\nabla^2\right)\mathbf{G}(\mathbf{x}-\mathbf{x}_1^h)\cdot\mathbf{F}_1 - \frac{1}{8\pi\mu}T_1\mathbf{e}_z \times \frac{\mathbf{x}}{|\mathbf{x}|^3}, \tag{4.19}$$

$$= -\frac{1}{8\pi\mu}\left[\mathbf{S}_h(\mathbf{x}-\mathbf{x}_1^h)\cdot\mathbf{F}_1 + \mathbf{v}(\mathbf{x}-\mathbf{x}_1^h)T_1\right]. \tag{4.20}$$

where $\mathbf{S}_h(\mathbf{x}) = \mathbf{S}(\mathbf{x}; \frac{(R^h)^2}{3})$. The rotlet in this problem has only one relevant component, $\mathbf{e}_z \cdot \mathbf{\Omega} = -\mathbf{v}(\mathbf{x})$, where

$$\mathbf{v}(\mathbf{x}) = \frac{\mathbf{x}^\perp}{|\mathbf{x}|^3}. \tag{4.21}$$

4.3.3 Hydrodynamic interactions

The leading order component of the background flow felt by the flagellum is the flow generated by its head as well as the head and flagellum of the neighboring swimmer. Conversely the flow felt by the head stems from its own flagellum along with the flow generated by the other swimmer:

$$\mathbf{u}_{\to 1f}[\mathbf{F}_1, \mathbf{F}_2, \mathbf{f}_2](\mathbf{x}_1(s)) = \mathbf{u}_{1h}[\mathbf{F}_1](s) + \mathbf{u}_{2h}[\mathbf{F}_2](s) + \mathbf{u}_{2f}[\mathbf{f}_2](s), \tag{4.22}$$

$$\mathbf{u}_{\to 1h}[\mathbf{f}_1, \mathbf{f}_2, \mathbf{F}_2](\mathbf{x}_1^h) = \mathbf{u}_{1f}[\mathbf{f}_1] + \mathbf{u}_{2f}[\mathbf{f}_2] + \mathbf{u}_{2h}[\mathbf{F}_2]. \tag{4.23}$$

This flow satisfies no boundary conditions in general but the reflections produce higher order effects as indicated above.

In summary the equations which govern the dynamics of each swimmer are

$$\dot{\mathbf{x}}_1^h + \dot{\theta}_1\mathbf{r}_1^\perp(s) + \dot{\mathbf{r}}_1(s) = \mathcal{L}_1[\mathbf{f}_1](s) + \mathcal{K}_1[\mathbf{f}_1](s) + \mathbf{u}_{1h}[\mathbf{F}_1](s) + \mathbf{u}_{2h}[\mathbf{F}_2](s) + \mathbf{u}_{2f}[\mathbf{f}_2](s), \tag{4.24}$$

$$\dot{\mathbf{x}}_1^h = -\mathcal{M}^t\mathbf{F}_1 + \mathcal{F}_1^t(\mathbf{u}_{1f}[\mathbf{f}_1] + \mathbf{u}_{2f}[\mathbf{f}_2] + \mathbf{u}_{2h}[\mathbf{F}_2]), \tag{4.25}$$

$$\dot{\theta}_1 + \dot{\psi}_1^h = -\mathcal{M}^\theta T_1 + \mathcal{F}_1^\theta\left(\mathbf{u}_{1f}[\mathbf{f}_1] + \mathbf{u}_{2f}[\mathbf{f}_2] + \mathbf{u}_{2h}[\mathbf{F}_2]\right)\cdot\mathbf{e}_z. \tag{4.26}$$

and the equations for the second swimmer follow by exchanging $1 \leftrightarrow 2$. The exact expression of the Faxén operators on each component of the background flow is

given in the following section. These equations are closed by stipulating that both swimmers are force and torque free

$$\int_{-L_1}^{L_1} \mathbf{f}_1(s)ds = -\mathbf{F}_1, \tag{4.27}$$

$$\int_{-L_1}^{L_1} \tilde{\mathbf{r}}_1^{\perp}(s) \cdot \mathbf{f}_1(s)ds = -T_1. \tag{4.28}$$

4.3.4 Background flow terms

To compute the effects of the background flow terms the following formulae are useful and follow directly from the identities given earlier, $\nabla^2 \mathbf{S}_f = 2\mathbf{D}$, $\nabla^2 \mathbf{S}_h = 2\mathbf{D}$, $\boldsymbol{\nabla} \times \mathbf{S}_f = 2\boldsymbol{\Omega}$ and $\boldsymbol{\nabla} \times \mathbf{S}_h = 2\boldsymbol{\Omega}$.

For the heads we have

$$\begin{aligned}\mathcal{F}_1^t \mathbf{u}_{1f}[\mathbf{f}_1] &= -\frac{1}{8\pi\mu}\left(1 + \frac{(R_1^h)^2}{6}\nabla^2\right)\int_{-L_1}^{L_1} \mathbf{S}_f(\mathbf{x} - \mathbf{x}_1(s')) \cdot \mathbf{f}_1(s')ds'\Big|_{\mathbf{x}=\mathbf{x}_1^h}, \\ &= -\frac{1}{8\pi\mu}\int_{-L_1}^{L_1} \mathbf{S}_{hf}(\mathbf{x}_1^h - \mathbf{x}_1(s')) \cdot \mathbf{f}_1(s')ds', \end{aligned} \tag{4.29}$$

where $\mathbf{S}_{hf}(\mathbf{x}) = \mathbf{S}\left(\mathbf{x}; \frac{1}{6}\left(2(R_1^h)^2 + 3a^2\right)\right)$.

Similarly

$$\mathcal{F}_1^t \mathbf{u}_{2f}[\mathbf{f}_2] = -\frac{1}{8\pi\mu}\int_{-L_2}^{L_2} \mathbf{S}_{hf}(\mathbf{x}_1^h - \mathbf{x}_2(s')) \cdot \mathbf{f}_2(s')ds', \tag{4.30}$$

while

$$\begin{aligned}\mathcal{F}_1^t \mathbf{u}_{2h}[\mathbf{F}_2, T_2] &= -\frac{1}{8\pi\mu}\left(1 + \frac{(R_1^h)^2}{6}\nabla^2\right)\left[\mathbf{S}_h(\mathbf{x} - \mathbf{x}_2^h) \cdot \mathbf{F}_2 + T_2\boldsymbol{\Omega}(\mathbf{x} - \mathbf{x}_2^h) \cdot \mathbf{e}_z\right]\Big|_{\mathbf{x}=\mathbf{x}_1^h}, \\ &= -\frac{1}{8\pi\mu}\left[\mathbf{S}_{hh}(\mathbf{x}_1^h - \mathbf{x}_2^h) \cdot \mathbf{F}_2 + \mathbf{v}(\mathbf{x}_1^h - \mathbf{x}_2^h)T_2\right], \end{aligned} \tag{4.31}$$

where $\mathbf{S}_{hh}(\mathbf{x}) = \mathbf{S}\left(\mathbf{x}; \frac{1}{3}\left[(R_1^h)^2 + (R_2^h)^2\right]\right)$.

The rotational terms are

$$\mathcal{F}_1^\theta \mathbf{u}_{1f}[\mathbf{f}_1]\cdot\mathbf{e}_z = -\frac{1}{2(8\pi\mu)}\boldsymbol{\nabla}\times\int_{-L_1}^{L_1}\mathbf{S}_f(\mathbf{x}-\mathbf{x}_1(s'))\cdot\mathbf{f}_1(s')ds'\cdot\mathbf{e}_z\Big|_{\mathbf{x}=\mathbf{x}_1^h},$$
$$= \frac{1}{8\pi\mu}\int_{-L_1}^{L_1}\mathbf{v}(\mathbf{x}_1^h-\mathbf{x}_1(s'))\cdot\mathbf{f}_1(s')ds', \tag{4.32}$$

while similarly

$$\mathcal{F}_1^\theta \mathbf{u}_{2f}[\mathbf{f}_2]\cdot\mathbf{e}_z = \frac{1}{8\pi\mu}\int_{-L_2}^{L_2}\mathbf{v}(\mathbf{x}_1^h-\mathbf{x}_2(s'))\cdot\mathbf{f}_2(s')ds', \tag{4.33}$$

and finally

$$\mathcal{F}_1^\theta \mathbf{u}_{2h}[\mathbf{F}_2,T_2]\cdot\mathbf{e}_z = -\frac{1}{2(8\pi\mu)}\boldsymbol{\nabla}\times\left[\mathbf{S}_h(\mathbf{x}-\mathbf{x}_2^h)\cdot\mathbf{F}_2+T_2\boldsymbol{\Omega}(\mathbf{x}-\mathbf{x}_2^h)\cdot\mathbf{e}_z\right]\cdot\mathbf{e}_z\Big|_{\mathbf{x}=\mathbf{x}_1^h},$$
$$= \frac{1}{8\pi\mu}\left[\mathbf{v}(\mathbf{x}_1^h-\mathbf{x}_2^h)\cdot\mathbf{F}_2-\frac{1}{2}\left|\mathbf{x}_1^h-\mathbf{x}_2^h\right|^{-3}T_2\right]. \tag{4.34}$$

4.3.5 Non-dimensionalizing

First we wish to make the swimmers similar in the sense they have the same shape hence $R_1^h = R_2^h = R^h$ and $L_1 = L_2 = L$. We then rescale all lengths by L. Times are non-dimensionalized by L/c and forces by $\mu c/L$ hence the preceding equations are modified by the maps $a \to 2\epsilon$, $L_1 \to 1$ and $\mu \to 1$. It follows that

$$\mathbf{S}_f(\mathbf{x}) = \mathbf{S}(\mathbf{x}; 2\epsilon^2), \tag{4.35}$$
$$\mathbf{S}_h(\mathbf{x}) = \mathbf{S}(\mathbf{x}; \frac{1}{3}(R^h)^2), \tag{4.36}$$
$$\mathbf{S}_{hf}(\mathbf{x}) = \mathbf{S}(\mathbf{x}; \frac{1}{3}\left((R^h)^2+6\epsilon^2\right)), \tag{4.37}$$
$$\mathbf{S}_{hh}(\mathbf{x}) = \mathbf{S}(\mathbf{x}, \frac{2}{3}(R^h)^2). \tag{4.38}$$
$$\tag{4.39}$$

4.4 Numerical implementation

To solve the equations of motion we project the integral equations for the motion of the flagellum onto a Legendre basis. The reason for this approach is

because the Legendre polynomials P_i are eigenfunctions of the singular part of the non-local operator and a spectral theory exists which guarantees convergence [47]. Projecting the governing equations for the first swimmer onto the ith polynomial yields

$$\langle \mathcal{L}_1[\mathbf{f}_1]P_i\rangle + \langle \mathcal{K}_1[\mathbf{f}_1]P_i\rangle + \langle \mathbf{u}_{1h}[\mathbf{F}_1]P_i\rangle + \langle \mathbf{u}_{2h}[\mathbf{F}_2]P_i\rangle\,, \tag{4.40}$$

$$+ \langle \mathbf{u}_{2f}[\mathbf{f}_2]P_i\rangle - \left\langle \dot{\mathbf{x}}_1^h P_i\right\rangle - \left\langle \dot{\theta}_1 \mathbf{r}_1^\perp P_i\right\rangle = \langle \dot{\mathbf{r}}_1 P_i\rangle\,, \tag{4.41}$$

$$-\mathcal{M}^t\mathbf{F}_1 + \mathcal{F}^t(\mathbf{u}_{1f}[\mathbf{f}_1] + \mathbf{u}_{2f}[\mathbf{f}_2] + \mathbf{u}_{2h}[\mathbf{F}_2]) - \dot{\mathbf{x}}_1^h = \mathbf{0}, \tag{4.42}$$

$$-\mathcal{M}^\theta T_1 + \mathcal{F}_1^\theta\left(\mathbf{u}_{1f}[\mathbf{f}_1] + \mathbf{u}_{2f}[\mathbf{f}_2] + \mathbf{u}_{2h}[\mathbf{F}_2]\right)\cdot\mathbf{e}_z - \dot{\theta}_1 = \dot{\psi}_1^h, \tag{4.43}$$

$$\langle \mathbf{f}_1(s)\rangle + \mathbf{F}_1 = \mathbf{0}, \tag{4.44}$$

$$\left\langle \tilde{\mathbf{r}}_1^\perp(s)\cdot\mathbf{f}_1(s)\right\rangle + T_1 = 0. \tag{4.45}$$

Similarly for the second swimmer we have

$$\langle \mathcal{L}_2[\mathbf{f}_2]P_i\rangle + \langle \mathcal{K}_2[\mathbf{f}_2]P_i\rangle + \langle \mathbf{u}_{2h}[\mathbf{F}_2]P_i\rangle + \langle \mathbf{u}_{1h}[\mathbf{F}_1]P_i\rangle\,, \tag{4.46}$$

$$+ \langle \mathbf{u}_{1f}[\mathbf{f}_1]P_i\rangle - \left\langle \dot{\mathbf{x}}_2^h P_i\right\rangle - \left\langle \dot{\theta}_2 \mathbf{r}_2^\perp P_i\right\rangle = \langle \dot{\mathbf{r}}_2 P_i\rangle\,, \tag{4.47}$$

$$-\mathcal{M}^t\mathbf{F}_2 + \mathcal{F}^t(\mathbf{u}_{2f}[\mathbf{f}_2] + \mathbf{u}_{1f}[\mathbf{f}_1] + \mathbf{u}_{1h}[\mathbf{F}_1]) - \dot{\mathbf{x}}_2^h = \mathbf{0}, \tag{4.48}$$

$$-\mathcal{M}^\theta T_2 + \mathcal{F}^\theta\left(\mathbf{u}_{2f}[\mathbf{f}_2] + \mathbf{u}_{1f}[\mathbf{f}_1] + \mathbf{u}_{1h}[\mathbf{F}_1]\right)\cdot\mathbf{e}_z - \dot{\theta}_2 = \dot{\psi}_2^h, \tag{4.49}$$

$$\langle \mathbf{f}_2(s)\rangle + \mathbf{F}_2 = \mathbf{0}, \tag{4.50}$$

$$\left\langle \tilde{\mathbf{r}}_2^\perp(s)\cdot\mathbf{f}_2(s)\right\rangle + T_2 = 0. \tag{4.51}$$

We use short-hand notation for the integration, $\langle g\rangle \equiv \int_{-1}^{1} g ds$. The unknowns are $\mathbf{F}_n$, T_n, $\dot{\mathbf{x}}_n^h$ and $\dot{\theta}_n$ and $\mathbf{f}_n$ which is decomposed into a Legendre basis

$$\mathbf{f}_n = \sum_{j=0}^{N-1} \mathbf{a}_j P_j(s). \tag{4.52}$$

With the above in the previous equations, and taking $i \in [0, N-1]$, we end up with $4N + 12$ equations for the unknowns.

These equations constitute a linear system of the form $\boldsymbol{A}\cdot\boldsymbol{a} = \boldsymbol{b}$ where $\boldsymbol{a}$

and $\boldsymbol{b}$ are $4N + 12$ vectors, as shown below

$$\boldsymbol{a} = \begin{pmatrix} \mathbf{a}_{10} \\ : \\ \mathbf{a}_{1N-1} \\ \mathbf{F}_1 \\ T_1 \\ \dot{\mathbf{x}}_1^h \\ \dot{\theta}_1 \\ \mathbf{a}_{20} \\ : \\ \mathbf{a}_{2N-1} \\ \mathbf{F}_2 \\ T_2 \\ \dot{\mathbf{x}}_2^h \\ \dot{\theta}_2 \end{pmatrix}, \qquad \boldsymbol{b} = \begin{pmatrix} \langle \dot{\mathbf{r}}_1 P_0 \rangle \\ : \\ \langle \dot{\mathbf{r}}_1 P_{N-1} \rangle \\ \mathbf{0} \\ \dot{\psi}_1^h \\ \mathbf{0} \\ 0 \\ \langle \dot{\mathbf{r}}_2 P_0 \rangle \\ : \\ \langle \dot{\mathbf{r}}_2 P_{N-1} \rangle \\ \mathbf{0} \\ \dot{\psi}_2^h \\ \mathbf{0} \\ 0 \end{pmatrix}. \tag{4.53}$$

The linear operator $\boldsymbol{A}$ is comprised of the following terms: $\boldsymbol{L}$ local flagella hydrodynamic effects, $\boldsymbol{K}$ non-local hydrodynamic interactions, $\boldsymbol{S}_f$ flagella-flagella hydrodynamic interactions, $\boldsymbol{S}_h$ head on flagella interactions, $\boldsymbol{U}_f$ flagella rigid body motion, $\boldsymbol{H}_f$ flagella on head interactions, $\boldsymbol{H}_h$ head-head interactions, $\boldsymbol{U}_h$ head rigid body motion, $\boldsymbol{F}$ force and torque free equations. Hence

$$\boldsymbol{A} \cdot \boldsymbol{a} = (\boldsymbol{L} + \boldsymbol{K} + \boldsymbol{T} + \boldsymbol{S}_f + \boldsymbol{S}_h + \boldsymbol{U}_f + \boldsymbol{H}_f + \boldsymbol{H}_h + \boldsymbol{U}_h + \boldsymbol{F}) \cdot \boldsymbol{a} = \boldsymbol{b}. \tag{4.54}$$

In practice we also construct each individual term as a separate matrix which allows flexibility and clarity in implementation at the expense of memory. Details on the construction of each of these terms is provided in Appendix B. Our unknown coefficients are found by solution of the linear system.

4.4.1 Discontinuity

The non-local operator $\boldsymbol{K}$ contains a jump discontinuity when $s = s'$. To ensure we don't integrate a slope through this point we split the integration at s,

$$\int_{-1}^{1} ds' \to \int_{-1}^{s} ds' + \int_{s}^{1} ds', \tag{4.55}$$

and then choose a integration scheme which does not sample that point such as Gauss-Legendre quadrature. The main problem with this is that since we are also ultimately integrating over s to project the equation we will have to change the Gauss-Legendre weights N times, but we do this ahead of time outside the time loop.

4.4.2 Time stepping

At each point in time we will compute the unknowns $\mathbf{f}$, $\mathbf{F}$, T, $\dot{\mathbf{x}}^h$ and $\dot{\theta}$. We then integrate the position forward in time to obtain the new position. Note the time scale for a half cycle is $T = L/c$ so our time steps Δt should be such that $\Delta t \ll T/n$ where n is the number of Fourier modes used to represent the tangent angle of the flagellum. We must integrate in time explicitly, since we store the solution vectors for all time we can use use the multistep scheme used by Tornberg and Gustavsson [48] at no extra expense over a single-step scheme. The integration of position is given as follows

$$\mathbf{x}_{i+1}^h = \frac{1}{3}\left[2\Delta t(2\dot{\mathbf{x}}_i^h - \dot{\mathbf{x}}_{i-1}^h) + 4\mathbf{x}_i^h - \mathbf{x}_{i-1}^h\right]. \tag{4.56}$$

We do similarly for θ_{i+1}, and then we can compute $\boldsymbol{\Theta}_{i+1}$ while $\mathbf{R}_{i+1}$ is known hence we have the new position in the lab frame $\mathbf{x}_{i+1}$ from (4.2), and the new tangent $\mathbf{t}_{i+1} = \boldsymbol{\Theta}_{i+1} \cdot \mathbf{X}_s(s - ct_{i+1})$.

4.5 Numerical validation

4.5.1 Convergence

We set the number of integration points to be twice the number of Legendre modes $N_{int} = 2N_l$ so that the Nyquist-Shannon theorem is satisfied. In general if

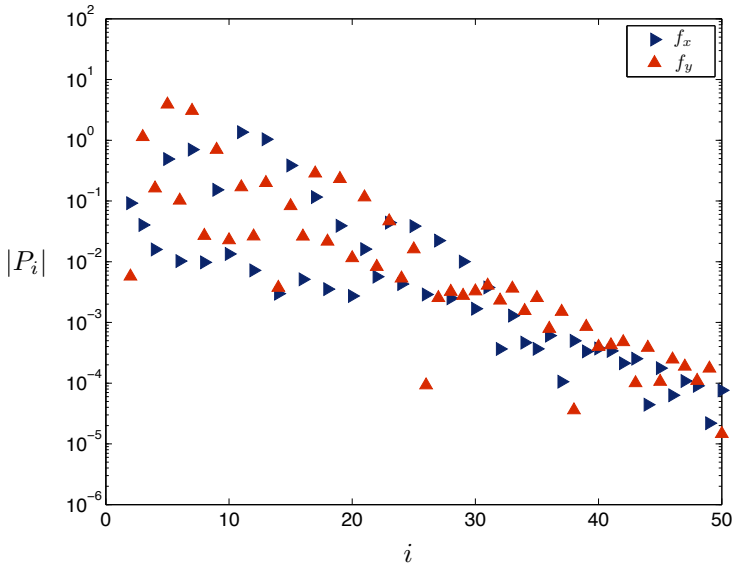

Figure 4.2: Figure illustrates the exponential decay of the Legendre polynomials when the swimmers are far apart.

the swimmers are not too close (say not within R^h for instance) then the Legendre modes decay exponentially and $N_l < 50$ is sufficient to ensure the highest modes are vanishing, say $|\mathbf{a}_{N_l}| < 10^{-4}$ as illustrated in Fig. 4.2. However, if the swimmers are near each other our asymptotic expansions may cease to be well ordered and the Legendre polynomial coefficients may not decay at all. In such a scenario we can no longer describe the interactions as our numerical method ceases to be accurate.

4.5.2 Comparison with theory

It's safe to say that there are no analytical models to which we can reasonably compare the full scope of the theory presented above. We can however take a single filament and provided we use a high wavenumber, the pitching due to the finite size can be suppressed so that we can use the approximation of a swimming filament which has a swimming speed that scales quadratically with amplitude much like the swimming sheet for comparison. Furthermore, we may compare the swimming speed of a filament with that computed using Stokesian Dynamics simulations in which the filament is composed of small spheres [49, 50].

A simple check that may be performed is to observe whether symmetries which restrict dynamics are observed in the numerical simulation. If an individual swimmer is instantaneously symmetric under a 180° rotation, then such a swimmer must have zero rotational velocity at that instant. Furthermore, for pairs of swimmers, if the system possesses instantaneous 180° rotational symmetry there can be no phase dynamics, nor can the swimmers undergo relative rotations, or collective rotations. In all these examples our numerical simulations conform to expectation.

4.6 Results

When the swimmers are of finite size they will experience rotation. Furthermore hydrodynamic interaction will cause attraction or repulsion between the swimmers. This added dynamical complexity can make it significantly more difficult to tease out the relevant nature of the interactions and therefore, to gain a foothold we first look at a simple case where swimmers can only translate horizontally before exploring the more complex effects of rotation and attraction/repulsion.

4.6.1 Swimmers on a rail

In order to discern whether a sinusoidal swimmer, simply by being finite in nature ,will present sufficient asymmetry to observe synchronization, we first look at an idealization in which the swimmers were only permitted to translate relative to one another (mimicking the two dimensional problem), while attraction and rotation were eliminated, as if the swimmers were confined to a rail. This significantly simplifies the dynamical scenario while addressing the question of whether or not the flow fields generated by finite swimmers do indeed have a synchronizing component that would be lost if those swimmers were periodic.

The expectation was initially that finite sinusoidal swimmers without a head would have very weak interaction and might not synchronize, while the introduction of a head would produce highly asymmetric flow fields yielding strong

interactions and synchronization (or faster synchronization). What we find is that sinusoidal swimmers, both those with heads and those without, synchronize to an in-phase configuration. This means that the finite-size symmetry-breaking effect does indeed produce a flow field which drives the swimmers together, but unlike the infinite case, where the asymmetry had to be prescribed to the waveforms, here for these swimmers propagating symmetric sinusoidal waves, there is no condition under which the swimmers synchronize to an opposite phase conformation. The surprising result is that the swimmers without heads synchronize on a faster time scale as illustrated in Fig. 4.3. What we see is that the headless swimmers synchronize on a timescale that is here a factor of four faster than the swimmers with heads. We note that we maintain identical kinematics for both swimmers. The headless swimmers move as if they had a head but the pertinent hydrodynamics are simply eliminated.

A reasonable explanation of this phenomenon could be that while the heads produce a more asymmetric flow there is an increased hydrodynamic drag preventing horizontal translation. Yet this explanation is contradicted by the fact that the headless swimmers travel only about one percent further than swimmers with heads which indicates that perhaps there is something deeper at play. We point out that the hydrodynamic interaction due to the heads seems to drive a large oscillatory component in the relative position of the two swimmers with a timescale of the gait itself, oscillations which are much larger than those present in the dynamics of the headless swimmers. So it appears that the asymmetric flow fields produced by the heads do indeed drive larger phase dynamics but that relative motion is oscillatory and does not enhance, but rather hinders, a coherent evolution of the phase to a synchronized state.

Offset synchronization

When the swimmers are finite, there is the possibility that the swimmers could become phase-locked with a phase difference which is an integer multiple of 2π. We refer to this as offset synchronization because the position of the heads is offset. In our simulations we do not observe offset synchronization and there does

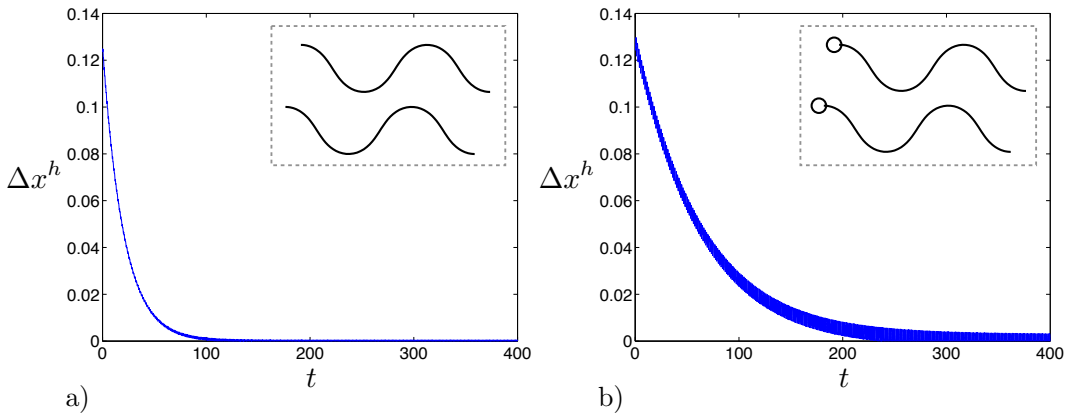

Figure 4.3: a) Shows the synchronization of headless sinusoidal swimmers, while b) shows swimmers with heads. In both cases the swimmers are only permitted to translate horizontally. We see that the time required for synchronization with heads is longer than without. The insets contain illustrations of each pair of swimmers, here $n = 1.5$ and $\Delta\mathbf{x}^h(t = 0) = \{1/8, 1/4\}$ apart while $R_h = 0.04$ and $\epsilon = 0.01$.

not appear to be a true fixed point for these configurations. We find that the phase evolution is slower but non-zero near points where the swimmers are in phase but offset.

4.6.2 Long range dynamics

Swimmers with heads

When rotations and attraction/repulsion are introduced the dynamics of the two-body interactions is much more complicated. It is hence insightful first to consider what we might expect from the leading order far field interactions. A flagellated swimmer with a head is a dipole to leading order in the far field. Each swimmer is force free and so the leading order term in an expansion of the boundary integral equations must necessarily be free of the Stokeslet term which integrates to give the net force on the body. The next term is a dipole, and here the dipole is apparent as the swimmer has a head with large drag which pushes fluid out of the way and the drag on the head is balanced by the thrust of the flagellum. In the far field this is seen as a dipole oriented in the direction of the velocity vector with a positive sign indicating the swimmer is *pushing* flow outwards (known as a

pusher).

The dynamics of dipole-dipole interactions as a model for swimming microorganisms was first studied by Guell *et al.* [51]. It was shown that for two pushers, each swimmer will be reoriented by the flow field generated by its neighbor so as to align their velocity vectors. This reorientation occurs on a time scale set by the separation $\dot{\Delta\theta} \sim UL(R^h)^2/h^3\Delta\theta$ where U is the (dimensional) swimming speed of the microorganisms and h the distance between them. This is clearly beneficial for synchronization as if the swimmers are slightly misaligned their flow fields will act to align the swimmers so that they don't swim away from each other, preventing any synchronizing dynamics from taking place. Additionally, the flow fields act to attract the swimmers with a speed $U_{attract} \sim ULR^h/h^2$. This attraction then reduces the separation which in turn accelerates both the attraction and the reorientation.

Our model contains a much more detailed account of the hydrodynamic interactions between two pushers but on the surface we find the dipole-dipole model to give a very good account of the interactions when the swimmers are not unreasonably close together.

Our simulations find, in accordance with the simple dipole model, that if the swimmers start with an initial angle separating their velocity vectors hydrodynamic interactions will realign the swimmers. The space of stable angles depends on the the size of the head, the length of the flagellum, the separation between the swimmers and the swimming speed (and hence the wave speed and amplitude). We leave the cataloguing of this parameter space to a subsequent paper.

We also find the swimmers attract one another as predicted by the simple dipole-dipole model as shown in Fig. 4.4. Indeed given the simple scaling of the dipole model one would expect the swimmers to attract each other initially with a speed an order of magnitude slower than the speed of the swimmer in this instance and this is indeed precisely what we find. Of course in that approximation the rate of attraction is divergent as the swimmers get close, and in our simulations the rate of attraction does not grow unbounded (it increases roughly linearly in time see Fig. 4.4c). This rate of attraction is however between one and two orders

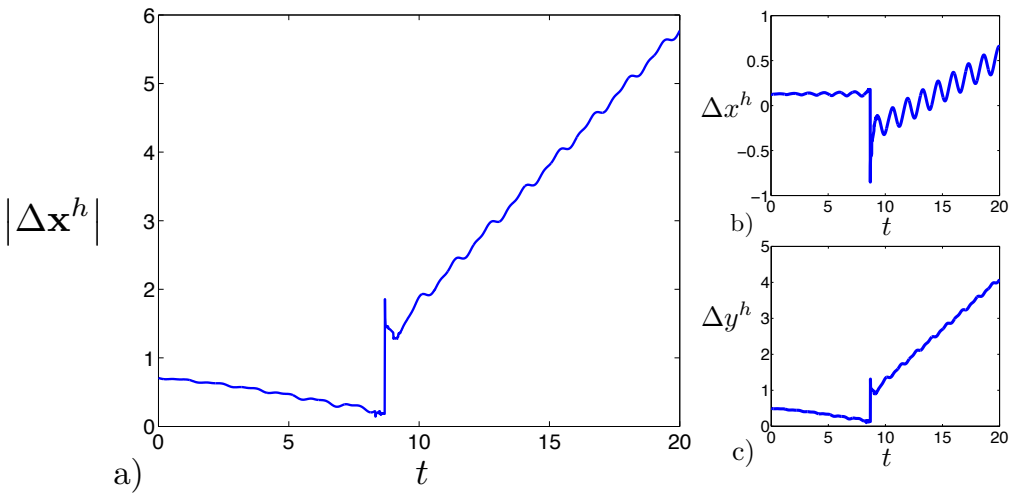

Figure 4.4: This figure illustrates that the dipole-dipole attraction of the two swimming microorganisms occurs on a much faster time-scale than the synchronization observed in the previous section. Here a) shows distance between the heads and b) and c) show the x and y components respectively. We see a numerical collision event prior to ten periods as the organisms approach and the singular interaction causes a discontinuity in their relative position. Here again $n = 1.5$ and $\Delta \mathbf{x}^h(t = 0) = \{1/8, 1/2\}$ while $R_h = 0.04$ and $\epsilon = 0.01$.

of magnitude faster than the rate of synchronization we observed in simulations above in Fig. 4.3b). This is problematic in our simulation as the model is only valid when the distance between the swimmers is large. In Fig. 4.4 we see that the swimmers quickly close the distance between them and as a result we have a numerical 'collision' event prior to ten periods elapsing as we attempt to integrate diverging integrals. Here the simulation is completely inaccurate and we see a discontinuity in the velocity.

We see that attraction occurs on much faster time scales than synchronization for finite swimmers with heads. In this scenario far field approximations break down as the organisms get close before synchronization occurs. To accurately model the full synchronization dynamics for finite swimmers it would be necessary to include the physics of lubrication interactions and possibly steric interactions. The Stokesian Dynamics method [49], initially developed for numerical simulation of colloidal suspensions, was recently adapted to model swimming problems [50]. This method, which models swimmers as a collection of spherical particles

and includes both far field dynamics by the method of reflections and near field interactions with lubrication theory, may be robust enough to model the entire synchronization event.

We point out that here and in the previous chapter we modeled the swimmers by prescribing their kinematics, and while this may be a reasonable approach in the far field, as the swimmers approach each other the hydrodynamic interactions between the swimmers become much stronger, the pressure diverges with the square of the separation and it becomes unrealistic to assume that the flagella of the swimmers will not be significantly deformed by the flows. In light of this in the next chapter we will proceed to model the swimmers as elastic sheets in the lubrication limit and will find that elastic deformations present a significant avenue for symmetry breaking and synchronization.

Headless swimmers

The heads of spermatozoa carry the genetic payload and so it is perhaps unphysical to consider the behavior of headless swimmers. Nevertheless, it is an interesting scenario because swimmers without heads do not possess a very clear dipole which arises from the drag of a large head balancing the thrust of the flagella. The configuration is much more uniform and hence we expect the far-field dipole model to be much less representative. In Fig. 4.5 illustrate the interactions between two headless microorganisms.

The results are somewhat surprising. Initially we see that the organisms begin to synchronize and are attracted together, on a somewhat slower time scale than for the swimmers with heads. But as they approach each other they are reoriented by the flow and consequently swim apart and move back out of phase. The accuracy of the interaction when the organisms approach can be regarded as questionable as near-field effects will certainly play a role, but given the perfect periodicity of the interactions it is perhaps reasonable to assume the far-field effects are being captured accurately.

An interesting question to address is how accurately does a dipole-dipole model capture these interactions both for swimmers with heads and without, a

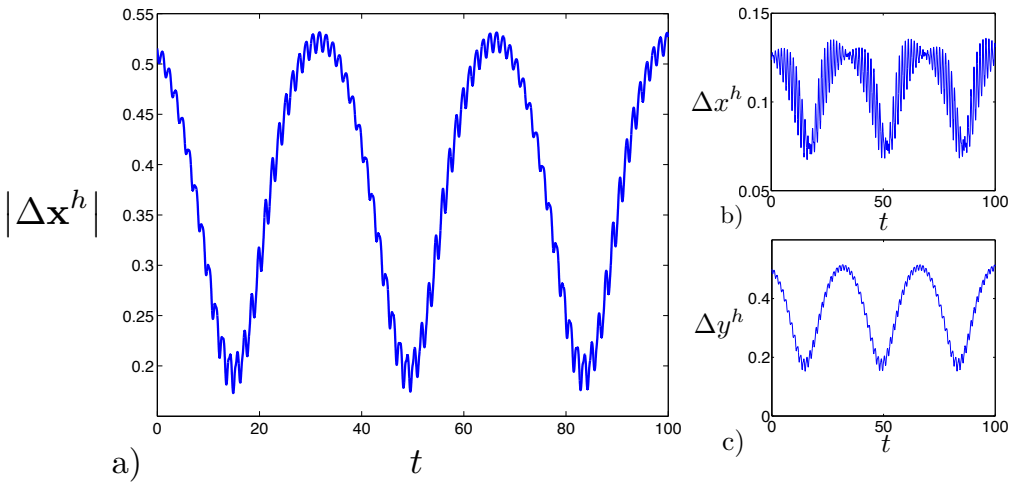

Figure 4.5: This figure illustrates that the periodic attraction of the two swimming headless microorganisms. Here a) shows distance between the 'head' and b) and c) show the x and y components respectively. We see that the microorganisms start to synchronize and come together but upon reaching a threshold there is a reorientation and the organisms start swimming apart and this occurs on periodically. Here again $n = 1.5$ and $\Delta \mathbf{x}^h(t = 0) = \{1/8, 1/2\}$ while $R_h = 0.04$ and $\epsilon = 0.01$.

goal of future work.

4.7 Conclusion

In this chapter we observed that symmetry breaking due to the finite size of real microorganims is a mechanism by which these swimmers may become synchronized and that surprisingly, swimmers without heads synchronized faster when confined to a rail than those with heads. We observed that for swimmers with heads, the full far-field dynamics of their interactions seem well represented by long range dipole-dipole fields. We saw that those hydrodynamic interactions serve to align swimmers so that they are parallel and attract the swimmers together. This attraction occurs on a faster time scale than synchronization. This leads to a break-down of numerical methods which rely on far field expansions but also prompts the exploration of elastic effects which may become important as the organisms are attracted together.

Chapter 5

Elastic effects

5.1 Introduction

In this chapter we investigate a physical mechanism responsible for symmetry-breaking in real biological cells. Instead of delineating a fixed waveform for the swimming sheets, we take the more realistic modeling approach of passing internal waves of bending as produced by a flagellum's internal structure (or axoneme) [52]. In the case of a single sheet, similar models have been employed to study swimming [53, 54] and peeling [55]. We use this model to show that elastic deformation due to fluid body interactions, with purely sinusoidal forcing, always leads to in-phase synchronization.

Flexibility has long been considered as an avenue for symmetry breaking in Stokes flow. Purcell, in his celebrated talk and paper [56], asserted that while a stiff oar undergoing reciprocal motion would produce no net motion, due to the scallop theorem, a flexible oar would escape this conundrum because of a broken symmetry between forward and reverse strokes. This was first investigated analytically by Machin [57] while more recently a number of theoretical and experimental studies have further elucidated the effect of flexibility quantitively, both for boundary-driven [58, 42, 59] and internally-driven filaments [60, 61, 62].

Recently, the analysis of a pair rotating helices as model for bacterial flagella has shown flexibility to be a crucial ingredient for synchronization [63], as was similarly shown for a minimal model of interacting cilia [64]. Additionally flexibil-

ity has been found to be requisite for the synchronization of paddles that would otherwise be too symmetric to yield stable fixed points [65]. In these models and experiments, the bodies are rigid, but permitted to deviate from their trajectories, in an elastic manner in response to fluid forces. In contrast, here we allow the bodies themselves to deform due to fluid stresses induced by the other swimmer.

Our approach is organized as follows. For a pair of two-dimensional sheets in the lubrication limit, we derive a system of nonlinear equations governing both the fluid stresses and the resulting swimmer shapes. We linearize these equations to produce analytical solutions, and then solve the nonlinear equations numerically. We show that flexible sheets with symmetric sinusoidal forcing will deform when interacting with each other via a thin fluid layer in such a way as to break geometrical symmetry, and to evolve to an in-phase conformation where energy dissipation is minimized. Further, this evolution of phase is shown to be functionally equivalent to that found for prescribed waveforms in viscoelastic fluids [29], illuminating the role of elasticity in symmetry-breaking and synchronization.

5.2 Model system

We consider the dynamics of two infinite two-dimensional elastic sheets which are separated by a fluid layer of mean distance $\bar{h}$ (see Fig. 7.1). The sheets deform due to a balance between an active moment m, passive bending (elastic) resistance, and fluid stresses. The positions of the sheets are given by $y_1 = \eta_1(x,t)$ for the bottom sheet and $y_2 = \bar{h} + \eta_2(x,t)$ for the top sheet. We seek to solve this problem in the limit that the fluid layer is thin compared to the wavelength of the sheets, $k\bar{h} \ll 1$, to make use of Reynolds' lubrication approximation for the fluid field equations [66].

An infinitesimal element along one sheet is subject to tension, T, normal force, N and moment, M (shown in Fig. 7.1). Since the fluid layer is thin and lubrication forces are singular with the gap thickness, forces from the outer flow are safely ignored [54]. To capture the active bending of the sheet we use a model for the flagella of eukaryotes introduced by Jülicher and co-workers [61, 52] where

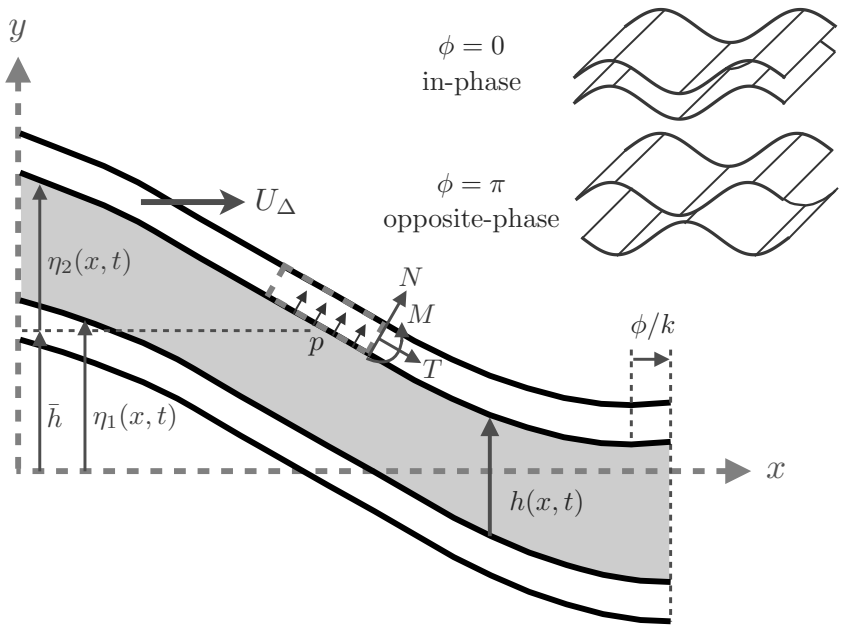

Figure 5.1: System of two infinite two-dimensional sheets, of shape described by the functions η_1 and η_2, which are separated by a fluid layer of thickness h (mean value, $\bar{h}$), have a relative phase ϕ, and may move relative to each other with a velocity U_Δ. An infinitesimal material element on the top sheet is subject to fluid pressure p, normal force N, tension T and moment M. Inset: schematic representation of in-phase and opposite-phase configurations.

the bending of an elastic filament (flagellum) is caused by the constrained sliding of microtubule doublets; the effect of the internal forces which induce sliding are here represented by an active moment density m. Given that we are in an over-damped limit we take the equilibrium shapes to arise instantaneously [55]. Assuming reasonably small deflections such that the swimmers are linearly elastic [67], force ($\mathbf{F}$) and moment (M) balances on the top sheet yield, respectively,

$$\frac{\partial \mathbf{F}}{\partial x} = -\mathbf{n} \cdot \boldsymbol{\sigma}, \qquad \frac{\partial M}{\partial x} = -N + m, \tag{5.1}$$

where $\mathbf{n}$ is the unit normal and $\boldsymbol{\sigma}$ is the fluid stress tensor. The relation between the moment and the sheet curvature is given by the constitutive relation $M = B\partial^2\eta/\partial x^2$, where B is the sheet bending stiffness. Combining with (5.1) we obtain the equations governing the shape of the sheets

$$B\frac{\partial^4 \eta}{\partial x^4} = \frac{\partial m}{\partial x} \mp \mathbf{n} \cdot \boldsymbol{\sigma} \cdot \mathbf{n}, \tag{5.2}$$

where $\mp$ are for the top and bottom sheets respectively. If resistive force theory is used for the fluid forces then we obtain the governing equation used by [52] for a single filament.

The internal forcing on the sheets is assumed to take the form $m(x,t) = Ag(kx - kct)$ where k is the wavenumber, c is the wave speed, A is the amplitude of the moment and g is an arbitrary but 2π-periodic function. Because the forcing is periodic, we will assume the shape η also to be periodic. We nondimensionalize vertical distances by $y^* = y/\bar{h}$ and horizontal distances by $x^* = kx$ (* indicates a dimensionless quantity). Nondimensionalizing the continuity equation we find that if the horizontal velocity is given by $u = cu^*$ then the vertical velocity must be $v = \epsilon c v^*$ where $\epsilon = k\bar{h}$. The Stokes equations then yield the lubrication equations to leading order in ϵ

$$\frac{\partial p^*}{\partial x^*} = \frac{\partial^2 u^*}{\partial y^{*2}}, \qquad \frac{\partial p^*}{\partial y^*} = 0, \tag{5.3}$$

$$\frac{\partial u^*}{\partial x^*} + \frac{\partial v^*}{\partial y^*} = 0. \tag{5.4}$$

where $p^* = \epsilon^2 p/\mu\omega$. Forces (per unit depth) are nondimensionalized as $f^* = f\epsilon/\mu c$, while energy dissipation rate per unit depth is $\dot{E}^* = \epsilon^2 \dot{E}/\mu\omega c\bar{h}$.

In the lubrication limit, $\epsilon \ll 1$, the normal force due to the fluid on the beam is to leading order merely the pressure, $-\mathbf{n}\cdot\boldsymbol{\sigma}\cdot\mathbf{n} = p$. Since the field equations for the fluid yield the pressure gradient, we differentiate (5.2), and recasting the equation in dimensionless form we obtain

$$B^* \frac{\partial^5 \eta^*}{\partial x^{*5}} = A^* \frac{\partial^2 g}{\partial x^{*2}} \pm \frac{dp^*}{dx^*}, \tag{5.5}$$

where $B^* = B\epsilon^3 k^3/\mu\omega$ is the dimensionless bending stiffness and $A^* = A\epsilon^2 k^2/\mu\omega$ is the dimensionless amplitude of the active bending moment. This equation allows us to solve for the shape of the sheets, $\eta_{1,2}$, and is coupled to the fluid field equations through the pressure gradient. We now drop the * for convenience.

5.3 Analysis

Given the form of the forcing we expect post-transient solutions which are functions of a wave variable $z = x - t$ and thus we write $\eta = \eta(z)$. The top

sheet may move relative to the bottom sheet with a horizontal velocity $u = U_\Delta$, hence the boundary conditions for the fluid equations (5.4), in a frame moving with waveform are given by $u(x, y_1) = -1$, $v(x, y_1) = -\eta_1'$, $u(x, y_2) = U_\Delta - 1$ and $v(x, y_2) = -\eta_2'$. Given the above boundary conditions the solution for the velocity field is found to be

$$u(x, y) = \frac{1}{2}\frac{dp}{dx}(y - y_1)(y - y_2) + U_\Delta \frac{y - y_1}{y_2 - y_1} - 1. \tag{5.6}$$

If one integrates the continuity equation one finds

$$\frac{\partial}{\partial x}\int_{y_1}^{y_2} u dy = U_\Delta \frac{d\eta_2}{dx}. \tag{5.7}$$

If $U_\Delta = 0$ then the flow rate between the sheets is constant. Integrating (5.7) and exploiting the periodicity of the pressure [25], we obtain the equation for the pressure gradient

$$\frac{dp}{dx} = \frac{6U_\Delta - 12}{h^2} - \frac{12U_\Delta y_2}{h^3} - \frac{(6U_\Delta - 12)I_2 - 12U_\Delta J_3}{I_3 h^3}, \tag{5.8}$$

where the distance between the two sheets is given $h = 1 + \eta_2 - \eta_1$ and $I_j = \int_0^{2\pi} h^{-j} dx$ and $J_3 = \int_0^{2\pi} y_2 h^{-3} dx$. Then the force on the top sheet is given by

$$F_x = \int_0^{2\pi} \left(y_2 \frac{dp}{dx} - \frac{\partial u}{\partial y} \right)\Big|_{y=y_2} dx = \int_0^{2\pi} \left(\frac{1}{2}\frac{dp}{dx}(\eta_2 + \eta_1) - \frac{U_\Delta}{1 + \eta_2 - \eta_1} \right) dx. \tag{5.9}$$

5.3.1 Linear regime: statics

We first look at the case where we enforce $U_\Delta = 0$ (i.e. we fix the top sheet with respect to the bottom sheet) in order to determine under which condition a nonzero synchronization force will arise.

If we assume the dimensionless amplitude of the forcing A to be small, and the dimensionless bending stiffness B to be large, then the shape amplitude (or maximum value of the shape) $\|\eta\|_\infty$ is expected also to be small. Linearizing the pressure gradient for small η, with $U_\Delta = 0$ gives

$$\frac{dp}{dx} \approx -12(\eta_2 - \eta_1), \tag{5.10}$$

where we have invoked an integrated conservation of mass, $\langle \eta_2 - \eta_1 \rangle = 0$ (angle brackets $\langle\rangle$, denote the average over a period). Our goal is now to determine

whether two sheets which are equally and symmetrically forced but with a phase shift ϕ will synchronize in time. With this in mind we let $g_2 = g_1(z+\phi)$ with $g_1(z) = \cos(z)$, and we set equal for both sheets the bending stiffness B and the forcing amplitude A. The linearized governing equations are then given by

$$\begin{aligned} B\frac{d^5\eta_1}{dz^5} - 12(\eta_2 - \eta_1) &= -A\cos(z), \\ B\frac{d^5\eta_2}{dz^5} + 12(\eta_2 - \eta_1) &= -A\cos(z+\phi). \end{aligned} \tag{5.11}$$

To solve these equations we apply periodic boundary conditions. The solution of this system of equations with the linearized pressure gradient (5.10), can be found analytically to be

$$\begin{aligned} \eta_1(z) &= A\frac{12B\big[\cos(z+\phi) - \cos z\big] - \big[(288+B^2)\sin z + 288\sin(z+\phi)\big]}{B\,(576+B^2)} + C, \\ \eta_2(z) &= A\frac{12B\left[\cos z - \cos(z+\phi)\right] - \left[288\sin z + (288+B^2)\sin(z+\phi)\right]}{B\,(576+B^2)} + C. \end{aligned} \tag{5.12}$$

Note that nothing prevents the solution from including a uniform shift $C(A,B)$; however, the relevant physics of the problem are invariant under such a shift hence and hence the value of C is irrelevant (equivalently, we place our z-axis at $\langle\eta_1\rangle = 0$).

Both shapes in (5.12) are delineated by the competition between bending rigidity, the pressure gradient in the fluid, and the internal forcing (with ϕ dependence). In this linear limit we note that the sheets are linear in the forcing amplitude A, and when $A = 0$ then as expected they become straight, *i.e.* $\eta = 0$. In the limit where rigidity dominates, $B \to \infty$, then the sheets also tend to become straight, $\eta \to 0$. If the rigidity and forcing amplitude are both very large ($A, B \gg 1$) then we can scale out the contribution from the fluid forces in (5.11) and we are left with $\eta_1 \approx -(A/B)\sin z$ and $\eta_2 \approx -(A/B)\sin(z+\phi)$ as might be expected. Note finally that the solutions in (5.12) are only valid when $B \gg A$ as otherwise unphysical solutions may arise with the sheets overlapping; this is prevented when the full nonlinear form of the pressure gradient is kept, as it diverges when $h \to 0$.

Solutions to (5.12) for $A = 1$, $B = 10$, and three values of the phase difference ($\phi = \pi/4, \pi/2, 3\pi/4$) are plotted in Fig. 5.2 (left). We observe that the

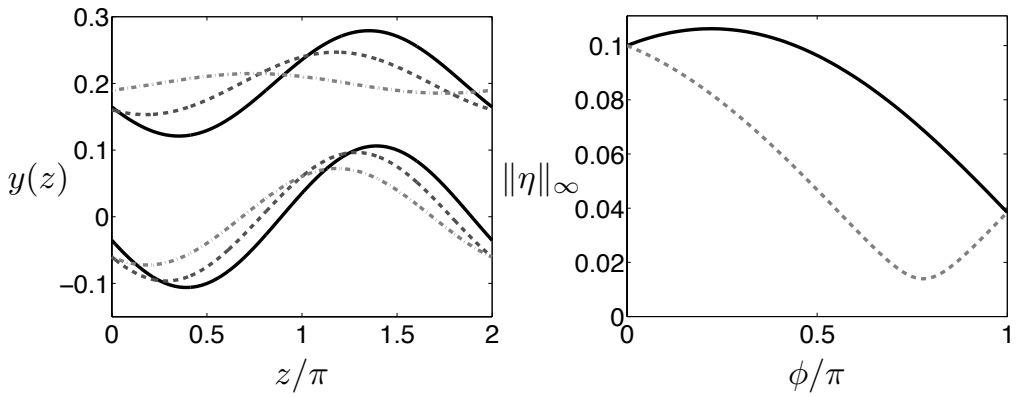

Figure 5.2: Left: Solution shapes, (5.12), for various phase differences $\phi = \pi/4$ (solid lines), $\pi/2$ (dashed lines), and $3\pi/4$ (dash-dot lines), with $A = 1$ and $B = 10$. We observe that the amplitude is not evenly affected by the pressure (the plot is shown here with $\bar{h} = 0.2$ rather than $\bar{h} = 1$ for display purposes only). Right: Shape amplitude, $\|\eta\|_\infty$, vs. phase difference, ϕ (bottom sheet: solid line; top sheet: dashed line). Lines are reversed upon the change $\phi \to -\phi$.

shapes are sinusoidal and hence individually remain symmetric both about the vertical axis and the horizontal axis. The global asymmetry that arises however is that the amplitudes of the two waveforms are not equally modulated by the fluid pressure, as shown in Fig. 5.2 (right). We see indeed that the top sheet has smaller amplitude for positive ϕ (and by symmetry, this is reversed upon changing $\phi \to -\phi$).

The phase locking force on the top sheet is, at leading order, given by

$$F_x = -6 \int_0^{2\pi} (\eta_2 - \eta_1)(\eta_2 + \eta_1) dx = 2\pi\alpha \sin\phi. \tag{5.13}$$

where $\alpha = 144A^2/(576B + B^3)$. Equation (5.13) is the main result of this chapter. The phase locking force is proportional to the sine of the phase, meaning that the only stable fixed point is expected to occur at $\phi = 0$, and hence all initial conformations will evolve to the stable in-phase conformation. We thus see that the elasticity of the swimmers, and thus fluid-structure interactions, can introduce the geometrical symmetry-breaking necessary to develop a nonzero phase locking force. The force is found to be quadratic in amplitude, reminiscent of viscoelastic symmetry-breaking [29] (and discussed here in Chapter 7); by comparison, the phase-locking force arises at fourth order in amplitude for prescribed asymmetric

waveforms in a Newtonian fluid. The reason for the difference is that with elastic deformation, the sheets are ultimately not the same shape, despite having identical mechanical properties, and hence $\langle \eta_1^2 \rangle \neq \langle \eta_2^2 \rangle$; for prescribed waveforms this is different as the same waveform is prescribed for both sheets, and the quadratic term of the force vanishes.

The energy dissipated by the fluid between the two swimming cells to leading order is

$$\dot{E} = 12 \int_0^{2\pi} (\eta_2 - \eta_1)^2 \, dx = \frac{24\pi A^2}{576 + B^2}(1 - \cos\phi). \tag{5.14}$$

We see that the energy dissipation is a global minimum when $\phi = 0$ and global maximum when $\phi = \pi$. It follows then that the cells will always evolve to a state of minimum energy dissipation. We observe that the form of the energy dissipation is precisely the same as that for fixed shapes (and taking the fixed wave amplitude $A_{fixed}^2 = A^2/(576 + B^2)$ they are equal) [68]. It is important to note that waveforms with a prescribed broken symmetry may evolve to either the in-phase or opposite-phase conformation [25]; in contrast, the natural symmetry-breaking due to elasticity of the bodies, or in the fluid, leads to a conformation of minimum energy dissipation.

5.3.2 Linear regime: dynamics

When the sheets are permitted to evolve in time in force-free swimming, the relative velocity U_Δ will thus be nonzero. In order to determine the leading order component of the pressure field we must first find out how the relative velocity scales with the sheet amplitudes. Given that the net force on the sheets in the dynamic case must now be zero, we obtain at leading order the relative speed as given by

$$U_\Delta = -\frac{3}{\pi} \int_0^{2\pi} (\eta_2 - \eta_1)(\eta_2 + \eta_1) dx. \tag{5.15}$$

We see that the velocity is quadratic in amplitude and indeed is proportional to the static force $U_\Delta = F_x^s/2\pi$ (we use here the superscript s to indicate the static force given by (5.13) to avoid confusion). With this we thus know that at leading

order the pressure field (for a given ϕ) is invariant between the static and dynamic case, and since the beam equation couples via the pressure field, our instantaneous shapes are found to be the same. The only difference is that now the phase difference changes in time (geometrically) due to the presence of a nonzero relative velocity, according to $\mathrm{d}\phi/\mathrm{d}t = -U_\Delta$. Using (5.15), we find the rate of change of the phase at leading order to be given by

$$\frac{d\phi}{dt} = -\alpha \sin\phi. \tag{5.16}$$

Equation (5.16) can be integrated analytically, leading to a time-evolution of the phase given by

$$\phi(t) = 2\tan^{-1}\left[\tan\left(\frac{\phi_0}{2}\right)e^{-\alpha t}\right]. \tag{5.17}$$

All initial conformations, ϕ_0, decay in time to the stable in-phase conformation, $\phi = 0$. Notably, the time-evolution of the phase for a sinusoidally forced elastic sheet we obtain here is mathematically similar to that for a fixed sinusoidal waveform in a viscoelastic fluid [29] and for rigid bodies with flexible trajectories [64], emphasizing therefore the crucial role of elasticity in synchronization.

Finally, if we allow a small difference in the wavespeeds of the sheets, $\Delta\omega$, then to leading order we have the same evolution of phase, (5.16) and (5.17), but now the rate of change of phase is defined as $\dot{\phi} = -U_\Delta - \Delta\omega$ and hence we see a synchronization of shape but not of material points.

5.3.3 Nonlinear case

To move beyond the linear regime, we now solve the nonlinear equations for the shapes (5.5) numerically, together with (5.8), using Matlab's boundary value problem solver `bvp4c`, both for the static case, $U_\Delta = 0$, and the force free case, $F_x = 0$ using (5.9).

We find the linearized pressure gradient to be a capable approximation, particularly when the bending is of the same order as the pressure $B \sim 1$ and the phase difference is small; however, when $A, B \gg 1$ the linearized pressure may lead to unphysical solutions particularly if the sheets are near opposite-phase as

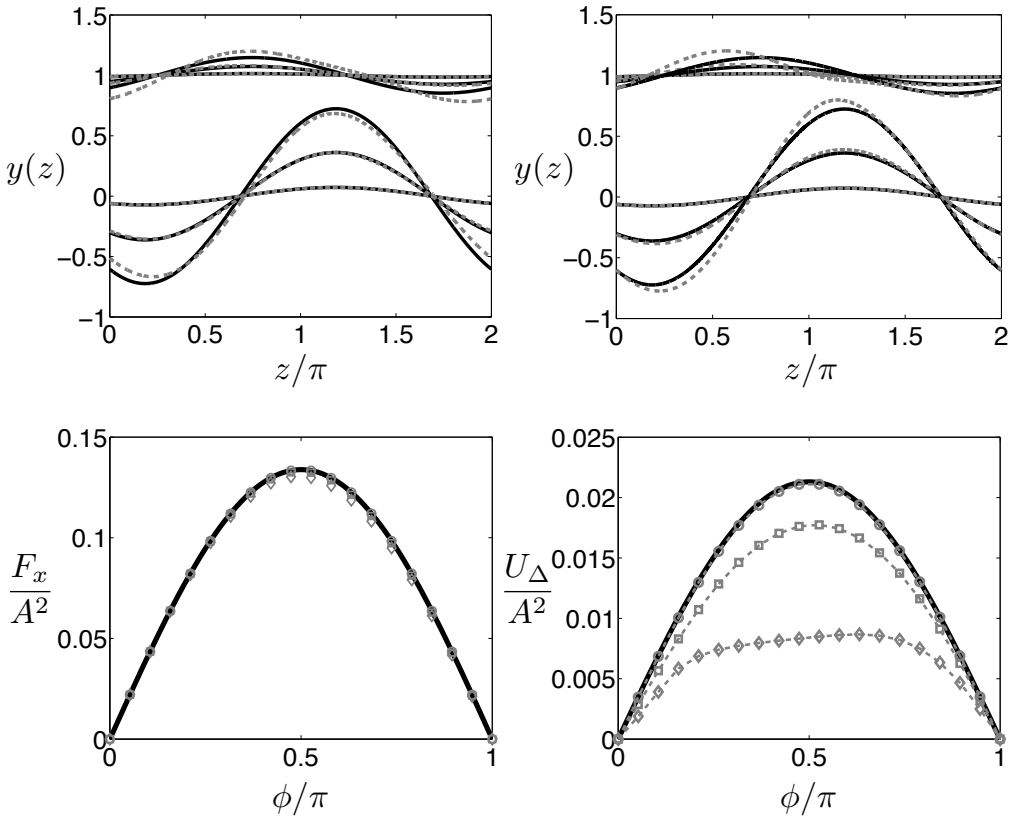

Figure 5.3: Top: solution shapes, η_1 and η_2, for bending stiffness $B = 10$, phase difference $\phi = 3\pi/4$, and amplitudes $A = \{1, 5, 10\}$ (left: $U_\Delta = 0$; right $F_x = 0$); linearized pressure approximation: solid lines; full pressure gradient: dashed lines. Bottom left: phase locking force, F_x/A^2, vs. phase difference, ϕ, when $U_\Delta = 0$; bottom right: relative velocity, U_Δ/A^2, vs. ϕ, when $F_x = 0$. Both plots are for numerical solutions of the nonlinear equations with $B = 10$ and $A = 1$ (circles), 5 (squares), and 10 (diamonds); linearized solutions are shown as solid lines. Away from the linear regime, the rate of change of the phase is affected while the forces are not.

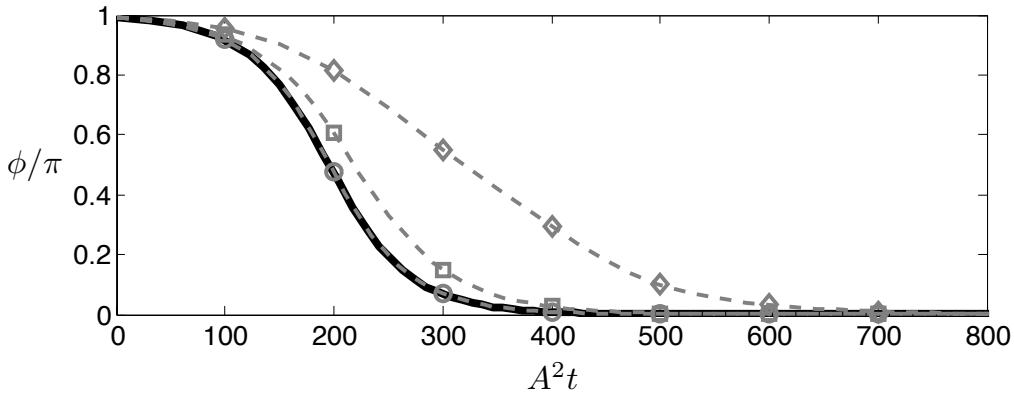

Figure 5.4: Time-evolution of the phase difference, ϕ, in the nonlinear problem for $B = 10$ starting from an initial angle of $\phi/\pi = .99$ and with forcing amplitude $A = 1$ (circles), 5 (squares) and 10 (diamonds); the linear estimate is solid. As the forcing amplitude increases, the linear solution increasingly underestimates the time scale to synchronize.

the divergent nature of the full form of the pressure gradient is required to deform the sheets from contact.

In Fig. 5.3 we illustrate the breakdown of the linear regime. We plot the static shapes ($U_\Delta = 0$, top left), and dynamic shapes ($F_x = 0$, top right), both with a phase difference of $\phi = 3\pi/4$, bending stiffness $B = 10$, and with forcing amplitudes $A = \{1, 5, 10\}$. We see that for increasing amplitude the shapes predicted by linearized equations (solid) and nonlinear equations (dashed) begin to diverge. In particular the nonlinear equations lead to a pronounced left-right asymmetry in the individual shape. In the lower left plot of Fig. 5.3 we display the phase locking force vs. phase, while in the lower right plot we show the relative velocity vs. phase, both with $B = 10$ and $A = \{1, 5, 10\}$ (circles, squares and diamonds respectively) for the numerical solutions to the nonlinear equations; the analytical solutions for the linear equations are shown solid. The synchronizing hydrodynamic force, F_x, found by either method remains remarkably consistent even for very large forcing amplitude, A. In contrast, the rate of change of the phase decreases markedly from the linear approximation for large amplitude waves. Because the force is virtually unaffected we know therefore that the resistance to motion is dramatically increased by the change in shape.

In Fig. 5.4 we integrate the instantaneous relative velocity to obtain the

evolution of the phase in time. We show solution to both the linear equations (solid) and nonlinear equations (dashed) for $B = 10$ and $A = \{1, 5, 10\}$ starting from an initial phase difference of just less than π. We see that, as the forcing amplitude increases, the nonlinear equations yield an increasingly slower evolution to a synchronized conformation than that predicted by the linear regime; however, the general behavior remains qualitatively unchanged.

5.4 Conclusion

In this chapter we inquired about a physical mechanism responsible for symmetry-breaking and synchronization in the flagella of biological cells such as spermatozoa. In a Newtonian fluid, two swimming sheets passing waveforms of a prescribed sinusoidal shape will not synchronize due to an excess of symmetry; however, here we have demonstrated that identical flexible sheets with symmetric sinusoidal forcing will deform, when interacting with each other via a thin fluid layer, in such a way as to systematically break the overall geometrical symmetry. This system will always evolve to an in-phase conformation in which energy dissipation is minimized, in contrast to a prescribed asymmetry, which may maximize energy dissipation. In addition, this time-evolution of the relative phase is shown to be equivalent to that obtained for prescribed waveforms in viscoelastic fluids in Chapter 7, emphasizing the crucial role of elasticity in symmetry-breaking and synchronization – be it that of the fluid, or the swimmers themselves.

Chapter 5, in part, is a reprint of the material as it appears in the Journal of Fluid Mechanics 2011. Elfring, Gwynn J.; Lauga, Eric, Cambridge University Press, 2011. The dissertation author was the primary investigator and author of this paper.

Chapter 6

Non-Newtonian swimming

In the previous chapters our swimming microorganisms, representing in particular spermatozoa, were immersed in Newtonian fluids. However, many biological fluids involved in mammalian reproduction are non-Newtonian. As these spermatozoa make their journey through the female reproductive tract they encounter several complex fluids, including glycoprotein-based cervical mucus in the cervix, mucosal epithelium inside the fallopian tubes, and actin-based viscoelastic gel outside the ovum [69, 70]. In a viscoelastic fluid, kinematic reversibility, restated in Purcell's scallop theorem [56], breaks down due to the presence of normal stresses and shear-dependent material functions, fundamentally altering the governing flow physics [10]. The waveform, structure, and swimming path of spermatozoa have been experimentally observed to be modified in viscoelastic fluids [71]. Locomotion in complex fluids has been studied analytically [72, 73, 74], and it has been shown that microorganisms which propel themselves by propagating waves along their flagella have a lower swimming speed in a viscoelastic fluid than in a Newtonian fluid [59, 75].

In this chapter we briefly introduce swimming in viscoelastic fluids and present some simple results which show how the presence of polymeric stresses can alter the dynamics of an organism.

6.1 Fundamentals

We consider here a viscoelastic fluid which is, as with everything in this thesis, forced by a very small relevant length scale which leads to a low Reynolds number, meaning that mechanical equilibrium is given by

$$\boldsymbol{\nabla} p = \boldsymbol{\nabla} \cdot \boldsymbol{\tau} \tag{6.1}$$

where p is the pressure and $\boldsymbol{\tau}$ is the deviatoric part of the stress tensor.

In a Newtonian fluid the constitutive relationship between stress and strain-rate was a simple linear one, $\boldsymbol{\tau} = \mu\dot{\boldsymbol{\gamma}}$ where $\dot{\boldsymbol{\gamma}} = \boldsymbol{\nabla}\mathbf{u} + \boldsymbol{\nabla}\mathbf{u}^{\mathrm{T}}$ is the strain-rate tensor. However, the biological viscoelastic fluids under consideration are polymeric suspensions and there are contributions to the stress both from the entropic polymers and the fluid in which they are suspended.

To relate the stress to the strain-rate, in this chapter and the next, we use the simplest polymeric constitutive equation derived from a microscopic theory, namely the Oldroyd-B model [76, 77]. In this model the stress is split into a contribution from the polymer and from the solvent, $\boldsymbol{\tau} = \boldsymbol{\tau}^p + \boldsymbol{\tau}^s$. The viscosity is similarly split $\mu = \mu^p + \mu^s$. The solvent is taken to be Newtonian $\boldsymbol{\tau}^s = \mu^s\dot{\boldsymbol{\gamma}}$ while the polymeric contribution to the stress is given by an upper-convected Maxwell model

$$\boldsymbol{\tau}^p + \lambda_1 \overset{\triangledown}{\boldsymbol{\tau}}^p = \mu^p\dot{\boldsymbol{\gamma}}, \tag{6.2}$$

where λ_1 is the relaxation time of the polymer. The upper convected derivative is defined for a general tensor $\mathbf{A}$ as $\overset{\triangledown}{\mathbf{A}} = \partial\mathbf{A}/\partial t + \mathbf{u}\cdot\boldsymbol{\nabla}\mathbf{A} - (\boldsymbol{\nabla}\mathbf{u}^{\mathrm{T}}\cdot\mathbf{A} + \mathbf{A}\cdot\boldsymbol{\nabla}\mathbf{u})$. Combining the above we can write the constitutive relation

$$\boldsymbol{\tau} + \lambda_1 \overset{\triangledown}{\boldsymbol{\tau}} = \mu\left[\dot{\boldsymbol{\gamma}} + \lambda_2 \overset{\triangledown}{\dot{\boldsymbol{\gamma}}}\right], \tag{6.3}$$

where $\lambda_2 = \lambda_1\mu_s/(\mu_s + \mu_p) = \lambda_1\beta$ is the retardation time of the polymer [77], and β is the ratio of the solvent viscosity to the total viscosity. Rheological studies have shown the relaxation time of cervical mucus to be between 1 and 10 seconds [78].

6.2 Boundary conditions

As in the previous chapters we model the swimming microorganism as a two dimensional swimming sheet. The shape of this sheet, in a frame moving with the sheet, can in general be represented by $y = \epsilon g(z)$ where

$$g(z) = \tilde{c}_n e^{inz}, \tag{6.4}$$

where $z = kx - \omega t$. It proves to be convenient in this chapter to use complex notation but of course $\Im[\tilde{c}_0] = 0$ and $\tilde{c}_{-n} = \tilde{c}_n^*$ so that the function is real. We use the following dimensionless variables $x^* = xk$, $t^* = t\omega$, $\mathbf{u}^* = \mathbf{u}/c$. We also define two Deborah numbers, $\mathrm{De}_1 = \lambda_1\omega$ and $\mathrm{De}_2 = \lambda_2\omega$. Given that the flagella of spermatozoa typically beat at a frequency between 20 and 50 Hz [9] we might expect a range of Deborah numbers $\mathrm{De}_1 = 10^2 - 10^3$, and in most practical instances $\mathrm{De}_1 \gg \mathrm{De}_2$ [77]. We now drop the $(^*)$ notation and refer only to dimensionless variables below.

6.3 Biharmonic solution

In this chapter, we will repeatedly refer to the general solution to the biharmonic equation $\nabla^4\psi(x,y) = 0$ which, when bounded at positive infinity, is given by the complex form

$$\psi(x,y) = \sum_{n=-\infty}^{\infty} (a_n + yb_n)e^{-|n|y}e^{inx}. \tag{6.5}$$

We will also in this section use a different symbol $\Psi(x,y,t)$ to refer the stream function whose time dependence may arise from the field equations (not necessarily merely a parametric dependence).

6.4 Expansion

As in previous chapters, we take the approach that the amplitude of transverse oscillations of the sheet, ϵ, is small and hence proceed to solve for all fields

perturbatively, e.g. $\dot{\boldsymbol{\gamma}} = \epsilon\dot{\boldsymbol{\gamma}}_1 + \epsilon^2\dot{\boldsymbol{\gamma}}_2 + ...$ The relationship between stress and strain at j^{th} order is hence given by

$$\left(1 + \mathrm{De}_1\frac{\partial}{\partial t}\right)\boldsymbol{\tau}_j - \left(1 + \mathrm{De}_2\frac{\partial}{\partial t}\right)\dot{\boldsymbol{\gamma}}_j = \sum_{m=1}^{j-1}\Big[\mathrm{De}_1\left(\boldsymbol{\nabla}\mathbf{u}_{j-m}^{\mathrm{T}}\cdot\boldsymbol{\tau}_m + \boldsymbol{\tau}_m\cdot\boldsymbol{\nabla}\mathbf{u}_{j-m} - \mathbf{u}_{j-m}\cdot\boldsymbol{\nabla}\boldsymbol{\tau}_m\right) - \mathrm{De}_2\left(\boldsymbol{\nabla}\mathbf{u}_{j-m}^{\mathrm{T}}\cdot\dot{\boldsymbol{\gamma}}_m + \dot{\boldsymbol{\gamma}}_m\cdot\boldsymbol{\nabla}\mathbf{u}_{j-m} - \mathbf{u}_{j-m}\cdot\boldsymbol{\nabla}\dot{\boldsymbol{\gamma}}_m\right)\Big]. \tag{6.6}$$

6.5 Transient response

Because the field equations in a viscoelastic fluid have an explicit time dependence, the flow resulting from the actuation of a boundary will now have a transient response to this actuation.

6.5.1 First order

The Oldroyd-B equation to first order is

$$\boldsymbol{\tau}_1 + \mathrm{De}_1\frac{\partial\boldsymbol{\tau}_1}{\partial t} = \dot{\boldsymbol{\gamma}}_1 + \mathrm{De}_2\frac{\partial\dot{\boldsymbol{\gamma}}_1}{\partial t}. \tag{6.7}$$

Taking the divergence and the curl we obtain

$$\left(1 + \mathrm{De}_2\frac{\partial}{\partial t}\right)\nabla^4\Psi_1 = 0, \tag{6.8}$$

and in the Laplace domain this yields

$$(1 + s\mathrm{De}_2)\nabla^4\bar{\Psi}_1 = \mathrm{De}_2\nabla^4\Psi_1(t = 0). \tag{6.9}$$

where the overbar represents a function in the Laplace domain. If we take the initial condition to be Newtonian then the right-hand side vanishes and we are left with a biharmonic equation for $\bar{\Psi}_1$.

The boundary conditions are

$$\boldsymbol{\nabla}\Psi_1^{(n)}\Big|_{y=0} = \boldsymbol{\nabla}g(z) = nic_n e^{niz}\mathbf{e}_x, \tag{6.10}$$

which in the Laplace domain yield

$$\boldsymbol{\nabla}\bar{\Psi}_1^{(n)}\Big|_{y=0} = \frac{nic_n}{in+s}e^{inx}\mathbf{e}_x. \tag{6.11}$$

From the general solution to the biharmonic equation we obtain

$$\boldsymbol{\nabla}\bar{\Psi}_1^{(n)}\Big|_{y=0} = \left[ina_n\mathbf{e}_x + (-|n|\,a_n + b_n)\mathbf{e}_y\right]e^{inx}. \tag{6.12}$$

Hence $a_n = c_n/(in+s)$ and $b_n = |n|\,a_n$ leaving

$$\Psi_1 = \sum_{n=-\infty}^{\infty} c_n(1+|n|\,y)e^{-|n|y}e^{inz}. \tag{6.13}$$

In the case of Taylor's sinusoidal swimming sheet we have $c_1 = -i/2$ and hence

$$\Psi_1 = -i(1+y)e^{-y}e^{iz} + c.c., \tag{6.14}$$

which is precisely the same as the Newtonian case. We see then that viscoelastic effects do not affect the flow field at linear order in ϵ.

Now it is important to note that while the first order stream function is strictly Newtonian, and hence $\mathbf{u}_1$ and $\dot{\boldsymbol{\gamma}}_1$ are Newtonian, the first order stress field $\boldsymbol{\tau}_1$ is not, as a Laplace transform of the first order constitutive relation reveals,

$$\bar{\boldsymbol{\tau}}_1 = \frac{1+\mathrm{De}_2 s}{1+\mathrm{De}_1 s}\bar{\dot{\boldsymbol{\gamma}}} + \frac{\mathrm{De}_1 - \mathrm{De}_2}{1+\mathrm{De}_1 s}\dot{\boldsymbol{\gamma}}(t=0). \tag{6.15}$$

The right-hand side is entirely known and then from an inverse transform we can obtain $\boldsymbol{\tau}_1$.

6.5.2 Second order

For the swimming speed at second order the boundary conditions are

$$\begin{aligned}\boldsymbol{\nabla}\Psi_2|_{y=0} &= -g(z)\boldsymbol{\nabla}\frac{\partial\Psi_1}{\partial y} + \frac{\mathbf{e}_y}{2}\left[g'(z)^2 - \left\langle g'(z)^2\right\rangle\right], \\ \boldsymbol{\nabla}\Psi_2|_{y\to\infty} &= -U_2\mathbf{e}_y\end{aligned} \tag{6.16}$$

We are really only interested in the mean term, in x, as that yields the swimming speed and thus we extract it from

$$\begin{aligned}\left.\frac{\partial \Psi_2^{(0)}}{\partial y}\right|_{y=0} &= -\left\langle g(z)\left.\frac{\partial^2 \Psi_1}{\partial y^2}\right|_{y=0}\right\rangle, \\ &= -\left\langle \sum_n c_n e^{inz} \sum_m -m^2 c_m e^{imz} \right\rangle, \\ &= \sum_n n^2 c_n c_n^*, \end{aligned} \tag{6.17}$$

which in the Laplace domain is

$$\left.\boldsymbol{\nabla}\bar{\Psi}_2^{(0)}\right|_{y=0} = \frac{1}{s}\sum_n n^2 c_n c_n^*. \tag{6.18}$$

The second order constitutive relation yields

$$\begin{aligned}\left(1+\mathrm{De}_1\frac{\partial}{\partial t}\right)\boldsymbol{\tau}_2 - \left(1+\mathrm{De}_2\frac{\partial}{\partial t}\right)\dot{\boldsymbol{\gamma}}_2 = \\ \Bigg[\mathrm{De}_1\left(\boldsymbol{\nabla}\mathbf{u}_1^{\mathrm{T}}\cdot\boldsymbol{\tau}_1 + \boldsymbol{\tau}_1\cdot\boldsymbol{\nabla}\mathbf{u}_1 - \mathbf{u}_1\cdot\boldsymbol{\nabla}\boldsymbol{\tau}_1\right) \\ -\mathrm{De}_2\left(\boldsymbol{\nabla}\mathbf{u}_1^{\mathrm{T}}\cdot\dot{\boldsymbol{\gamma}}_1 + \dot{\boldsymbol{\gamma}}_1\cdot\boldsymbol{\nabla}\mathbf{u}_1 - \mathbf{u}_1\cdot\boldsymbol{\nabla}\dot{\boldsymbol{\gamma}}_1\right)\Bigg].\end{aligned} \tag{6.19}$$

At this point the calculation becomes too laborious to continue for general waveforms and we proceed only with Taylor's sinusoidal sheet $\tilde{c}_1 = -i/2$. Substituting into (6.19) and taking the divergence and the curl we obtain

$$\begin{aligned}\left(1+\mathrm{De}_2\frac{\partial}{\partial t}\right)\nabla^4\Psi_2 = \frac{8\mathrm{De}_1(\mathrm{De}_1-\mathrm{De}_2)}{1+\mathrm{De}_1^2}\left(1-3y+y^2\right)e^{-2y} \\ \times\left[1+(\mathrm{De}_1\sin t-\cos t)e^{-\frac{t}{\mathrm{De}_1}}\right].\end{aligned} \tag{6.20}$$

Here we see a distinct transient forcing term on the right-hand side. Upon a Laplace transform, again taking the initial condition to be Newtonian, we are left with

$$\begin{aligned}(1+s\mathrm{De}_2)\nabla^4\bar{\Psi}_2 = \frac{8\mathrm{De}_1(\mathrm{De}_1-\mathrm{De}_2)}{1+\mathrm{De}_1^2}\left(1-3y+y^2\right)e^{-2y} \\ \times\left[\frac{\left(1+\mathrm{De}_1^2\right)(1+\mathrm{De}_1 s)}{s\left(1+\mathrm{De}_1\left(\mathrm{De}_1+2s+\mathrm{De}_1 s^2\right)\right)}\right].\end{aligned} \tag{6.21}$$

The particular solution in the Laplace domain may be obtained directly by integration

$$\bar{\Psi}_{2p} = \frac{\mathrm{De}_1(\mathrm{De}_1 - \mathrm{De}_2)e^{-2y}\left(y + y^2\right)\left(1 + \mathrm{De}_1 s\right)}{2s\left(1 + \mathrm{De}_1\left(\mathrm{De}_1 + 2s + \mathrm{De}_1 s^2\right)\right)\left(1 + s\mathrm{De}_2\right)}. \tag{6.22}$$

We care only about the zeroth term in the general solution, as this gives the swimming speed, and hence we find

$$\tilde{b}_0 = \frac{1}{2s} - \frac{\mathrm{De}_1(\mathrm{De}_1 - \mathrm{De}_2)(1 + \mathrm{De}_1 s)}{2s\left(1 + \mathrm{De}_1\left(\mathrm{De}_1 + 2s + \mathrm{De}_1 s^2\right)\right)\left(1 + s\mathrm{De}_2\right)}. \tag{6.23}$$

Now taking $\mathrm{De}_1 = \mathrm{De}$ and $\mathrm{De}_2 = \beta\mathrm{De}$ we obtain for the swimming speed of the sheet

$$U = -\frac{1}{2}\left[\frac{1 + \beta\mathrm{De}^2}{\left(1 + \mathrm{De}^2\right)} - \frac{\beta\mathrm{De}^2(1-\beta)^2}{(1-\beta)^2 + \beta^2\mathrm{De}^2}e^{-\frac{t}{\beta\mathrm{De}}} + \frac{\mathrm{De}^2(\beta - 1)e^{it}}{2\left(1 - i\mathrm{De} + (i + \mathrm{De})^2\beta\right)}e^{-\frac{t}{\mathrm{De}}} + c.c.\right]. \tag{6.24}$$

We see that the swimming speed has three distinct components: a steady state swimming speed and two transient responses. One transient response is oscillatory and decays on the relaxation time scale of the polymer while the other term is a steady decay on the retardation time-scale of the fluid. In Fig. 6.1 we plot the transient swimming response from a Newtonian initial condition and we see there exist scenarios in which the transient swimming speed can far surpass the steady state swimming speed (and even the initial swimming speed), which raises the question of whether or not microorganisms can utilize the transient response of the polymeric fluid for 'rapid' maneuvering.

6.6 Steady state

When we are only concerned with the steady state swimming speed it is far easier simply to focus on the post transient field from the start, as we demonstrate in this section.

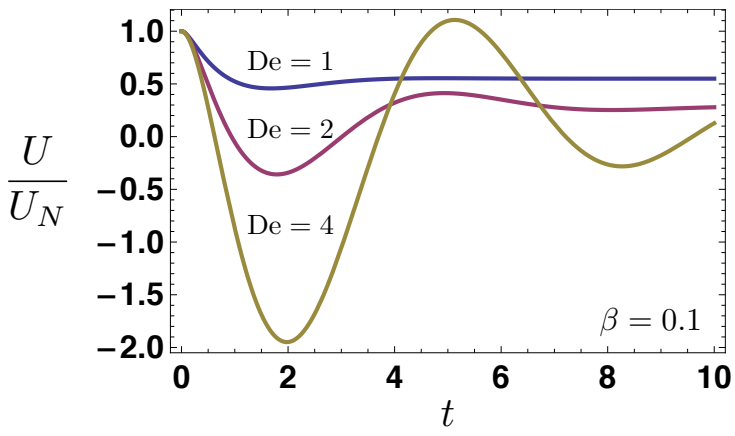

Figure 6.1: The ratio of transient swimming speed in a viscoelastic fluid to Newtonian swimming speed. We see that for certain choices of parameters we can obtain an enhanced speed on transient time scales.

6.6.1 Time

We stipulate that all fields are time-periodic

$$\Psi(x,y,t) = \sum_{n=-\infty}^{\infty} \tilde{\psi}^{(n)}(x,y)e^{-nit}. \tag{6.25}$$

By writing that the fields may be decomposed into purely harmonic components in time we are hence looking at post transient behavior, with the Fourier modes dictated by the boundary conditions. Indeed we will see that the t and x dependency can be written entirely in terms of a wave variable $z = x - t$.

6.6.2 Fourier modes

We decompose (6.6) into its Fourier modes in time at each order in the expansion. For example at second order we obtain

$$\boldsymbol{\tau}_2^{(0)} - \dot{\boldsymbol{\gamma}}_2^{(0)} = \frac{1}{2}\mathrm{Re}\left[\frac{\mathrm{De}_1 - \mathrm{De}_2}{1 - i\mathrm{De}_1}\left(\boldsymbol{\nabla}\tilde{\mathbf{u}}_1^{(1)\mathrm{T}} \cdot \tilde{\dot{\boldsymbol{\gamma}}}_1^{(1)*} + \tilde{\dot{\boldsymbol{\gamma}}}_1^{(1)*} \cdot \boldsymbol{\nabla}\tilde{\mathbf{u}}_1^{(1)} - \tilde{\mathbf{u}}_1^{(1)} \cdot \boldsymbol{\nabla}\tilde{\dot{\boldsymbol{\gamma}}}_1^{(1)*}\right)\right] \tag{6.26}$$

and

$$(1 - 2i\mathrm{De}_1)\tilde{\boldsymbol{\tau}}_2^{(2)} - (1 - 2i\mathrm{De}_2)\tilde{\dot{\boldsymbol{\gamma}}}_2^{(2)} = \frac{1}{2}\frac{\mathrm{De}_1 - \mathrm{De}_2}{1 - i\mathrm{De}_1}\left(\boldsymbol{\nabla}\tilde{\mathbf{u}}_1^{(1)\mathrm{T}} \cdot \tilde{\dot{\boldsymbol{\gamma}}}_1^{(1)} + \tilde{\dot{\boldsymbol{\gamma}}}_1^{(1)} \cdot \boldsymbol{\nabla}\tilde{\mathbf{u}}_1^{(1)} - \tilde{\mathbf{u}}_1^{(1)} \cdot \boldsymbol{\nabla}\tilde{\dot{\boldsymbol{\gamma}}}_1^{(1)}\right) \tag{6.27}$$

For convenience, we label the right-hand side of the above $\tilde{\mathbf{A}}_2^{(0)}$ and $\tilde{\mathbf{A}}_2^{(2)}$ respectively. In general the constitutive relations at order j for the n Fourier mode are given by

$$(1 - ni\mathrm{De}_1)\tilde{\boldsymbol{\tau}}_j^{(n)} - (1 - ni\mathrm{De}_2)\tilde{\dot{\boldsymbol{\gamma}}}_j^{(n)} = \tilde{\mathbf{A}}_j^{(n)} \tag{6.28}$$

If j is even then n is even and $n \in [1, j]$. Conversely for odd j then n is odd and $n \in [1, j]$. Upon taking the divergence and the curl of each equation we obtain a forced biharmonic equation for the stream function

$$\mathbf{e}_z \nabla^4 \tilde{\Psi}_j^{(n)} = \frac{1}{(1 - ni\mathrm{De}_2)} \boldsymbol{\nabla} \times \boldsymbol{\nabla} \cdot \tilde{\mathbf{A}}_j^{(n)} \tag{6.29}$$

Given that the zeroth mode has no x dependence we simply obtain

$$\nabla^4 \Psi_j^{(0)} = -\frac{d^2}{dy^2} \tilde{\mathbf{A}}_j^{(0)}[1, 2] \tag{6.30}$$

6.6.3 First order

The Oldroyd-B equation to first order is

$$\boldsymbol{\tau}_1 + \mathrm{De}_1 \frac{\partial \boldsymbol{\tau}_1}{\partial t} = \boldsymbol{\gamma}_1 + \mathrm{De}_2 \frac{\partial \boldsymbol{\gamma}_1}{\partial t}, \tag{6.31}$$

and hence for each Fourier mode we have

$$\tilde{\boldsymbol{\tau}}_1^{(n)} = \frac{1 - ni\mathrm{De}_2}{1 - ni\mathrm{De}_1} \tilde{\dot{\boldsymbol{\gamma}}}_1^{(n)} \tag{6.32}$$

The boundary conditions are

$$\boldsymbol{\nabla} \tilde{\psi}_1^{(n)} \Big|_{y=0} = \boldsymbol{\nabla} g(z) = ni\tilde{c}_n e^{niz} \mathbf{e}_x. \tag{6.33}$$

From the general solution we obtain

$$\boldsymbol{\nabla} \tilde{\psi}_1^{(n)} \Big|_{y=0} = \left[in\tilde{a}_n \mathbf{e}_x + (-|n|\, \tilde{a}_n + \tilde{b}_n)\mathbf{e}_y \right] e^{inx}, \tag{6.34}$$

therefore $\tilde{a}_n = \tilde{c}_n$ and $\tilde{b}_n = |n|\, \tilde{c}_n$, leaving

$$\Psi_1 = \sum_{n=-\infty}^{\infty} \tilde{c}_n (1 + |n|\, y) e^{-|n|y} e^{inz}. \tag{6.35}$$

For Taylors sinusoidal swimming sheet we have $\tilde{c}_1 = -i/2$ yielding $\Psi_1 = (1 + y)e^{-y} \sin z$. As in the transient calculation, we see the that the linear flow field is strictly Newtonian.

6.6.4 Second order

For the swimming speed at second order the boundary conditions are

$$\boldsymbol{\nabla}\psi_2|_{y=0} = -g(z)\boldsymbol{\nabla}\frac{\partial\psi_1}{\partial y} + \frac{\mathbf{e}_y}{2}\left[g'(z)^2 - \left\langle g'(z)^2\right\rangle\right] \tag{6.36}$$

If we are only interested in the swimming speed at second order then we may ignore all terms but the mean term since that is the only term that affects the second order swimming speed, and as we showed above

$$\left.\frac{\partial\tilde{\psi}_2^{(0)}}{\partial y}\right|_{y=0} = \sum_n n^2\tilde{c}_n\tilde{c}_n^*. \tag{6.37}$$

However, if we wish to proceed to higher order we need to find all modes present in ψ_2.

The equation governing the zeroth mode at second order as shown above is

$$\boldsymbol{\tau}_2^{(0)} - \boldsymbol{\gamma}_2^{(0)} = \sum_n\left[\frac{\mathrm{De}_1 - \mathrm{De}_2}{1 - in\mathrm{De}_1}\left(\boldsymbol{\nabla}\tilde{\mathbf{u}}_1^{(\mathrm{n})\mathrm{T}}\cdot\tilde{\dot{\boldsymbol{\gamma}}}_1^{(n)*} + \tilde{\dot{\boldsymbol{\gamma}}}_1^{(n)*}\cdot\boldsymbol{\nabla}\tilde{\mathbf{u}}_1^{(n)} - \tilde{\mathbf{u}}_1^{(n)}\cdot\boldsymbol{\nabla}\tilde{\dot{\boldsymbol{\gamma}}}_1^{(n)*}\right)\right]. \tag{6.38}$$

After taking the divergence and curl we obtain a forced biharmonic equation for the stream function

$$\nabla^4\psi_2^{(0)} = \sum_n\frac{8\tilde{c}_n\tilde{c}_n^*\mathrm{De}_1(\mathrm{De}_1 - \mathrm{De}_2)e^{-2|n|y}n^6\left(|n|\left(1 + y^2n^2\right) - 3n^2y\right)}{1 + n^2\mathrm{De}_1^2}. \tag{6.39}$$

The particular solution may be found by integration and when adding the homogeneous solution and taking into account the boundary conditions we may obtain the second order swimming speed,

$$\begin{aligned} U_2 &= -\sum_n n^2\tilde{c}_n\tilde{c}_n^*\frac{1 + n^2\mathrm{De}_1\mathrm{De}_2}{1 + n^2\mathrm{De}_1^2}, \\ &= -\sum_n n^2\tilde{c}_n\tilde{c}_n^*\frac{1 + n^2\mathrm{De}^2\beta}{1 + n^2\mathrm{De}^2}. \end{aligned} \tag{6.40}$$

For the Taylor sinusoidal swimming sheet the only nonzero coefficient is $\tilde{c}_1 = -i/2$. We see of course that we recover the steady state limit from the transient calculation presented above. Here we take the time to highlight the factor

$$\Upsilon_n = \frac{1 + n^2\mathrm{De}^2\beta}{1 + n^2\mathrm{De}^2} \tag{6.41}$$

which separates the viscoelastic swimming speed from the Newtonian one. We point out this factor because it will occur in all the classical variants of the swimming sheet problem we consider below.

6.7 Steady swimming near a wall

Another classical swimming problem is the swimming sheet near a wall. On the swimmer we have the same boundary condition but now we stipulate that a well exists at $y = h$ where we have no slip, $\mathbf{u} = \mathbf{0}$. In the frame moving with the swimmer we then have

$$\boldsymbol{\nabla}\psi|_{y=h} = -U\mathbf{e}_y. \tag{6.42}$$

We again look for solutions in terms of a regular perturbation series, $U = \sum_n \epsilon^n U_n$.

6.7.1 First order

The boundary conditions are

$$\boldsymbol{\nabla}\tilde{\psi}_1^{(n)}\Big|_{y=0} = \boldsymbol{\nabla}g(z) = ni\tilde{c}_n e^{niz}, \tag{6.43}$$

$$\boldsymbol{\nabla}\psi_1|_{y=h} = -U_1\mathbf{e}_y. \tag{6.44}$$

With the first order boundary conditions we arrive at the stream function

$$\begin{aligned}\psi_1 = {} & \frac{U_1 - 3\tilde{d}_0 h^2}{2h}y^2 + \tilde{d}_0 y^3 \\ & + \sum_{n\neq 0} e^{inx}\Big[\cosh ny\left(\tilde{c}_n - \frac{ny\tilde{c}_n(2hn + \sinh[2hn])}{1 + 2h^2n^2 - \cosh[2hn]}\right) \qquad (6.45) \\ & + \sinh ny\left(\frac{\tilde{c}_n(2hn - ny + ny\cosh[2hn] + \sinh[2hn])}{1 + 2h^2n^2 - \cosh[2hn]}\right)\Big]. \qquad (6.46)\end{aligned}$$

Now at this point we must resort to dynamical considerations to resolve the unknown coefficient, namely enforcing that the swimmer (and thus the wall) is force free, to find $\tilde{d}_0 = 0$ and hence $U_1 = 0$.

6.7.2 Second order

Again at second order we only compute the mean component of the boundary conditions

$$\left.\frac{\partial \psi_2^{(0)}}{\partial y}\right|_{y=0} = \sum_n \tilde{c}_n \tilde{c}_n^* n^2 \frac{1 - 2h^2m^2 - \cosh[2hm]}{1 + 2h^2m^2 - \cosh[2hm]}, \tag{6.47}$$

$$\left.\frac{\partial \tilde{\psi}_2^{(0)}}{\partial y}\right|_{y=h} = -U_2. \tag{6.48}$$

From this we compute the inhomogeneous second order biharmonic equation. Since the mean contains no x dependency we can simply integrate to obtain the particular solution. The problem is closed by assuming both the sheet and the wall are force free. The swimming speed is then found to be

$$U_2 = -\sum_n n^2 \tilde{c}_n \tilde{c}_n^* \frac{\sinh^2 nh + n^2h^2}{\sinh^2 nh - n^2h^2} \Upsilon_n. \tag{6.49}$$

We see again that the classical result for swimming speed near a wall, to leading order, is simply modified by the factor Υ_n for every Fourier mode in the shape of the traveling wave.

6.8 Peristaltic pumping

We now think consider the case of peristaltic pumping between two oscillating walls with a phase difference of ϕ.

$$\begin{aligned} y_h &= h + \epsilon \tilde{c}_n e^{inz} \\ y_{-h} &= -h + \epsilon \tilde{c}_n e^{in(z+\phi)} = -h + \epsilon \tilde{\alpha}_n e^{inz} \end{aligned} \tag{6.50}$$

6.8.1 First order

The boundary conditions are

$$\boldsymbol{\nabla} \tilde{\psi}_1^{(n)} \Big|_{y=h} = ni\tilde{c}_n e^{niz} \mathbf{e}_x \tag{6.51}$$

$$\boldsymbol{\nabla} \tilde{\psi}_1^{(n)} \Big|_{y=-h} = ni\tilde{\alpha}_n e^{niz} \mathbf{e}_x \tag{6.52}$$

With the first order boundary conditions we arrive at the stream function

$$\begin{aligned}\psi_1 = &\ \tilde{d}_0 y\left(y^2 - 3h^2\right) \\ &+ \sum_{n\neq 0} e^{inx}\Bigg[\cosh ny\left(-\frac{ny(\tilde{c}_n - \tilde{\alpha}_n)\cosh[hn]}{-2hn + \sinh[2hn]} + \frac{(\tilde{c}_n + \tilde{\alpha}_n)(hn\cosh[hn] + \sinh[hn])}{2hn + \sinh[2hn]}\right) \\ &+ \sinh ny\left(\frac{(\tilde{c}_n - \tilde{\alpha}_n)(\cosh[hn] + hn\sinh[hn])}{-2hn + \sinh[2hn]} - \frac{ny(\tilde{c}_n + \tilde{\alpha}_n)\sinh[hn]}{2hn + \sinh[2hn]}\right)\Bigg] \quad (6.53)\end{aligned}$$

If there is no imposed pressure drop, then $\tilde{d}_0 = 0$. Otherwise $\tilde{d}_0 = -\Delta P/6$.

6.8.2 Second order

The mean component of the boundary condition at the top wall is

$$\left.\frac{\partial \psi_2^{(0)}}{\partial y}\right|_{y=h} = \sum_n \tilde{c}_n \tilde{c}_n^* n^2 \left(\frac{\sinh[2nh]^2 + 4n^2h^2}{\sinh[2nh]^2 - 4n^2h^2} - e^{-in\phi}\frac{4hn\sinh[2hn]}{\sinh[2nh]^2 - 4n^2h^2}\right) \quad (6.54)$$

while at the bottom wall

$$\left.\frac{\partial \psi_2^{(0)}}{\partial y}\right|_{y=-h} = \sum_n \tilde{c}_n \tilde{c}_n^* n^2 \left(\frac{\sinh[2nh]^2 + 4n^2h^2}{\sinh[2nh]^2 - 4n^2h^2} - e^{in\phi}\frac{4hn\sinh[2hn]}{\sinh[2nh]^2 - 4n^2h^2}\right) \quad (6.55)$$

By the same methodology above, and assuming no second order pressure drop we find a flow-rate Q of

$$Q = \int_{-h}^{h} \frac{\partial \psi_2}{\partial y} dy \quad (6.56)$$

$$= \sum_n 2hn^2 \tilde{c}_n \tilde{c}_n^* \left(\frac{\mathrm{Sinh}[2hn]^2 + 4h^2n^2}{\mathrm{Sinh}[2hn]^2 - 4h^2n^2} - \frac{4hn\mathrm{Cos}[n\phi]\mathrm{Sinh}[2hn]}{\mathrm{Sinh}[2hn]^2 - 4h^2n^2}\right)\Upsilon_n \quad (6.57)$$

which is again identical to the Newtonian result with the exclusion of Υ_n.

6.9 Steady swimming sheet, higher order

The leading order steady swimming speed, U_2, for Taylor's swimming sheet, $\tilde{c}_1 = -i/2$ and $\tilde{c}_n = 0$ for all other n, was first found by Lauga [59]. Here we present the swimming speed at the next two non-zero orders in the asymptotic series, the fourth and the sixth. While laborious in practice, the results can be found with a straight forward application of the formalism presented above, in particular section 6.6.2.

6.9.1 Boundary conditions

For large amplitude (ϵ) transverse oscillations of the sheet it is necessary, as we showed in Chapter 3, to recast the boundary conditions so that the sheet remains inextensible. These boundary conditions for a sinusoidal sheet were first described by Taylor [13] and catalogued in detail, for general waveforms, in [68]. The boundary conditions are

$$u\,|_{y=y_1} = 1 - \alpha\cos\theta\,|_{y=y_1}, \tag{6.58a}$$

$$v\,|_{y=y_1} = -\alpha\sin\theta\,|_{y=y_1} \tag{6.58b}$$

where the angle, θ, is defined by $\tan\theta = \partial y/\partial z$. Hence

$$\cos\theta = \frac{1}{\sqrt{1+(y')^2}}, \tag{6.59}$$

$$\sin\theta = y'\cos\theta, \tag{6.60}$$

and the material velocity (in the wave frame), α, is ratio of the length of the sheet to its wavelength multiplied by the wave speed, or

$$\alpha = \frac{1}{2\pi}\int_0^{2\pi}\sqrt{1+\left(\frac{\partial y}{\partial x}\right)^2}\,dx. \tag{6.61}$$

Expanding the boundary conditions we obtain

$$u\,|_{y=y_1} = \mathrm{Re}\left[\left(\frac{1}{4}e^{2iz}\right)\epsilon^2 - \frac{1}{64}\left(2+8e^{2iz}+3e^{4iz}\right)\epsilon^4\right. \tag{6.62}$$

$$\left. + \left(\frac{1}{32}+\frac{45}{512}e^{2iz}+\frac{3}{64}e^{4iz}+\frac{5}{512}e^{6iz}\right)\epsilon^6\right] \tag{6.63}$$

$$-v\,|_{y=y_1} = \mathrm{Re}\left[\left(e^{iz}\right)\epsilon - \left(\frac{e^{iz}}{8}+\frac{1}{8}e^{3iz}\right)\epsilon^3 + \frac{1}{128}\left(12e^{iz}+11e^{3iz}+3e^{5iz}\right)\epsilon^5\right] \tag{6.64}$$

6.9.2 Results

Following the methodology presented above, a perturbation expansion in ϵ, we obtain a inhomogeneous biharmonic equation at each order for each Fourier mode, the stream function then satisfying each such equation and the appropriate

part of the boundary condition leads to the solution of the flow field at each order. The details are lengthy and laborious and omitted here for clarity. Noting that $b_j^{(0)} = -U_j$ gives the swimming speed at each order and $\mathrm{De}_2 = \eta_r \mathrm{De}$ we give the results at each order below.

At second order we repeat the Lauga [59] result

$$U_2 = -\frac{1 + \mathrm{De}^2 \eta_r}{2\left(1 + \mathrm{De}^2\right)}. \tag{6.65}$$

As Lauga found, this indicates that at leading order the swimming speed is strictly less than the swimming speed in a Newtonian fluid.

At fourth order we find

$$U_4 = \frac{\left(\left(1 + \mathrm{De}^2 \eta_r\right)\left(76 + 50\mathrm{De}^2 + 47\mathrm{De}^4 + \mathrm{De}^2\left(102 + 29\mathrm{De}^2\right)\eta_r + \mathrm{De}^2\left(76 + 45\mathrm{De}^2 + 42\mathrm{De}^4\right)\eta_r^2 + \mathrm{De}^4\left(107 + 34\mathrm{De}^2\right)\eta_r^3\right)\right)}{\left(128\left(1 + \mathrm{De}^2\right)^3\left(1 + \mathrm{De}^2\eta_r^2\right)\right)}. \tag{6.66}$$

Hence there exist regimes where the viscoelastic swimming speed is faster than the Newtonian swimming speed (at equivalent order) near $\mathrm{De} = 1$, but only for relatively large amplitudes.

Finally at sixth order we find the mercilessly lengthy formula

$$\begin{aligned}
U_6 = \Big[& 956448 \\
& + \mathrm{De}^2\left(4377888 + 57875730\mathrm{De}^2 + 185430852\mathrm{De}^4 + 133190147\mathrm{De}^6 + 180283105\mathrm{De}^8 + 48775484\mathrm{De}^{10} + 13846644\mathrm{De}^{12}\right)\eta_r \\
& + 3\mathrm{De}^2\left(1912896 + 27553473\mathrm{De}^2 + 111625168\mathrm{De}^4 + 169957123\mathrm{De}^6 + 198981546\mathrm{De}^8 + 96543501\mathrm{De}^{10} + 29566863\mathrm{De}^{12}\right)\eta_r^2 \\
& + \mathrm{De}^4\left(25917048 + 345637148\mathrm{De}^2 + 1134451024\mathrm{De}^4 + 907319288\mathrm{De}^6 + 1157711741\mathrm{De}^8 + 325926653\mathrm{De}^{10} + 77353668\mathrm{De}^{12}\right)\eta_r^3 \\
& + \mathrm{De}^4\left(8608032 + 147895752\mathrm{De}^2 + 823387667\mathrm{De}^4 + 1743774767\mathrm{De}^6 + 1309807855\mathrm{De}^8 + 905882638\mathrm{De}^{10} + 223458219\mathrm{De}^{12}\right)\eta_r^4 \\
& + \mathrm{De}^6\left(39247080 + 533168575\mathrm{De}^2 + 1833453005\mathrm{De}^4 + 1671026336\mathrm{De}^6 + 1705865570\mathrm{De}^8 + 479056216\mathrm{De}^{10} + 113365368\mathrm{De}^{12}\right)\eta_r^5 \\
& + \mathrm{De}^6\left(3825792 + 102195918\mathrm{De}^2 + 853535920\mathrm{De}^4 + 2264397416\mathrm{De}^6 + 1203975005\mathrm{De}^8 + 1002144235\mathrm{De}^{10} + 202656204\mathrm{De}^{12}\right)\eta_r^6 \\
& + \mathrm{De}^8\left(17717280 + 256438610\mathrm{De}^2 + 1030708045\mathrm{De}^4 + 1343615553\mathrm{De}^6 + 884993510\mathrm{De}^8 + 236388088\mathrm{De}^{10} + 47120544\mathrm{De}^{12}\right)\eta_r^7 \\
& + 4\mathrm{De}^{10}\left(1 + 9\mathrm{De}^2\right)\left(5967006 + 25953014\mathrm{De}^2 + 10302134\mathrm{De}^4 + 10165819\mathrm{De}^6 + 1837552\mathrm{De}^8\right)\eta_r^8 \\
& + 4\mathrm{De}^{12}\left(1 + 4\mathrm{De}^2\right)\left(1 + 9\mathrm{De}^2\right)\left(2621142 + 789627\mathrm{De}^2 + 169834\mathrm{De}^4\right)\eta_r^9\Big] \\
& \times \left(1492992\left(1 + \mathrm{De}^2\right)^5\left(1 + 13\mathrm{De}^2 + 36\mathrm{De}^4\right)\left(1 + \mathrm{De}^2\eta_r^2\right)^2\left(1 + 4\mathrm{De}^2\eta_r^2\right)\right)^{-1}.
\end{aligned} \tag{6.67}$$

At this order the swimming speed is again strictly less than the swimming speed in a Newtonian fluid, for all ϵ.

The swimming speed in a viscoelastic fluid, asymptotically valid up to sixth order is hence

$$U = \epsilon^2(U_2 + \epsilon^2 U_4 + \epsilon^4 U_6) + \mathcal{O}(\epsilon^8). \tag{6.68}$$

Again all odd terms in the expansion are zero by symmetry.

As expected, when we take De = 0 we obtain the swimming speed in a Newtonian fluid to sixth order

$$U_N = -\frac{\epsilon^2}{2}\left(1 - \frac{19}{16}\epsilon^2 + \frac{41}{32}\epsilon^4\right) + \mathcal{O}(\epsilon^8). \tag{6.69}$$

where the first two terms were found by Taylor [13], while the third was later found by Drummond [79].

There is some debate in the literature whether large amplitude gaits may see a swimming speed increase in viscoelastic fluids, near De = 1, as found in experiments by Liu *et al.* [80], and numerics by Teran *et al.* [81] and as displayed by our fourth order accurate formula, or as demonstrated in another set of experiments with *C. Elegans* swimming in viscoelastic fluids by Shen and Arratia [82] there is instead strictly a swimming speed decrease (as with the second or sixth order accurate formulae). Sadly our results are inconclusive on this matter.

6.10 Conclusion

Because many microorganisms swim immersed in biological fluids which are non-Newtonian, in this chapter we introduced swimming in a viscoelastic Oldroyd-B fluid. We first demonstrated that there are transient effects on the swimming speed of a microorganism decaying both on the relaxation timescale and retardation timescale. Secondly the steady state swimming speed is strictly lower in a viscoelastic fluid compared to a Newtonian fluid at leading order and the difference was shown to be determined by a factor that depends on each Fourier mode which constitute the swimming waveform. This factor was found to be identical in other classical results such as swimming next to a wall and peristaltic pumping. Finally we presented the next two terms in the asymptotic series for the swimming speed of a sinusoidal sheet in an unbounded fluid.

Chapter 6, in small part, is a reprint of the material as it appears in the Journal of Fluid Mechanics 2010. Elfring, Gwynn J.; Pak, On Shun; Lauga, Eric, Cambridge University Press, 2010. The dissertation author was the primary investigator and author of this paper.

Chapter 7

Non-Newtonian synchronization

7.1 Introduction

In all previously-studied situations, synchronization was addressed in the case of a Newtonian fluid. In this chapter we study the passive synchronization of two flagellated cells in a viscoelastic (Oldroyd-B) fluid. Using Taylor's infinite two-dimensional sheet model, we show that not only does phase locking arise in a viscoelastic fluid, but also that it does not require the front-back geometrical asymmetry that must exist for such a model to display synchronization in a Newtonian fluid. We demonstrate that the system evolves to a single stable fixed point at the in-phase conformation, which is also the conformation that yields minimal energy dissipation. In addition, we show that the evolution to a phase-locked state occurs on asymptotically faster time scales than in a Newtonian fluid.

7.2 Setup

Our system, shown in Fig. 7.1, consists of two parallel infinite two-dimensional sheets, separated by a mean distance h. Both sheets propagate sinusoidal waves of transverse displacement of amplitude a at speed $c = \omega/k$, where ω is the wave frequency and k is the wavenumber, but have an initial phase difference ϕ_0. By passing these waves, the sheets propel themselves in the direction opposite to the wave speed [13]. The sheets are also permitted to move relative to each other with an un-

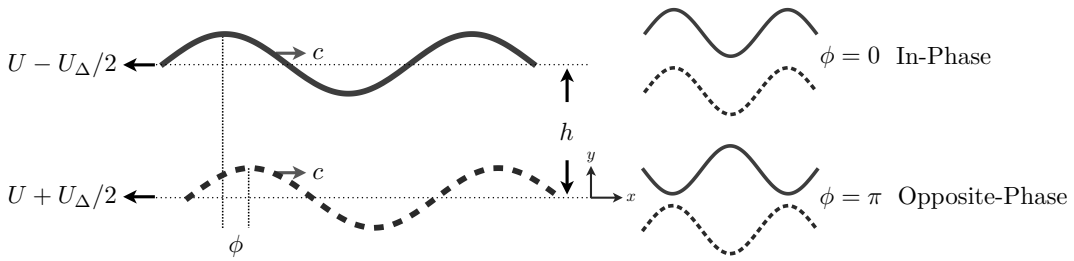

Figure 7.1: Model system consisting of two infinite sinusoidal sheets passing waves at speed c and thereby swimming at speed $U \pm U_\Delta/2$ in the opposite direction. The difference in phase ϕ incurs a relative velocity $U_\Delta(\phi, h)$ between the two sheets denoted positive when the top sheet swims to the right relative to the bottom one. The average separation distance is denoted h.

known velocity U_Δ, denoted positive when the top sheet (#2) swims in the positive x direction relative to the bottom one (#1). The positions of the sheets, in their swimming frames, are thereby given by $y_1 = a\sin(kx - \omega t - \phi_0/2 + \int_0^t kU_\Delta(t')dt'/2)$ and $y_2 = h + a\sin(kx - \omega t + \phi_0/2 - \int_0^t kU_\Delta(t')dt'/2)$.

We use the following dimensionless variables $x^* = xk$, $t^* = t\omega$, $\mathbf{u}^* = \mathbf{u}/c$, $U_\Delta^* = U_\Delta/c$. The amplitude of the waves is non-dimensionalized by the wavenumber, $\epsilon = ak$. For convenience we let $z^* = x^* - t^*$ and $\phi = \phi_0 - \int_0^{t^*} U_\Delta^*(t')dt'$ which is the instantaneous phase difference between the two sheets. The position of the sheets in dimensionless form is thus given by $y_1^* = \epsilon\sin(z^* - \phi/2)$, and $y_2^* = h^* + \epsilon\sin(z^* + \phi/2)$, and the phase evolves in time according to $\dot{\phi} = -U_\Delta^*$. We refer to the $\phi = 0$ conformation as in-phase, and the $\phi = \pi$ conformation as opposite-phase. The system is 2π periodic and ϕ is defined from $-\pi$ to π. We now drop the $(^*)$ notation and refer only below to dimensionless variables.

Since this problem is two dimensional, we introduce the streamfunction $\psi(x, y, t)$ where the components of the velocity field are $\mathbf{u} = [u, v]^{\mathrm{T}} = [\partial\psi/\partial y, -\partial\psi/\partial x]^{\mathrm{T}}$, and the incompressibility condition is always satisfied. The boundary conditions then become

$$\boldsymbol{\nabla}\psi|_{y=y_1} = \boldsymbol{\nabla}\Big[-U_\Delta y/2 + \epsilon\sin(z - \phi/2)\Big]\Big|_{y=y_1}, \tag{7.1}$$

$$\boldsymbol{\nabla}\psi|_{y=y_2} = \boldsymbol{\nabla}\Big[U_\Delta y/2 + \epsilon\sin(z + \phi/2)\Big]\Big|_{y=y_2}. \tag{7.2}$$

We solve this problem, in the post-transient limit, using the perturbative

formalism presented in the previous chapter.

7.3 Analysis

7.3.1 First-order solution

The leading order component of (6.3) is

$$\boldsymbol{\tau}_1 + \mathrm{De}_1 \frac{\partial \boldsymbol{\tau}_1}{\partial t} = \boldsymbol{\gamma}_1 + \mathrm{De}_2 \frac{\partial \boldsymbol{\gamma}_1}{\partial t}. \tag{7.3}$$

Taking the divergence and the curl of (7.3) we get the governing equation for the first-order streamfunction

$$\left(1 + \mathrm{De}_2 \frac{\partial}{\partial t}\right) \nabla^4 \psi_1 = 0. \tag{7.4}$$

With the first order boundary conditions

$$\boldsymbol{\nabla}\psi_1|_{y=0} = \boldsymbol{\nabla}\left[(-U_{\Delta 1} y/2 + \sin(z - \phi/2)\right]|_{y=0}, \tag{7.5}$$

$$\boldsymbol{\nabla}\psi_1|_{y=h} = \boldsymbol{\nabla}\left[U_{\Delta 1} y/2 + \sin(z + \phi/2)\right]|_{y=h}, \tag{7.6}$$

the solution can be shown to be

$$\psi_1 = a_0(y) + a_1(y)\cos(z) + b_1(y)\sin(z), \tag{7.7}$$

where

$$a_0(y) = \mathrm{C}_1 y^2 \left(y - \frac{3}{2}h\right) + \frac{1}{2} U_{\Delta 1} y \left(\frac{y}{h} - 1\right), \tag{7.8}$$

$$a_1(y) = \frac{\sin\frac{\phi}{2}}{h - \sinh(h)}\Big(y\cosh(h-y) - (h-y)\cosh y + \sinh(h-y) - \sinh y\Big), \tag{7.9}$$

$$b_1(y) = \frac{\cos\frac{\phi}{2}}{h + \sinh(h)}\Big(y\cosh(h-y) + (h-y)\cosh y + \sinh(h-y) + \sinh y\Big). \tag{7.10}$$

To determine the unknown constant C_1 we resort to dynamical considerations. For simplicity we resolve the streamfunction into its complex Fourier

components in the wave variable $z = x - t$ giving $\psi_1 = \mathrm{Re}\left[\tilde{\psi}_1^{(0)} + \tilde{\psi}_1^{(1)}\right]$, where Re[...] denotes the real part and $\tilde{\psi_1}^{(0)} = a_0(y)$ and $\tilde{\psi}_1^{(1)} = (a_1(y) + ib_1(y))e^{-iz}$. The strain-rate tensor, $\boldsymbol{\gamma}_1 = \boldsymbol{\nabla}\mathbf{u}_1 + \boldsymbol{\nabla}\mathbf{u}_1^{\mathrm{T}}$, can then be obtained using (7.7). Exploiting (7.3), we see that the first-order stress tensor is given by

$$\boldsymbol{\tau}_1 = \mathrm{Re}\left[\tilde{\dot{\boldsymbol{\gamma}}}_1^{(0)} + \frac{1 + i\mathrm{De}_2}{1 + i\mathrm{De}_1}\tilde{\dot{\boldsymbol{\gamma}}}_1^{(1)}\right]. \tag{7.11}$$

If $\boldsymbol{\sigma} = -p\mathbf{I} + \boldsymbol{\tau}$ refers to the total stress tensor, integration of $\boldsymbol{\nabla} \cdot \boldsymbol{\sigma} = 0$ leads to the sum of the forces, $\mathbf{f}$, on the upper and lower sheets (over a period) equal to zero, *i.e.* $\mathbf{f}|_{y=y_1} + \mathbf{f}|_{y=y_2} = 0$. At leading order, the horizontal component of this relationship is

$$\int_0^{2\pi} \tau_{1xy}|_{y=0}\mathrm{d}x = \int_0^{2\pi} \tau_{1xy}|_{y=h}\mathrm{d}x, \tag{7.12}$$

which yields $\mathrm{C}_1 = 0$. We finally determine the relative velocity by insisting the sheets be force-free. Typically, for each sheet, one must sum the forces on both the inner and outer surfaces. However, the outer problem is force-free for all $U_{\Delta 1}$ [59]. The net force on the upper sheet is therefore given by

$$F_{1x} = -\int_0^{2\pi} a_0''(h)\mathrm{d}x = -2\pi U_{\Delta 1}/h, \tag{7.13}$$

and hence $U_{\Delta 1}$ is zero, which is expected due to the $\epsilon \to -\epsilon$ symmetry of the system. With C_1 and $U_{\Delta 1}$ equal to zero then $a_0 = 0$ (see (7.8)) therefore we have no time-averaged flow and we get a simplified relation between stress and strain-rate in Fourier space as

$$\tilde{\boldsymbol{\tau}}_1 = \frac{1 + i\mathrm{De}_2}{1 + i\mathrm{De}_1}\tilde{\dot{\boldsymbol{\gamma}}}_1. \tag{7.14}$$

7.3.2 Second-order solution

The second-order component of (6.3) is given by

$$\left(1 + \mathrm{De}_1\frac{\partial}{\partial t}\right)\boldsymbol{\tau}_2 - \left(1 + \mathrm{De}_2\frac{\partial}{\partial t}\right)\boldsymbol{\gamma}_2 = \mathrm{De}_1\left(\boldsymbol{\nabla}\mathbf{u}_1^{\mathrm{T}} \cdot \boldsymbol{\tau}_1 + \boldsymbol{\tau}_1 \cdot \boldsymbol{\nabla}\mathbf{u}_1 - \mathbf{u}_1 \cdot \boldsymbol{\nabla}\boldsymbol{\tau}\right) - \mathrm{De}_2\left(\boldsymbol{\nabla}\mathbf{u}_1^{\mathrm{T}} \cdot \boldsymbol{\gamma}_1 + \boldsymbol{\gamma}_1 \cdot \boldsymbol{\nabla}\mathbf{u}_1 - \mathbf{u}_1 \cdot \boldsymbol{\nabla}\boldsymbol{\gamma}_1\right). \tag{7.15}$$

The only part of the streamfunction, ψ_2, that will contribute to the force on the sheets at second order is its mean value in x. Using (7.14), the mean value of (7.15) is given by

$$\langle \boldsymbol{\tau}_2 \rangle - \langle \boldsymbol{\gamma}_2 \rangle = \mathrm{Re}\left[\frac{\mathrm{De}_1 - \mathrm{De}_2}{2(1+i\mathrm{De}_1)} \left(\boldsymbol{\nabla} \tilde{\mathbf{u}}_1^{\mathrm{T}*} \cdot \tilde{\dot{\boldsymbol{\gamma}}}_1 + \tilde{\dot{\boldsymbol{\gamma}}}_1 \cdot \boldsymbol{\nabla} \tilde{\mathbf{u}}_1^{*} - \tilde{\mathbf{u}}_1^{*} \cdot \boldsymbol{\nabla} \tilde{\dot{\boldsymbol{\gamma}}}_1 \right) \right], \tag{7.16}$$

where *'s indicate complex conjugates, and $\langle ... \rangle$ denotes averaging over one period in x. The right hand side of (7.16) can then be computed using the first-order streamfunction. Upon taking the divergence and the curl of (7.16), we obtain

$$\nabla^4 \langle \psi_2 \rangle = \frac{\mathrm{De}_1 - \mathrm{De}_2}{1 + \mathrm{De}_1^2} \frac{\mathrm{d}^2}{\mathrm{d}y^2} G(y; h, \phi), \tag{7.17}$$

where

$$\begin{aligned} G(y;h,\phi) = \frac{1}{2}\Big[&- a_1'(y)\Big(\mathrm{De}_1 a_1''(y) + 3b_1''(y)\Big) + b_1'(y)\Big(3a_1''(y) - \mathrm{De}_1 b_1''(y)\Big) \\ &+ a_1(y)\Big(- 2b_1'(y) - \mathrm{De}_1 a_1'''(y) + b_1'''(y)\Big) \\ &+ b_1(y)\Big(2a_1'(y) - a_1'''(y) - \mathrm{De}_1 b_1'''(y)\Big)\Big]. \end{aligned} \tag{7.18}$$

The second-order components of the boundary conditions are

$$\boldsymbol{\nabla}\psi_2|_{y=0} = -\boldsymbol{\nabla}(U_{\Delta 2} y) - \sin(z - \phi/2)\boldsymbol{\nabla}\left(\frac{\partial \psi_1}{\partial y}\right)\Big|_{y=0}, \tag{7.19}$$

$$\boldsymbol{\nabla}\psi_2|_{y=h} = \boldsymbol{\nabla}(U_{\Delta 2} y) - \sin(z + \phi/2)\boldsymbol{\nabla}\left(\frac{\partial \psi_1}{\partial y}\right)\Big|_{y=h}. \tag{7.20}$$

Taking the mean value of (7.19) and (7.20) yields

$$\frac{\partial \langle \psi_2 \rangle}{\partial x}\Big|_{y=0} = 0, \tag{7.21}$$

$$\frac{\partial \langle \psi_2 \rangle}{\partial y}\Big|_{y=0} = \frac{1}{2}\left[-U_{\Delta 2} + \frac{\cos^2(\frac{\phi}{2})(-h + \sinh h)}{h + \sinh h} + \frac{\sin^2(\frac{\phi}{2})(h + \sinh h)}{-h + \sinh h} \right], \tag{7.22}$$

$$\frac{\partial \langle \psi_2 \rangle}{\partial x}\Big|_{y=h} = 0, \tag{7.23}$$

$$\frac{\partial \langle \psi_2 \rangle}{\partial y}\Big|_{y=h} = \frac{1}{2}\left[U_{\Delta 2} + \frac{\cos^2(\frac{\phi}{2})(-h + \sinh h)}{h + \sinh h} + \frac{\sin^2(\frac{\phi}{2})(h + \sinh h)}{-h + \sinh h} \right]. \tag{7.24}$$

Solving (7.17) with the above boundary conditions leads to the solution

$$\langle\psi_2\rangle = \mathrm{C}_2 y^2\left(y-\frac{3h}{2}\right)+\frac{U_{\Delta 2}y(y-h)}{2h}+\frac{y(\sinh h-h)\cos^2\frac{\phi}{2}}{2(h+\sinh h)}+\frac{y(\sinh h+h)\sin^2\frac{\phi}{2}}{2(-h+\sinh h)} + \frac{\mathrm{De}_1-\mathrm{De}_2}{1+\mathrm{De}_1^2}\left[\frac{y(y-2h)}{2h}\int G dy|_{y=0}-\frac{y^2}{2h}\int G dy|_{y=h}+\int\int G dy^2\right]. \tag{7.25}$$

To find the unknown constant C_2 we again turn to dynamical considerations. Using integration by parts, it is straightforward to get that the force on the bottom sheet, to $O(\epsilon^2)$, is given by

$$F_{2x} = \int_0^{2\pi}\langle\tau_{2xy}\rangle|_{y=0}\mathrm{d}x, \tag{7.26}$$

and only the mean component of the second-order stress, $\langle\tau_{2xy}\rangle$, contributes to the net force. A similar relationship holds for the force on the upper sheet. We then proceed by obtaining $\langle\tau_{2xy}\rangle$ from (7.16), where $\langle\dot{\boldsymbol{\gamma}}_2\rangle = \boldsymbol{\nabla}\langle\mathbf{u}_2\rangle + \boldsymbol{\nabla}\langle\mathbf{u}_2\rangle^{\mathrm{T}}$ and $\langle\mathbf{u}_2\rangle = [\partial\langle\psi_2\rangle/\partial y, -\partial\langle\psi_2\rangle/\partial x]^{\mathrm{T}}$. Exploiting that $\mathbf{f}|_{y=y_1} = -\mathbf{f}|_{y=y_2}$ we obtain $\mathrm{C}_2 = 0$, and the net force on the upper sheet is finally given by

$$F_{2x} = -\frac{2\pi U_{\Delta 2}}{h}+4\pi\left(\frac{\mathrm{De}_1-\mathrm{De}_2}{1+\mathrm{De}_1^2}\right)A(h)\sin\phi, \quad A(h)=\frac{h\cosh h+\sinh h}{\cosh(2h)-2h^2-1}. \tag{7.27}$$

7.4 Results

7.4.1 Synchronization

It is insightful first to consider the nature of the force which arises if the sheets are not permitted to move relative to each other but instead held with a fixed phase difference. If $U_{\Delta 2} = 0$, then the force in (7.27) is zero for $\phi = 0, \pm\pi$. The function $A(h)$, governing the variation in the force amplitude with mean distance h, is positive definite and decays exponentially with h, while becoming unbounded near $h = 0$ (see Fig. 7.2a). Since $\mathrm{De}_1 > \mathrm{De}_2$, we see that the force $F_{2x} \propto \sin\phi$. This indicates that $\phi = 0$ is a stable fixed point while $\phi = \pm\pi$ are unstable, and therefore we expect in-phase synchronization to occur.

We next observe that we obtain here a nonzero force on sheets with front/back symmetric waveforms. In the case of a Newtonian fluid, this is forbidden because of kinematic reversibility, and the force is identically zero unless the front/back symmetry is broken [25, 68]. The other symmetry, with respect to the x-axis, is always assumed to be true in order to enforce swimming along a straight line. Indeed, in a Newtonian fluid, for any system with both vertical and horizontal symmetry one can reflect about both axes of symmetry then reverse the kinematics to obtain an identical conformation with the opposite force necessitating $F_x = 0$ (our calculations confirm this by setting $\mathrm{De}_1 = \mathrm{De}_2 = 0$ in 7.27). In a viscoelastic fluid, time is no longer merely a parameter, and therefore the flow is no longer kinematically reversible, thereby permitting a nonzero force.

If instead of holding the sheets fixed, we let them move, we then have to enforce the force-free condition, and thus we obtain the relative speed $U_{\Delta 2} = hF^s_{2x}/2\pi$, where F^s_{2x} is the static force incurred when $U_{\Delta 2} = 0$ in (7.27). The remarkable result is that, since the force occurs in a viscoelastic fluid at second order in the wave amplitude, the phase will evolve on a time scale varying as $t \sim \epsilon^{-2}$. In a Newtonian fluid, was shown that the force is always zero to second order in ϵ, for any shape, and first appears at fourth order for shapes with broken front-back symmetry [68]. This means that in a Newtonian fluid, at best, the phase will evolve to a phase-locked configuration on a time scale varying as $t \sim \epsilon^{-4}$. In complex fluids, synchronization is therefore seen to take place on asymptotically faster time scales than in a Newtonian fluid.

We now solve analytically for the time-evolution of the phase. Since to leading order $\dot{\phi} = -\epsilon^2 U_{\Delta 2}$, we obtain a differential equation for the evolution for ϕ as

$$\frac{d\phi}{dt} = -\epsilon^2 2h \left(\frac{\mathrm{De}_1 - \mathrm{De}_2}{1 + \mathrm{De}_1^2} \right) A(h) \sin\phi, \tag{7.28}$$

which, for constant h, can be integrated to yield an analytical formula for the phase as

$$\phi(t) = 2\tan^{-1}\left\{ \tan\left(\frac{\phi_0}{2}\right) \exp\left[-\epsilon^2 2hA(h) \left(\frac{\mathrm{De}_1 - \mathrm{De}_2}{1 + \mathrm{De}_1^2} \right) t \right] \right\}. \tag{7.29}$$

Given that $\mathrm{De}_1 > \mathrm{De}_2$, we see that $\phi \sim \pm e^{-t}$ near the $\phi = 0$ fixed point, meaning

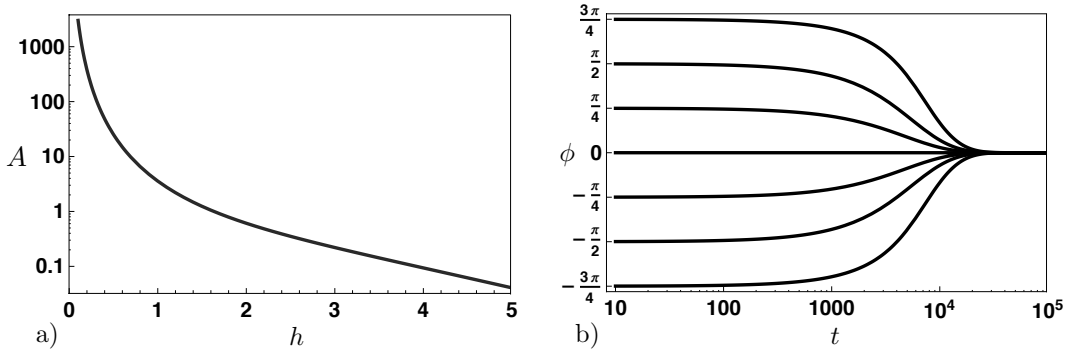

Figure 7.2: a) Amplitude A of the phase-locking force decays exponentially with the separation distance, h (7.27). b) Time-evolution of the phase angle $\phi(t)$ from various initial conditions towards the stable in-phase conformation ((7.29) with $\epsilon = 0.1$, $h = 2$, $\mathrm{De}_1 = 100$ and $\mathrm{De}_2 = 10$).

it is stable; however, near the $\phi = \pm\pi$ fixed points, $\phi \mp \pi \sim \mp e^t$ meaning they are unstable and hence the phase converges to $\phi = 0$ for all initial conditions. The time-evolution of the phase from various initial positions, assuming a constant separation between the sheets of $h = 2$, is plotted in Fig. 7.2b with $\mathrm{De}_1 = 100$, $\mathrm{De}_2 = 10$ and $\epsilon = 0.1$. All initial conformations evolve to stable in-phase synchrony. In the Newtonian case, the stability of the in-phase versus opposite-phase conformation is purely a matter of geometry, regardless of considerations of energy dissipation, and in fact two swimmers can evolve to a stable conformation which maximizes the energy dissipated [25, 68]. In contrast, in a viscoelastic fluid we find that with no asymmetry the system naturally evolves to an in-phase conformation which, as we show below, coincides with the conformation of minimal viscous dissipation.

7.4.2 Energy dissipation

The energy dissipated in the fluid between two sheets is given by integrating the dissipation density, $\boldsymbol{\tau} : \boldsymbol{\gamma}$, over the volume. The leading order component is given by

$$\boldsymbol{\tau}_1 : \boldsymbol{\gamma}_1 = \mathrm{Re}\left[\tilde{\boldsymbol{\tau}}_1\right] : \mathrm{Re}\left[\tilde{\dot{\boldsymbol{\gamma}}}_1\right] = \frac{1 + \mathrm{De}_1\mathrm{De}_2}{1 + \mathrm{De}_1^2}\boldsymbol{\gamma}_1 : \boldsymbol{\gamma}_1 - \frac{1}{2}\frac{\mathrm{De}_1 - \mathrm{De}_2}{1 + \mathrm{De}_1^2}\Im\left[\tilde{\dot{\boldsymbol{\gamma}}}_1 : \tilde{\dot{\boldsymbol{\gamma}}}_1\right], \tag{7.30}$$

where $\Im[...]$ denotes the imaginary part. The second term in (7.30) integrates to zero over a period, thus, to leading order, the energy dissipation rate per unit depth over one period is given by

$$\dot{E} = \epsilon^2 \frac{1 + \mathrm{De}_1 \mathrm{De}_2}{1 + \mathrm{De}_1^2} \int_0^{2\pi} \int_{y_1}^{y_2} \boldsymbol{\gamma}_1 : \boldsymbol{\gamma}_1 \mathrm{d}x\mathrm{d}y. \tag{7.31}$$

The result of (7.31) is merely a scalar multiple of the Newtonian dissipation calculated by [13], which is minimum at the in-phase conformation, and maximum in the case of opposite-phase (and decays to zero as $h \to 0$). We see therefore that in a viscoelastic fluid the system is driven towards a state of minimum energy dissipation.

7.4.3 Vertical force

Since the evolution of the phase depends on the separation distance h, it is informative to analyze the magnitude of vertical forces between the sheets. We now proceed to compute the vertical force from the inner problem with the first and second-order streamfunctions derived here, and we use the solutions of the outer flow problem from the literature [59]. The vertical force on the bottom sheet to first order is given by

$$F_{1y} = \int_0^{2\pi} \left(\sigma_{1_{22}}|_{y=0} - \sigma^{\mathrm{outer}}_{1_{22}}|_{y=0} \right) \mathrm{d}x. \tag{7.32}$$

Both components are individually zero, hence the force is zero. At second order, the outer flow yields no force for all $U_{\Delta 2}$, therefore the force on the bottom sheet is given by

$$\begin{aligned} F_{2y} &= \int_0^{2\pi} \left[\langle \tau_{2yy} \rangle - \int \frac{\partial \langle \tau_{2yy} \rangle}{\partial y} dy \right] \Big|_{y=0} \mathrm{d}x \\ &= 2\pi \left(\frac{\mathrm{De}_1 - \mathrm{De}_2}{1 + \mathrm{De}_1^2} \right) \Big[\mathrm{B}_1(h) + \mathrm{B}_2(h) \cos\phi \Big], \end{aligned} \tag{7.33}$$

where

$$\mathrm{B}_1(h) = \frac{2\left[1 - (1 + 2h^2)\cosh(2h) - 2h\sinh(2h)\right]}{\left(\cosh(2h) - 1 - 2h^2\right)^2}, \tag{7.34}$$

$$\mathrm{B}_2(h) = \frac{(4h^2 - 1)\cosh h + \cosh(3h) + 2h\left[3 + 2h^2 + \cosh(2h)\right]\sinh h}{\left(\cosh(2h) - 2h^2 - 1\right)^2} \tag{7.35}$$

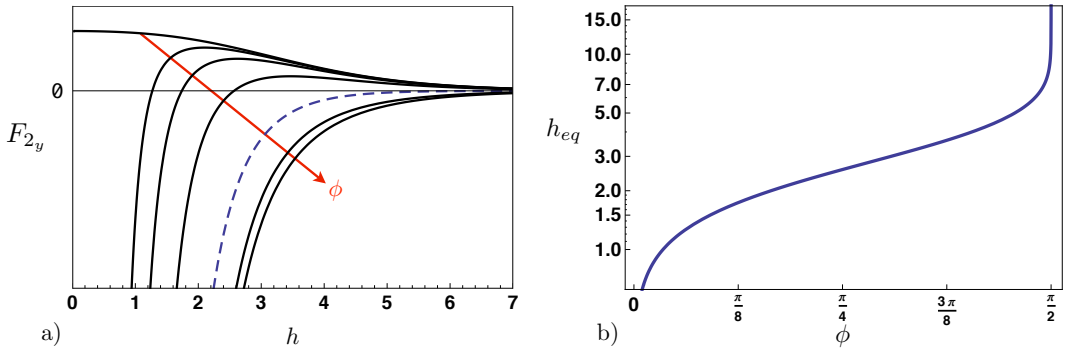

Figure 7.3: a) The leading-order vertical force on the lower sheet, $F_{2y}(h)$, displays a complex behavior which depends on both phase difference ϕ and mean separation h. Plotted for $\phi = \{0, \pi/16, \pi/8, \pi/4, \pi/2 \text{ (shown dashed)}, 3\pi/4, \pi\}$ (arbitrary units). b) Equilibrium separation, h_{eq}, defined as the distance at which the vertical force is zero for a given ϕ.

The vertical component of the force is a cosine function in ϕ which is amplified by the positive-definite function B_2 and shifted by the negative-definite function B_1. Both functions become unbounded as $h \to 0$, and both tend asymptotically to zero as $h \to \infty$. In Fig. 7.3a we plot the vertical force as a function of the distance between the sheets, h, for various ϕ (arbitrary units). If the phase difference is above $\pi/2$ ($\phi = \pi/2$ is shown dashed), then the sheets will be repelled from each other. However, as the sheets get closer in phase there arises a finite equilibrium separation, $h_{eq}(\phi)$, where $F_{2y} = 0$. If the sheets are separated by $h < h_{eq}$, they will be repelled while if $h > h_{eq}$, they will be attracted. In Fig. 7.3b we plot h_{eq} as a function of phase difference and we see that the equilibrium separation decreases monotonically with decreasing ϕ and that when the sheets are in phase the vertical force acting on them is strictly attractive. Indeed, for $\phi = 0$, in the limit $h \to 0$ we see that $F_{2y} = (3\pi/4)(\mathrm{De}_1 - \mathrm{De}_2)/(1 + \mathrm{De}_1^2)$. Note h is allowed to approach zero only when $\phi = 0$, as otherwise the sheets would overlap.

7.4.4 Coupled dynamics

In the idealized two-dimensional case studied here, the swimmer mobility in the vertical direction is strictly zero and hence only motion in the horizontal direction occurs. In the slender-body limit, which is the one relevant for the

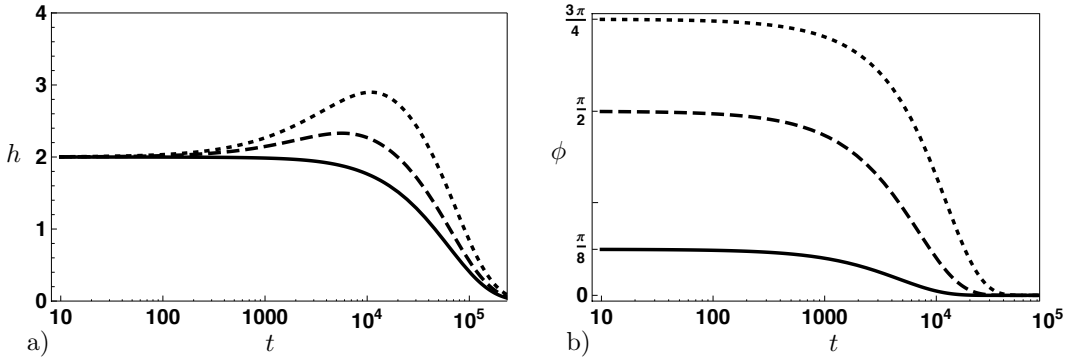

Figure 7.4: Coupled time evolution of the distance between the swimmers, $h(t)$ (a), and the phase difference, $\phi(t)$ (b). The initial condition is $h_0 = 2$, and the mobility in y is taken to be half of that in x: $\phi_0 = 3\pi/4$ (dotted line), $\phi_0 = \pi/2$ (dashed line), $\phi_0 = \pi/8$ (solid line). Here $\epsilon = 0.1$, $\mathrm{De}_1 = 100$ and $\mathrm{De}_2 = 10$.

dynamics of three-dimensional flagellar filaments of swimming cells, the viscous mobility in the direction perpendicular to the length of the flagellum is about half of that in the parallel direction [83]. In order to propose a simple model for the coupled vertical/horizontal motion of the sheets, we proceed to use this ratio in our model, and simply assume

$$\frac{dh}{dt} = -\frac{\epsilon^2 h}{4\pi} F^s_{2y}. \tag{7.36}$$

Given the behavior of the vertical force, we expect the swimmers to be pushed apart slightly if their phase difference is large, then, as the phase difference decreases, to be attracted to a final synchronized conformation where the flagella are as close together as possible, as seen experimentally [4]. We can numerically integrate both differential equations, (7.28) and (7.36), to obtain the coupled time evolution of $h(t)$, shown in Fig. 7.4a, and $\phi(t)$, shown in Fig. 7.4b, for an initial separation $h_0 = 2$. We see that for a small enough initial angle, the sheets are monotonically attracted to each-other ($\phi_0 = \pi/8$, solid line). However, for larger initial phase differences, the sheets are initially repelled, before reaching a maximum separation, and eventually being drawn together closely. This is illustrated for $\phi_0 = \pi/2$ (dashed line) and $\phi_0 = 3\pi/4$ (dotted line). The time scale for the evolution of the phase angle is similar to the constant separation case, and all initial conformations converge to the stable in-phase conformation.

7.5 Conclusion

In this chapter we used a two-dimensional model to address analytically the synchronization of two swimmers in a viscoelastic (Oldroyd-B) fluid. In Newtonian fluids, a front-back asymmetry in the swimmer's waveform is required for synchronization. In contrast, in a viscoelastic fluid, phase-locking occurs even for swimmers displaying front/back symmetry. The two swimmers are driven into a stable in-phase conformation where a minimum of mechanical energy is dissipated, contrary to the Newtonian case where the stable conformation can be either in-phase or opposite-phase depending only on the waveform geometry. In addition, the evolution to a phase-locked conformation in a viscoelastic fluid occurs on asymptotically faster time scales than in a Newtonian fluid.

From a biological standpoint, the results of our model indicate that, for example, mammalian spermatozoa progressing through cervical mucus would be expected to synchronize passively, thereby reducing the work they are doing against the surrounding fluid as compared to when swimming isolated. This net energy savings could then potentially be used to increase their wave speeds, and hence swimming speed, as is observed experimentally [4]. The asymptotically larger forces between swimmers might also lead to large-scale coherence in the dynamics of cell suspensions which is more pronounced in complex fluids than in Newtonian environments.

Chapter 7, in part, is a reprint of the material as it appears in the Journal of Fluid Mechanics 2010. Elfring, Gwynn J.; Pak, On Shun; Lauga, Eric, Cambridge University Press, 2010. The dissertation author was the primary investigator and author of this paper.

Chapter 8

Buckling instability of squeezed droplets

8.1 Introduction

The interaction between liquids and solids is ubiquitous in our daily life, from droplets on a windshield to ink in our printers [84]. Capillary phenomena arise as a consequence of intermolecular forces and manifest themselves on large scales by the tendency of liquids to minimize their surface area [85]. The theory for the shapes of droplets was proposed over two hundred years ago by Young [86] and Laplace [87], and since that time much has been learned on the wetting of solids by liquids [88, 89]. Of interest to us in this chapter is why certain droplet configurations may be unstable. Plateau observed that a liquid jet would ultimately break up into droplets because the energy of the initial cylindrical shape is lowered by long wavelength perturbations [90]. The dynamics of this instability was later elucidated by Lord Rayleigh [91] while more recent work has explored the finite-time singularity at the break-up [92].

A somewhat lesser known observation made by Plateau, in the same work [90], details how a droplet suspended between two equal circular disks (a so-called liquid bridge) loses axisymmetry when sufficiently compressed. Plateau [90] observed that the onset of this shape instability occurs when the profile of the droplet

at the point of contact with the pinned surface becomes tangent to the disks, hence making for an apparent droplet contact angle of π (see also the review in Ref. [93]). An analytical solution for the shape of a liquid bridge was put forward by Howe [94] along with an initial analysis of the instability [94, 95]. It was later shown formally that if the axisymmetric droplet shape is described in polar coordinates by a single valued radius function then it is always stable to asymmetric perturbations for pinned boundary conditions [96]. Such a single-valued description breaks down when the droplet becomes tangent to the disks. Russo and Steen showed then that past this point the droplet is unstable to asymmetric perturbations [97].

Subsequent works [98, 99, 100, 101] further elucidated the space of stability of these liquid bridges for which the results of Plateau is only one of many. In particular, it was similarly shown that a pinned droplet deformed by a gravitational field, rather than by compression from an upper surface, will also transition to an asymmetric shape past the point when the droplet profile is tangent to the pinning line at the point of contact[93]. A related shape instability arises when two free-surfaces are squeezed together [102]. If two droplets, or bubbles [103, 104], are brought into contact, then initially the interface separating them is perpendicular to the direction of compression and their shapes deform in an axisymmetric fashion. Past a critical conformation the separating interface rotates and the droplets, or bubbles, lose axisymmetry. A general framework for the stability of equilibrium states of capillary phenomena is provided in the text by Myshkis et al. [105].

In recent experiments by Nagy and Neitzel, droplets pinned to a bottom surface and compressed by a perfectly non-wetting surface from above have been shown to develop a geometric asymmetry at a critical deformation [106]. Experimentally, the perfectly non-wetting condition on the top surface is obtained using a thin layer of air maintained by thermocapillary convection between the cold surface (of arbitrary contact angle) and the hot droplet, leading to an effective contact angle of 180° [107, 108]. On the bottom surface, pinned boundary conditions are achieved by extruding liquid through a capillary, but one can also imagine a droplet confined to the top of a small post or a disk. When the droplet is compressed by displacing the top surface, below a threshold the droplet maintains axisymmetry,

a) 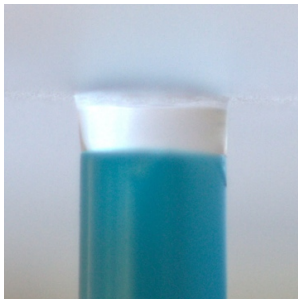 b) 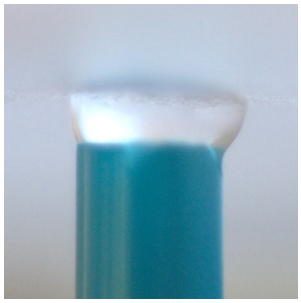 c) 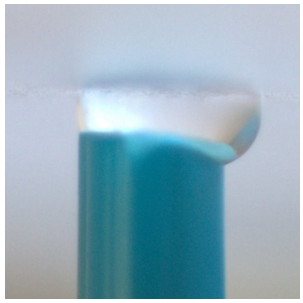

Figure 8.1: Images of a water droplet at the tip of a straw compressed against a hydrophobic surface; (a): The droplet after initial contact, with pinned boundary conditions at the bottom and a fixed hydrophobic contact angle at the top; (b): Axisymmetric deformation of the droplet prior to the onset of shape instability; (c) Asymmetric bulge-like shape of the droplet after the critical compression.

but upon reaching a critical conformation, the droplet bulges to one side indicating a shape instability. Subsequent Surface Evolver [109] simulations of the same setup verified the geometric asymmetry [106].

In this chapter we show that the shape instability observed by Nagy and Neitzel [106] arises with the same geometrical criterion as that of the Plateau liquid bridge, namely when the droplet surface becomes tangent to the pinned surface at the point of contact (apparent contact angle of π). We demonstrate that this instability criterion does not depend on the droplet contact angle on the upper surface. We reveal, however, that that the geometric instability criterion no longer holds when the deforming surface is not flat, as is illustrated with a compression of the droplet by a conical surface. We first use a simple table-top experimental example to show that the shape instability occurs even if the deforming surface is not perfectly non-wetting. We then employ a two-dimensional analysis to provide a preliminary analytical approach to the instability, and derive the stability criterion and its independence on the top contact angle. We next carry out a three-dimensional perturbation energetic analysis confirming the two-dimensional theory, and demonstrating the breakdown of the geometric stability criterion when the deforming surface is no longer flat. We finally utilize numerical computations using Surface Evolver to confirm our theoretical predictions.

8.2 Table-top experiments

We first performed simple table-top experiments in an effort to observe whether the shape instability occurs in the case where the compressing surface is not perfectly non-wetting. The results are shown in Fig. 8.1. We use a plastic straw extruding water, coated with hydrophobic spray to delay its wetting prior to the shape instability. The water droplet is put in contact with a slightly hydrophobic surface. In Fig. 8.1 we see that initially the droplet is symmetric (a), and remains symmetric under small deformations (b). When the droplet has been sufficiently squeezed, it rapidly develops a pronounced geometric asymmetry (c).

8.3 Energetic analysis

Consider a droplet pinned along one surface, which we will call the bottom surface with a constant circular area. The droplet has an volume V which remains constant by conservation of mass. We assume that the droplet is smaller than the capillary length and hence ignore gravity [84]. The droplet shape is the one which minimizes the functional

$$\mathcal{E} = \int_S \gamma dS - \int_V p dV, \tag{8.1}$$

where γ is the interfacial tension coefficient which is integrated over all interfaces S and the pressure p is a Lagrange multiplier enforcing mass conservation. We further assume that the droplet is in contact with a second surface, parallel to the bottom surface, and which we will refer to as the top surface. That surface, of area W, does not pin the drop but instead the droplet contact line is free to move along the top surface with the set contact angle θ. We ignore effects arising from contact angle hysteresis. In that case the relevant surface energy now becomes

$$E = \gamma_{sv}(W - S_{sl}) + \gamma_{sl}S_{sl} + S_{lv}\gamma_{lv} + const., \tag{8.2}$$

where the subscripts sv, sl and lv indicate the solid-vapor, solid-liquid and liquid-vapor interfaces respectively. The surface energy of the pinned interface is unchanging and thus rolled into the constant term. Using Young's equation for the

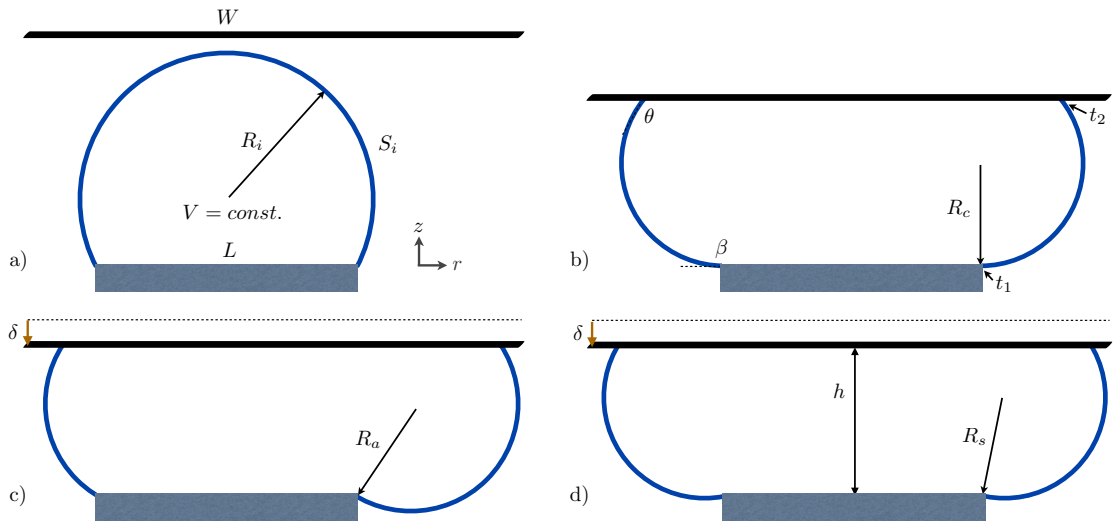

Figure 8.2: Schematic representation of the droplet in various stages of deformation, for a contact angle $\theta = 2\pi/3$. (a): No deformation; (b): Droplet at the critical conformation, $R = R_c$; (c): Asymmetric droplet post threshold $R = R_a$ ($\delta > 0$); (d): Symmetric droplet post threshold $R = R_s$ ($\delta > 0$). The droplet volume (termed A in 2D, V in 3D) remains constant; the initial radius R_i and surface area S_i are thus set by the value of the droplet volume.

equilibrium contact angle θ on the top surface [84], Eq. (8.2) may then be recast as

$$E = \gamma_{lv} \left(S_{lv} - S_{sl} \cos\theta \right) + \gamma_{sv} W + const. \tag{8.3}$$

Given that W is constant, we see that finding an equilibrium is tantamount to minimizing the projected surface $S = S_{lv} - S_{sl} \cos\theta$. Note that when the solid surface is nonwetting, $\theta = \pi$, and one has thus to minimize $S = S_{sl} + S_{lv}$. From this point on we neglect the constant terms in Eq. (8.3), and drop the lv subscript for the liquid-vapor interfacial coefficient for simplicity. Hence we write $E = \gamma S$.

8.3.1 Two-dimensional analysis

Flat surface

In order to get a sense of the essential physics of the droplet instability we first illustrate the process in two dimensions. The geometric criterion for the

instability of symmetric solutions is easier to derive and visualize than in three-dimensions, which is a calculation we will address in the next section.

The setup and notations are illustrated in Fig. 8.2. The volume of the droplet is denoted V in three dimensions and A in two dimensions, and the interfaces are denoted S in both cases. The liquid-vapor interface which minimizes the total interfacial energy is a surface of constant mean curvature, and thus in $2D$ it is circular. We therefore write the shape of the liquid-vapor interface, parameterized by t in the $\{r,z\}$ plane, as

$$\begin{aligned} r(t) &= r_0 + R\cos(t), \\ z(t) &= z_0 + R\sin(t), \end{aligned} \tag{8.4}$$

where R is the radius of curvature of the 2D droplet originating from the center (r_0, z_0), and t is the polar angle about that point measured positive counterclockwise from the point where the droplet is locally parallel to the z axis on the right-hand side. The contact point where the droplet is pinned occurs at $t = t_1$, and the point of contact with the wall W occurs at $t = t_2$. We define $\Delta t = t_2 - t_1$ so that the surface area of the liquid-vapor portion of the droplet is $S_{lv} = 2R\Delta t$. The contact area with the bottom surface is assumed to be of length $L = 2r_1$. We subsequently employ the subscript 1 or 2 on any function of t to denote the function evaluated at t_1 or t_2 respectively. With this in mind, the height between the two surfaces (clearance) is given by $h = z_2 - z_1$. We use θ to denote the equilibrium contact angle of the droplet on the top surface, and β the apparent contact angle with the bottom, horizontal, surface (where the contact line is pinned).

When the top surface is not in contact with the droplet, as in Fig. 8.2a, then t_2 is taken to lie on the axis of symmetry of the undeformed droplet ($t_2 = \pi/2$). The initial droplet volume, which remains constant, is $A = (R_i^2/2)(2\Delta t + \sin[2\pi - 2\Delta t])$, and the pinning length $L^2 = 4R_i^2(1 - \sin^2[(\pi - 2\Delta t)/2])$ closes the system. The droplet will form a half circle when $L = 4\sqrt{A/2\pi}$.

When there is contact with the wall, the droplet takes the shape illustrated in Fig. 8.2b, and two 'disconnected' liquid-vapor surfaces are present. In order to maintain mechanical equilibrium these two surfaces must have an identical radius of curvature, R. The point t_2 is located where the droplet is in contact with the

surface, and therefore we necessarily have $t_2 = \theta - \pi/2$. If the apparent contact angle at the pinned line, β, satisfies $\beta \leq \pi$, in other words $t_1 \geq -\pi/2$, we will show below that the only solution for the two-dimensional droplet is left-right symmetric (the details below will demonstrate that there exists no asymmetric solution).

At the critical point (denoted with a subscript c), which is depicted in Fig. 8.2b, we have $t_1 = t_1^c = -\pi/2$ and $\Delta t = \theta$. The total surface energy is then given by $E_c/\gamma = (2\Theta R_c - L\cos\theta)$, where $\Theta \equiv \theta - \cos\theta\sin\theta$. Here the radius R_c is given by conservation of volume, $A = \Theta R_c^2 + LR_c(1-\cos\theta)$; this quadratic equation for R_c can be solved to obtain the critical radius for a given initial droplet volume, pinning length and contact angle. The critical gap height, $h^c = z_2 - z_1^c = R_c(1-\cos\theta)$, increases monotonically with the contact angle (which ranges from zero to $\theta = \pi$).

If we now reduce the gap height by some amount δ, so that $h = h^c - \delta$, two possibilities exist for the droplet shape, either asymmetric (Fig. 8.2c) or symmetric (Fig. 8.2d). In each case the left and right sides of the droplet need to have the same radius of curvature to ensure mechanical stability. From this point on all lengths will be non-dimensionalized by the critical radius R_c, and hence $R_c = 1$.

In the asymmetric case, denoted by the subscript a, one of the circular ends moves in and the other moves out (see Fig. 8.2c). The droplet volume in this instance is $A = \Theta R_a^2 + hL$, meaning that $R_a^2 = 1 + L\delta/\Theta$. If we take $\delta < 0$ we see that $R_a < 1$ which is impossible as the droplet would not span the required length h, hence there can be no asymmetric shape for $\delta < 0$. Further, we see that for $\delta > 0$, $R_a > 1$. The relevant surface energy is given by $E_a/\gamma = 2\Theta R_a - L\cos\theta$ in that case.

Alternatively, the droplet may remain symmetric (subscript s) past the critical point, as shown in Fig. 8.2d. Conservation of volume leads to $A = R_s^2[\Theta - \pi/2 - t_1 + \cos t_1(\sin t_1 - 2\cos\theta)] + hL$, where we set the gap height to be $h = 1 - \cos\theta - \delta$, and hence $t_1 = -\sin^{-1}[\cos\theta + h/R_s]$. Note that when in contact with hydrophilic surfaces, $\theta < \pi/2$, droplets undergo a inversion of the concavity of the liquid-vapor interface for larger negative values of δ where this geometry no longer holds. The relevant surface energy is now give by $E_s/\gamma = 2(\Theta - t_1 -$

$\pi/2)R_s - (L - 2R_s\cos t_1)\cos\theta$.

The symmetric and asymmetric cases are the only two possible mechanically stable solutions. The one which appears in equilibrium is the one which minimizes surface energy. Solving for R_s and E_s, can in general only be done numerically. However, the difference in the surface energies between the symmetric and asymmetric configurations, $\Delta E = E_s - E_a$, may be formally bounded as follows

$$\frac{\Delta E}{2\gamma R_s} = \Theta + \lambda - \sqrt{\Theta^2 + \Theta(\lambda + \Gamma)} \geq 0, \tag{8.5}$$

where $\Theta \equiv \theta - \sin\theta\cos\theta$, $\lambda = \alpha - \sin\alpha\cos\theta$ and $\Gamma = (\cos\alpha - \cos\theta)\sin\alpha$ and while $\theta \in [0, \pi]$ and $\alpha = -(t_1^s + \pi/2) \in [0, \theta]$ (the superscript s indicates the symmetric contact point). We see that evidently $\Theta \geq 0$ and $\lambda \geq 0$ as $\theta \geq \sin\theta$. Rearranging we obtain

$$\lambda - \Gamma \geq -\frac{\lambda^2}{\Theta}. \tag{8.6}$$

Substituting back, we find

$$\alpha - \sin\alpha\cos\alpha \geq -\frac{\lambda^2}{\Theta}, \tag{8.7}$$

and since the left-hand side is non-negative the inequality is proved. The equality holds only at the critical point when $t_1^s = t_1^c = -\pi/2$, in other words when $\delta = 0$ and $R_s = 1$. We have thus proven that, past the critical point ($\delta > 0$), the asymmetric conformation is always the droplet shape which minimizes the free energy, independently of the value of the contact angle on the top surface. Droplets after this critical compression are thus expected to always display an asymmetric shape.

For small values of δ, the value of R_s can be found by hand, and provided the contact angle θ is not too small we obtain

$$R_s = 1 - \frac{1}{1 - \cos\theta}\delta + \frac{(L[1 - \cos\theta] + 2\Theta)^2}{256\sin^{10}(\theta/2)}\delta^2 + \mathcal{O}(\delta^3), \tag{8.8}$$

$$\frac{E_s}{\gamma} = 2\Theta - L\cos\theta + L\delta + \frac{L(1 - \cos\theta) + \Theta}{4\sin^4(\theta/2)}\delta^2 + \mathcal{O}(\delta^3). \tag{8.9}$$

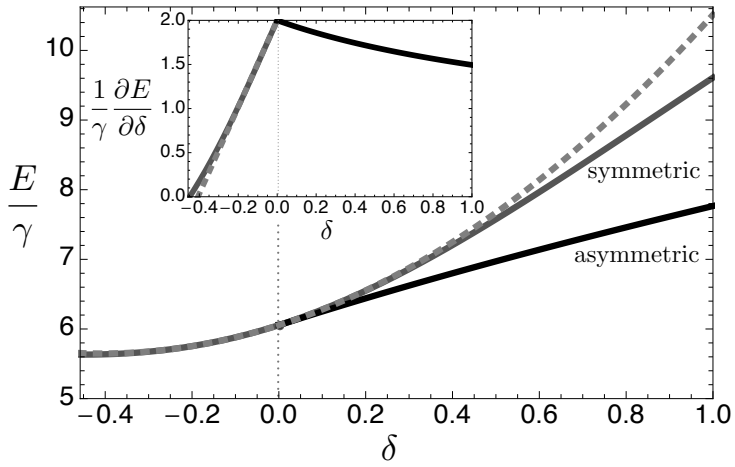

Figure 8.3: Surface energy, E, vs. change in separation, δ, with $L = 2$ and $\theta = 2\pi/3$ (two-dimensional case). The solid lines are exact solutions and the dashed line is asymptotic. The inset shows the slope of E. We see that when $\delta = 0$ (indicated by the dotted line) the surface energy bifurcates into symmetric and asymmetric conformations. The asymmetric conformation (solid black line) has lower surface energy than the asymmetric conformation (solid gray line) and hence is the energetically preferable state.

We then get

$$\frac{\Delta E}{\gamma} = \frac{\left(L[1-\cos\theta]+2\Theta\right)^2}{16\Theta\sin^4(\theta/2)}\delta^2 + \mathcal{O}(\delta^3) \geq 0. \tag{8.10}$$

Notably, the force required to deform the droplet is proportional to the spatial rate of change of the surface area hence, for $\delta > 0$ we find

$$f = \frac{\partial E}{\partial \delta} = \gamma \frac{L}{\sqrt{1+L\delta/\Theta}}. \tag{8.11}$$

This may be recast in terms of the pressure jump $f/L = \Delta p = \gamma/R_a$ which recovers the Young-Laplace equation in two dimensions. Since the radius of curvature has increased, the pressure has decreased in this configuration. The slope of the force at the critical point $df/d\delta|_{\delta=0} = -\gamma L^2/2\Theta$. As might be physically expected the pressure drop is least steep for large L and $\theta = \pi$.

The two-dimensional results are illustrated in Fig. 8.3 where we plot the surface energies, E (main plot), and the energy slope (force, inset) against the change in gap height from the critical conformation, δ (for the values $L = 2$ and $\theta = 2\pi/3$).

The surface energies increase monotonically as the droplet is progressively compressed. Beyond the transition point ($\delta = 0$) both the asymmetric conformation (black) and the symmetric conformation (gray) are geometrically permissible although the asymmetric conformation is always energetically favorable. Note that the solid gray line is obtained numerically for the symmetric conformation whereas the dashed line is the asymptotic result.

As seen above, the slope of the energy is the force required to deform the droplet. We therefore see that increasingly more force is required to compress the droplet up to the critical conformation, but that beyond the transition point the more we compress the droplet the less force is required to deform it. The non-monotonic force profile is reminiscent of the non-monotonic pressure required to inflate a balloon [110]. For squeezed droplets, that result means that the droplet will buckle at the transition point if an increasing (or constant) load is applied. Unlike the classic Euler-buckling of beams [67] which can support an increasing load after a buckling event, the buckling instability of a droplet is catastrophic, a so-called limit-point instability, as the droplet can no longer sustain the force at the point of instability and collapses. In the context of superhydrophobic surfaces in which a droplet rests on a series of posts this would be what has been referred to as the impalement transition between the Cassie and Wenzel states [89, 111]. Precisely the same behavior will be obtained in three dimensions.

Inclined surface

How different is the transition to an asymmetric shape is the upper surface is not flat? Since we do not want to embed a broken-symmetry in the top surface we insist that the top surface remains axisymmetric, the simplest example of which is a cone of slope χ – or a wedge in two dimensions. One finds that a droplet undergoes a similar symmetric to asymmetric bifurcation of possible solutions precisely at the moment when the droplet on the bottom surface (at $t = t_1$) is parallel to the upper surface, in other words, when the apparent contact angle with the bottom (pinned) surface reaches the value $\beta = \pi - \chi$. As we show below, this two-dimensional criterion is no longer indicative of the onset of the instability in three dimensions

where the critical compression becomes a more complex function of the droplet volume and contact angle. The quantitative agreement between two and three dimensions is therefore restricted to the case where the top surface is flat.

8.3.2 Three-dimensional analysis

Axisymmetric solution

In three dimensions the problem becomes more complicated due to the introduction of an second radius of curvature. Unlike the two-dimensional case, asymmetric analytical extremum are unavailable. We follow here the approach of Russo and Steen [97] by first assuming that the droplet is axisymmetric, which yields analytical solutions. We then consider small asymmetric perturbations to the axisymmetric shapes to find the configuration where the axisymmetric solution is no longer energy minimizing. Finally in Section 8.4 we use Surface Evolver[109] simulations to explore the mechanical properties of the asymmetric shapes.

The energy functional, Eq. (8.1), may be written

$$\mathcal{E} = \int_{S_{lv}} \gamma dA - \int_{S_{sl}} \gamma \cos\theta dA - \int_{V_l} p dV. \tag{8.12}$$

The axisymmetric droplet is schematically depicted in Fig. 8.4. It is easier to integrate $V = V_l + V_i$ and so we have to subtract the volume V_i. A known function $g(r, z) = 0$ defines the topology of the top surface. Assuming axisymmetry and parameterizing the shape by t we may recast the integral as

$$\begin{aligned}\mathcal{E} = & \int_{t_1}^{t_2} \pi \left(2\gamma r\sqrt{\dot{r}^2 + \dot{z}^2} - pr^2\dot{z}\right) dt \\ & - \gamma\cos\theta S_{sl}(r_2) + pV_i(r_2),\end{aligned} \tag{8.13}$$

or simply $\mathcal{E} = \int_{t_1}^{t_2} F(r, \dot{r}, \dot{z}, t)dt + f(r_2)$, where again numbered subscripts indicate evaluation at t_1 or t_2 and the over-dot represents a partial derivative with respect to t. Note that since the topology of the upper surface is known then the only unknown for S_{sl} and V_i is the location of the contact point, r_2.

Extremizing Eq. (8.13) leads to the Young-Laplace equation

$$\frac{d}{dt}\left[\frac{2\gamma r\dot{z}}{\sqrt{\dot{r}^2 + \dot{z}^2}} - pr^2\right] = 0, \tag{8.14}$$

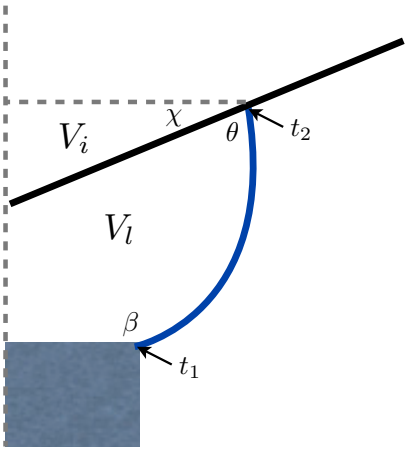

Figure 8.4: Schematic representation of an axisymmetric pinned droplet compressed by a cone of slope χ. The angle θ indicates the contact angle with the top surface ($t = t_2$) and β the apparent contact angle with the bottom surface ($t = t_1$). Here V_l is the volume of the liquid and V_i is the volume of revolution inside the cone from its tip to t_2.

and the boundary condition

$$\left(\frac{\partial f}{\partial r_2} + \frac{\partial F}{\partial \dot{r}} - \frac{\partial F}{\partial \dot{z}}\frac{\partial g/\partial r}{\partial g/\partial z}\right)\Bigg|_{t=t_2} = 0. \tag{8.15}$$

Eq. (8.14) was shown by Howe [94], as restated in English by Gillette and Dyson [95], to have a solution

$$r(t) = \Lambda\sqrt{1 - \sin^2\Omega \sin^2 t}, \tag{8.16a}$$

$$z(t) = \Lambda[E_2(\Omega, t) + E_1(\Omega, t)\cos\Omega], \tag{8.16b}$$

where

$$E_i = \int_0^t (1 - \sin^2\Omega \sin t')^{-3/2+i} dt', \tag{8.17}$$

are elliptic integrals of the first and second kind. The solution described by Eq. (8.16) has two parameters: the first one, Λ, with units of length, merely acts as a scaling factor; the second parameter, Ω, which is dimensionless, modulates the shape, and may be interpreted through the mean curvature H as follows

$$\cos\Omega = \frac{1 - \Lambda H}{\Lambda H}. \tag{8.18}$$

From this point on we rescale all distances by Λ (equivalently we set $\Lambda = 1$). Note that using these parameters, the pressure is then given by

$$\frac{p}{\gamma} = \frac{2}{\Lambda(1+\cos\Omega)}. \tag{8.19}$$

We note that the energy functional in Eq. (8.13) may be recast using a unit speed parameter s (arclength of the generatrix) [105] which then simplifies the formulae shown here; however, because the analytical axisymmetric solution is nonunit speed[100, 105] we leave the formulation general.

Boundary conditions

If the upper surface is a cone with slope χ as in Fig. 8.4 then it is described by

$$g(r,z) = r\tan\chi - (z-h) = 0, \tag{8.20}$$

where h is the smallest separation between the pinned surface and g. The flat wall is included here as the special case $\chi = 0$. We now have

$$f(r_2) = -\gamma\cos\theta\frac{\pi r_2^2}{\cos\chi} + p\frac{\pi r_2^3}{3}\tan\chi. \tag{8.21}$$

Using Eq. (8.21) into Eq. (8.15) we obtain the contact angle condition

$$\dot{z}_2 = \dot{r}_2\tan(\theta+\chi). \tag{8.22}$$

By differentiating our solution, Eq. (8.16), and substituting into Eq. (8.22) we can then obtain the location of the contact point as

$$t_2 = \frac{1}{2}\left(\theta+\chi-\arccos\left[-\cos(\theta+\chi)\cot\left(\frac{\Omega}{2}\right)^2\right]\right). \tag{8.23}$$

Note that if we select $\theta = \pi/2 - \chi$ then we obtain $t_2 = 0$ as expected. Also, since the droplet shape is symmetric about the point $t = 0$, the starting point (pinned contact point on the bottom surface) is given by the negative of the formula for t_2, and we have

$$t_1 = \frac{1}{2}\left(-\beta+\arccos\left[-\cos\beta\cot\left[\frac{\Omega}{2}\right]^2\right]\right), \tag{8.24}$$

where in Eq. (8.24) β is the apparent contact angle with the horizontal bottom surface. The point where $\beta = \pi$ is referred to as the Steiner limit[97]. In the two-dimensional analysis, recall that we obtained that the droplet goes unstable when the apparent contact angle, β, is parallel to the upper surface and hence $t_1 = t_1^c$ when $\beta = \pi - \chi$. We show below that this is true only when the wall is flat $\chi = 0$, but does not remain valid when $\chi \neq 0$.

Physical contact

If the slope of the cone is nonzero, $\chi \neq 0$, we run the risk of having physical contact between the upper surface and lower surface prior to the instability hence we have to limit the regime of Ω and t_1 (or β) to exclude this possibility. Since the parameter Λ merely scales the shape it is inconsequential. Solving the equation

$$z(t_2, \Omega) - z(t_1, \Omega) = r(t_2, \Omega) \tan \chi, \tag{8.25}$$

yields the limit of physically realizable solutions in the Ω-t_1 plane.

Perturbations

In order to observe the instability of axisymmetric shapes, following the method of Russo and Steen [97], we add to our axisymmetric solution (defined by $r(t)$ and $z(t)$) small, non-axisymmetric perturbations defined by the functions $F(t, \phi)$ and $G(t, \phi)$ which contain explicit dependence on the azimuthal angle ϕ. The liquid-vapor interface is thus given by the following equations

$$R(t, \phi) = r(t) + F(t, \phi), \tag{8.26}$$

$$Z(t, \phi) = z(t) + G(t, \phi). \tag{8.27}$$

The perturbations given by F and G must yield shapes which satisfy the boundary conditions and preserve volume, $\Delta V_l \equiv V_l(R, Z) - V_l(r, z) = 0$, in order to be viable.

To discover the onset of the instability we solve for $t_1^c(\Omega)$ such that surface energy of the perturbed shape is equal to the axisymmetric shape $\Delta E = E(R, Z) - E(r, z) = 0$. This will yield the point of the instability for any axisymmetric shape Ω. The results of this perturbative analysis are given below while the mathematical

details are given in Appendix C. The perturbation analysis can only reveal the onset of the asymmetry; to probe the mechanical properties of the asymmetric droplets Surface Evolver simulations are used in Section 8.4. Alternatively, other schemes [100, 101], often developed for liquid bridges, might be adapted for use with the contact angle boundary condition.

Results

Our theoretical results are illustrated in Fig. 8.5. We plot the dependance of the critical point at which the axisymmetric state becomes unstable to non-axisymmetric perturbations, $t_1^c(\Omega)$, with the shape parameter, Ω, for contact angles on the upper surface ranging from $\pi/4$ to π. The case of a flat wall is shown in Fig. 8.5a while the conical surface with $\chi = \pi/8$ is displayed in Fig. 8.5b. In both figures, the dotted lines are examples of a paths of constant volume with arrows indicating the direction of decreasing gap separation.

Plotted in Fig. 8.5 as a dashed line is the Steiner limit which corresponds to an apparent contact angle on the (bottom) pinned surface of $\beta = \pi$, while the solid line indicates where the apparent contact angle at the bottom surface is parallel to the top surface, i.e. $\beta = \pi - \chi$. In the case of a flat wall, $\chi = 0$, the two lines are coincident. For this geometry we see that for any contact angle on the upper surface the point of instability occurs on or immediately after the Steiner limit. Since we use only a truncated and restricted series to represent the asymmetric perturbations (see Appendix C), this results represents an upper bound. Using a symmetrization argument, Gillete and Dyson showed that the droplets in a liquid bridge [97, 98, 99, 100, 101], which can be represented by single valued functions $r(z)$ (in other words droplets prior to the Steiner limit), are stable to axisymmetric perturbations [96]. There is nothing in their argument that prohibits its application when we permit r_2 to be variable so long as z_2 is fixed; however, such a map does not preserve contact angle. To apply in our case when $\chi = 0$ we must adjust the contact angle, but it can easily be shown that one can always smoothly change the contact angle with a vanishing change in the surface area and volume. As lower and upper bound coincide, we get the final result that, in the flat wall case, the

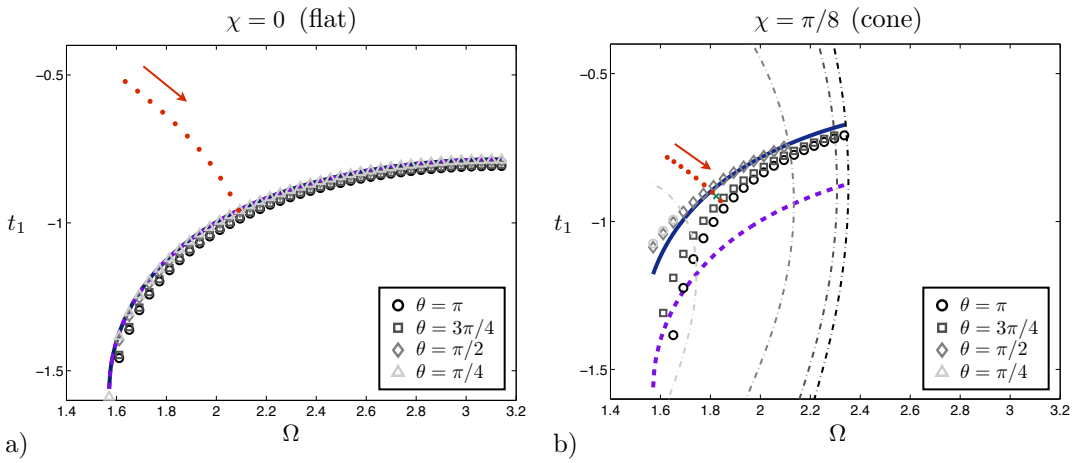

Figure 8.5: The onset of the asymmetric instability with varying shape Ω. The points indicate the limit of stability found by solving $\Delta E(t_1) = 0$ for a flat wall (case a, $\chi = 0$) and a conical top surface (case b, $\chi = \pi/8$). The contact angle θ on the top surface varies between $\pi/4$ and π by $\pi/4$ increments. The dashed line indicates the point when the apparent contact angle $\beta = \pi$ (droplet tangent to the bottom surface) while the solid line indicates when $\beta = \pi - \chi$ (bottom contact line parallel to the top surface); these two limits coincide in the flat wall case of (a). The dash-dot lines indicate the limit of physically realizable solutions when $\chi \neq 0$. Our parameter $\alpha \in (-0.06, -0.29)$ is selected to give the earliest possible instability. We see when $\chi = 0$ (flat wall) the limit of stability always corresponds to $\beta = \pi$, but when $\chi \neq 0$ the data do not always lie on either the $\beta = \pi - \chi$ or $\beta = \pi$ curves. The dotted lines in each plot are examples of a paths of constant volume with arrows indicating the direction of decreasing gap separation; they are further illustrated in Figs. 8.7 and 8.8.

limit of stability is when the droplet is parallel to the pinned surface at the point of contact (apparent contact angle of π), similarly to the stability threshold for liquid bridges and sessile droplets [93, 101].

The case where the top surface is conical ($\chi = \pi/8$, Fig. 8.5b) shows a different stability behavior. Because the upper surface may now contact the lower surface before the droplet goes unstable, a portion of parameter space, depending on the contact angle, is excluded; this is indicated by the dash-dotted lines. Our stability calculations show, in this case, that the droplet does not always go unstable when its surface is parallel to the upper surface (blue solid line) nor when it is tangent to the lower surface (purple dashed line). The two-dimensional prediction cannot therefore be extended to three dimensions.

Unlike the flat surface case, the symmetrization argument clearly does not hold when $\chi \neq 0$ and hence our prediction here for the limit of stability can only be regarded as an upper bound. We will show in the next section that this prediction can perform well nevertheless.

8.4 Surface Evolver computations

In order to corroborate our asymptotic predictions we appeal to numerical simulations using Surface Evolver (SE) [109]. Nagy and Neitzel also used the same program to confirm the existence of their observed instability in an idealized setting [106]. In Surface Evolver the droplet shape is discretized into triangular facets whose positions are defined by a position vector $\mathbf{X}$ hence the energy is $E(\mathbf{X})$ [112]. At a minimum of energy we have $\boldsymbol{\nabla} E = 0$ and the Hessian matrix, $\mathbf{H} = \partial^2 E/\partial X_i \partial X_j$, must be positive definite. We run SE simulations of both the flat and conical geometries and see that, as the separation h approaches a critical separation h^c, the smallest eigenvalue of $\mathbf{H}$ approaches zero. If the separation is reduced below this critical separation, the symmetric form yields negative eigenvalues and the true minimum is then given by an asymmetric shape.

Appealing to dimensional analysis tells us that we can write the critical separation in the form $h^c/r_1 = \Phi(V_l/r_1^3, \theta, \chi)$ [97, 113]. Given that we have an

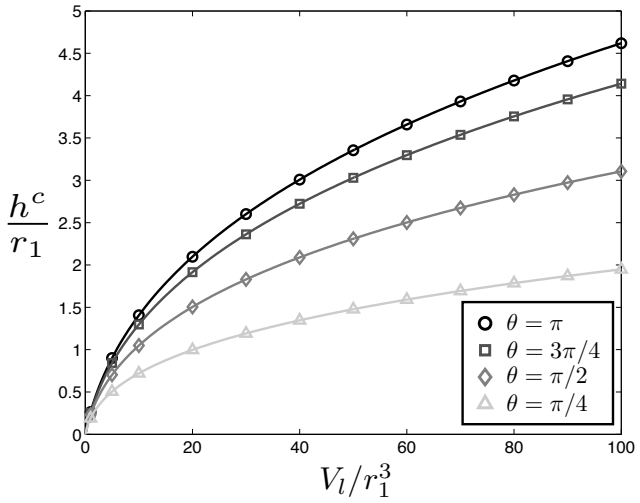

Figure 8.6: Critical separation h^c vs liquid volume V_l non-dimensionalized by the pinned radius r_1 for $\theta = \{\pi/4, \pi/2, 3\pi/4, \pi\}$ and $\chi = 0$.

analytical equation for the the limit of stability when the compressing top wall is flat ($\chi = 0$) in Eq. (8.24), we can plot this function easily for various constant θ, with results shown in solid lines in Fig. 8.6. We then run Surface Evolver, the symbols in Fig 8.6 indicate simulations performed where $h = h^c$ was stable but $h = 0.99h^c$ unstable. This then demonstrates that the instability occurs precisely as predicted theoretically in the previous section. We note that, as predicted by the two-dimensional example, the instability is the least physically apparent for large volumes and high contact angles, $\theta \to \pi$. In Surface Evolver this manifests itself by a need to use very high resolution to capture the onset of the stability in these physical regimes properly.

As a more concrete example we define a specific physical system and illustrate its transition to asymmetry. We choose as an example a droplet of volume $V = 4$ pinned on a base of radius $r_1 = 1$ (arbitrary units) compressed by a flat upper surface of contact angle $\theta = 120°$. Solving for $V(\Lambda, \Omega, t_1^c(\Omega)) = 4$ and $r(\Lambda, \Omega, t_1^c(\Omega)) = 1$ we determine theoretically that $\Lambda \approx 1.42$ and $\Omega \approx 2.089$ at a predicted critical separation $h^c \approx 0.6923$. The constant volume path of this system, from $h = 1.5h^c$ to h^c, was illustrated in parameter space in Fig. 8.5 by dots, the arrow indicating the direction of increased compression of the droplet.

In Fig. 8.7 we show the results of Surface Evolver simulations of this system

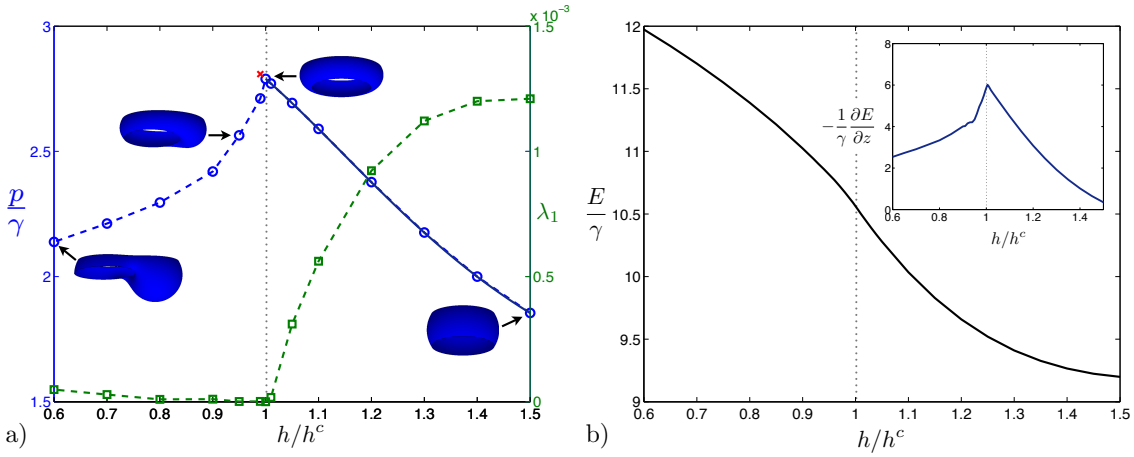

Figure 8.7: Surface evolver simulations of the onset of the instability for a flat wall, $\chi = 0$ with $V = 4$ and $r_1 = 1$. (a): Pressure, p (axis on the left, circles joined by a dashed line is numerical data and the solid line is analytical), and smallest eigenvalue of the Hessian matrix, λ_1 (squares with axis on right), versus separation h. We see that the smallest eigenvalue goes to zero, indicating a loss of stability, precisely when we predict $h = h^c$. The pressure reaches a maximum at the onset of the shape instability. The cross indicates the pressure past h^c is higher if the conformation were axisymmetric but this point is not physically realized. We have also inset graphical representations of the droplet for $h/h^c = 0.6, 0.95, 1$, and 1.5. (b): Surface energy, E, varies monotonically with the gap height. The slope of the energy (inset) indicates that the force required to deform the droplet peaks at $h = h^c$ past which the droplet becomes asymmetric and the amount of force required to deform the droplet decreases with increasing displacement. A loaded droplet would thus buckle at the transition to asymmetry.

with the separation, h, ranging $1.5h^c$ to $0.6h^c$. First and foremost, we see that the instability occurs precisely at the analytically predicted $h = h^c$. The pressure in the droplet increases until the critical point where the smallest eigenvalue in the system vanishes, indicating a loss of stability. Beyond the critical point, symmetric shapes have negative eigenvalues indicating an unstable saddle. The stable shapes beyond the critical point are asymmetric and have progressively lower pressure. In Fig. 8.7b we display the variation of the surface energy of the droplet, E, with the separation distance between the surface; in inset we plot the slope of the energy (obtained by numerical differentiation of E), i.e. the force acting on both surfaces resisting compression. The surface energy progressively increases as we deform the droplet from $h = 1.5h^c$ to $h = 0.6h^c$. The slope of the energy (shown in the inset) indicates that the force required in order to further deform the droplet peaks at the critical separation and then monotonically decreases with increasing deformation.

Experimentally, if we were to progressively load a droplet with increasing force, then at the point when the droplet is tangent to the pinned area it would become mechanically unstable, regardless of the contact angle of the deforming surface (and true for both two- and three-dimensional systems). The system would undergo a dynamic collapse past this point. These mechanical considerations are important for the design of systems such as the one described by Neitzel et al. for load support in a non-wetting scenario [107, 108, 106]. The peak load occurs at the critical shape, beyond which the droplet undergoes a limit-point buckling instability, and collapses.

With $\chi \neq 0$ we are not assured that an axisymmetric instability can occur prior to contact between the upper and lower surface. Since we do not have a analytical expression for the unstable point, when we must solve $\Delta E(\Omega, t_1^c) = 0$ given by Eq. (C.16), together with $V(\Lambda, \Omega, t_1^c) = 10$ and $r(\Lambda, \Omega, t_1^c) = 1$, with $\chi = \pi/8$ and $\theta = 3\pi/4$, to obtain our predictions $\Lambda \approx 1.575$, $\Omega \approx 1.84$ and a contact point $t_1^c \approx -0.93$. We then compute our predicted critical separation $h^c = z_2 - z_1^c - r_2 \tan\chi \approx 1.18$. As discussed the analytical prediction serves as an upper bound on the energy at the critical point, and we see when compared to the SE simulations, shown in Fig. 8.8, that the analysis slightly under-predicts the

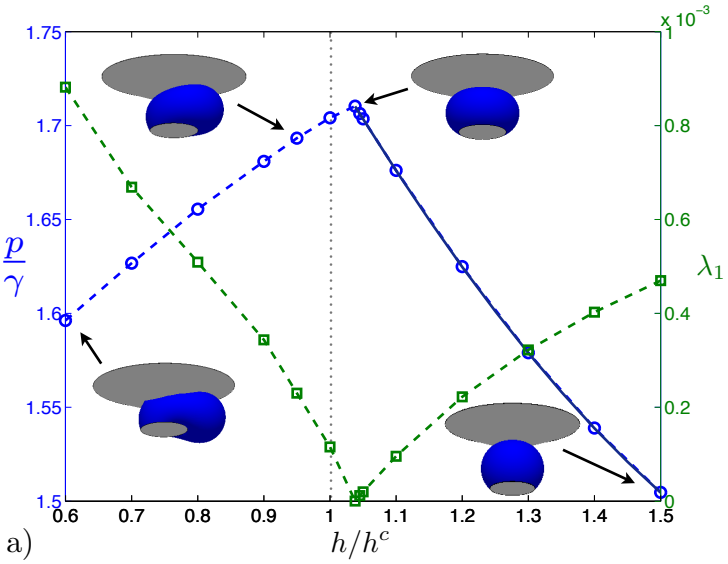

Figure 8.8: Surface Evolver simulations of the onset of the instability in the case where the top surface is conical, $\chi = \pi/8$. Same notation and parameters as in Fig. 8.7. The smallest eigenvalue goes to zero, and the pressure reaches a maximum, just past our calculated stability limit, at about $h \approx 1.04h^c$. Insets show graphical representations of the droplet for $h/h^c = 0.6, 0.95, 1$ and 1.5.

critical separation, and we obtain numerically that the droplet becomes asymmetric when $h \approx 1.038h^c$.

The path from $h = 1.5h^c$ to $h = 0.6h^c$ was shown earlier in Fig. 8.5b) by dotted lines, the cross along this path indicates where the instability occurs in Surface Evolver. Similarly to the flat wall case, we find the droplet displays a drop in pressure after losing axisymmetry, indicating the presence of a limit-point buckling instability.

8.5 Conclusion

In this chapter, motivated by recent experiments by Nagy and Neitzel [106], we have used theory and computations to show that a droplet, pinned at the bottom by a surface of finite area, if sufficiently deformed by a surface at the top, will always develop a shape instability at a critical compression – a result true for all values of the contact angle between the droplet and the top surface. After

the critical compression, the droplet will then transition from a symmetric shape to an asymmetric shape. The force required to deform the droplet peaks at the critical point then progressively decreases indicative of a buckling instability. If the deforming surface is flat then we predict the instability to occur when the apparent contact angle of the droplet at the pinned surface is π, regardless of the contact angle of the upper surface, similarly to past work on liquid bridges and sessile droplets. However, when the upper surface has non-trivial topology this criterion no longer holds, and a detailed stability analysis is carried out to predict the critical compression. An interesting question for future work would be to explore the effects of surface curvature on the shape instability.

Chapter 8, in part, is a reprint of the material as it appears in Physics of Fluids 2012. Elfring, Gwynn J.; Lauga, Eric, the American Institute of Physics, 2012. The dissertation author was the primary investigator and author of this paper.

Appendix A

Phase locking asymptotics

A.1 Fourth order expansion

A.1.1 Flow at $\mathcal{O}(\epsilon)$

The governing equation at $\mathcal{O}(\epsilon)$ is

$$\nabla^4 \psi_1 = 0, \tag{A.1}$$

and the boundary conditions are given by

$$\nabla \psi_1 \mid_{y=0} = \nabla g(x), \tag{A.2a}$$

$$\nabla \psi_1 \mid_{y=\bar{h}} = \nabla g(x+\phi) + \mathbf{e}_y U_{\Delta 1}, \tag{A.2b}$$

where $\mathbf{e}_y$ denotes the unit vector in the y direction. We note that the boundary conditions at $\mathcal{O}(\epsilon)$ are the same for both extensible and inextensible motion.

The biharmonic equation can be solved by repeated separation of variables.

The general solution may be expressed as

$$\begin{aligned}\psi_1(x,y) &= A_{1,0} + B_{1,0}y + C_{1,0}y^2 + D_{1,0}y^3 \\ &\quad + (E_{1,0} + F_{1,0}y + G_{1,0}y^2 + H_{1,0}y^3)x \\ &\quad + \sum_{n=1}^{\infty}\Big[(A_{1,n} + B_{1,n}y)\sinh(ny) \\ &\qquad + (C_{1,n} + D_{1,n}y)\cosh(ny)\Big]\cos(nx) \\ &\quad + \sum_{n=1}^{\infty}\Big[(E_{1,n} + F_{1,n}y)\sinh(ny) \\ &\qquad + (G_{1,n} + H_{1,n}y)\cosh(ny)\Big]\sin(nx), \end{aligned} \tag{A.3}$$

where for the constants A through H, the first subscript refers to the order in the expansion (here, first order) and the second refers to the corresponding Fourier mode. We can immediately discard the terms linear in x due to the periodicity of the problem.

From the first order boundary conditions, Eq. (A.2), we get that the solution to the biharmonic equation may be written analytically as

$$\psi_1 = a_{1,0}(y) + \sum_{n=1}^{\infty}\Big[a_{1,n}(y)\cos(nx) + b_{1,n}(y)\sin(nx)\Big], \tag{A.4}$$

where

$$a_{1,0}(y) = \frac{\left(U_{\Delta 1} - 3\mathrm{D}_{1,0}\bar{h}^2\right)y^2}{2h} + U_{\Delta 1}y^3, \tag{A.5}$$

$$a_{1,n}(y) = 2P_n(y)\big(\alpha_n\cos(n\phi) + \beta_n\sin(n\phi)\big) + \alpha_n Q_n(y), \tag{A.6}$$

$$b_{1,n}(y) = 2P_n(y)\big(\beta_n\cos(n\phi) - \alpha_n\sin(n\phi)\big) + \beta_n Q_n(y), \tag{A.7}$$

and

$$P_n(y) = \left[\frac{n^2\bar{h}y\cosh(n\bar{h}) + \sinh(n\bar{h})ny}{2n^2\bar{h}^2 - 2\sinh^2(n\bar{h})}\right]\cosh(ny) - \left[\frac{\left(1+\bar{h}n^2y\right)\sinh(n\bar{h}) + hn\cosh(n\bar{h})}{2n^2\bar{h}^2 - 2\sinh^2(n\bar{h})}\right]\sinh(ny), \tag{A.8}$$

$$Q_n(y) = \left[\frac{2n\bar{h} + 2ny\sinh^2(n\bar{h}) + \sinh(2n\bar{h})}{2n^2\bar{h}^2 - 2\sinh^2(n\bar{h})}\right]\sinh(ny) + \left[1 - \frac{2\bar{h}n^2y + ny\sinh(2n\bar{h})}{2n^2\bar{h}^2 - 2\sinh^2(n\bar{h})}\right]\cosh(ny). \tag{A.9}$$

The force on the top sheet is

$$F_{1x} = -\frac{2\pi}{\bar{h}}U_{\Delta 1}. \tag{A.10}$$

If $U_{\Delta 1} = 0$ then there is no phase locking force. Conversely if the sheets are force free then $U_{\Delta 1} = 0$. There is thus no synchronization at $\mathcal{O}(\epsilon)$, as expected from the $\epsilon \to -\epsilon$ symmetry.

A.1.2 Flow at $\mathcal{O}(\epsilon^2)$

The governing equation at $\mathcal{O}(\epsilon^2)$ is

$$\nabla^4\psi_2 = 0, \tag{A.11}$$

while the boundary conditions are given by

$$\nabla\psi_2\,|_{y=0} = -g(x)\nabla\left(\frac{\partial\psi_1}{\partial y}\right)|_{y=0} + \frac{\mathbf{e}_y}{2}\left[g'(x)^2 - \frac{1}{2\pi}\int_0^{2\pi} g'(x)^2dx\right], \tag{A.12}$$

$$\nabla\psi_2\,|_{y=\bar{h}} = \mathbf{e}_y U_{\Delta 2} - g(x+\phi)\nabla\left(\frac{\partial\psi_1}{\partial y}\right)|_{y=\bar{h}} + \frac{\mathbf{e}_y}{2}\left[g'(x+\phi)^2 - \frac{1}{2\pi}\int_0^{2\pi} g'(x+\phi)^2dx\right], \tag{A.13}$$

where the terms in the square brackets represent the contribution from the inextensibility constraint.

The solution to the biharmonic equation is written

$$\psi_2 = a_{2,0}(y) + \sum_{n=1}^{\infty} a_{2,n}(y)\cos(nx) + \sum_{n=1}^{\infty} b_{2,n}(y)\sin(nx). \tag{A.14}$$

The zeroth mode is given by

$$a_{2,0}(y) = u_{20}y + \frac{(U_{\Delta 2} + u_{2h} - u_{20})\, y^2}{2\bar{h}}, \tag{A.15}$$

The force on the top sheet is then given as

$$F_{2x} = \frac{2\pi}{\bar{h}}(u_{20} - u_{2h} - U_{\Delta 2}). \tag{A.16}$$

The mean components of the horizontal boundary conditions must then be evaluated, the lower

$$u_{20} = \frac{1}{2\pi}\int_0^{2\pi} \Bigg\{ -g(x)\left(\frac{\partial^2 \psi_1}{\partial y^2}\right)|_{y=0} + \frac{1}{2}\left[g'(x)^2 - \frac{1}{2\pi}\int_0^{2\pi} g'(t)^2 dt\right]\Bigg\} dx. \tag{A.17}$$

The term in the square brackets clearly integrates to zero, hence we are left with

$$u_{20} = -\frac{1}{2\pi}\int_0^{2\pi} g(x)\left(\frac{\partial^2 \psi_1}{\partial y^2}\right)|_{y=0}\, dx, \tag{A.18}$$

which, using orthogonality of Fourier modes, gives

$$u_{20} = -\frac{1}{2}\sum_{n=1}^{\infty}\Big[\alpha_n a''_{1,n}(0) + \beta_n b''_{1,n}(0)\Big]. \tag{A.19}$$

Similarly u_{2h} is given by

$$u_{2h} = -\frac{1}{2\pi}\int_0^{2\pi} g(x+\phi)\left(\frac{\partial^2 \psi_1}{\partial y^2}\right)|_{y=\bar{h}}\, dx, \tag{A.20}$$

which may be evaluated to give

$$u_{2h} = -\frac{1}{2}\sum_{n=1}^{\infty}\Big[(\alpha_n a''_{1,n}(\bar{h}) + \beta_n b''_{1,n}(\bar{h}))\cos(n\phi) + (\beta_n a''_{1,n}(\bar{h}) - \alpha_n b''_{1,n}(\bar{h}))\sin(n\phi)\Big]. \tag{A.21}$$

Further, by considering P_n and Q_n, given by Eq. (A.7) and Eq. (A.8) respectively, and observing that $2P_n''(\bar{h}) = -Q_n''(0)$ and $2P_n''(0) = Q_n''(h)$ it can be shown that

$$u_{20} - u_{2h} = \frac{1}{2}\sum_{1}^{\infty}(\alpha_n^2 + \beta_n^2)\Big[2P_n''(\bar{h}) - Q_n''(0) - \cos(n\phi)\Big(2P_n''(0) - Q_n''(\bar{h})\Big)\Big] = 0, \tag{A.22}$$

as each term in the sum is zero for all n.

The force on the top sheet is then equal to

$$F_{2x} = -\frac{2\pi}{\bar{h}}U_{\Delta 2}. \tag{A.23}$$

Here again we see that when we allow the swimmers to move in a force free manner then $U_{\Delta 2} = 0$ and hence there is no synchronization at $\mathcal{O}(\epsilon^2)$. Note that we have not specified the Fourier coefficients of the of the waveform, and this result is therefore valid for any waveform $g(x)$.

Sadly, due to the $\epsilon \to -\epsilon$ symmetry of the model there cannot be any force at $\mathcal{O}(\epsilon^3)$, and therefore we expect the force to arise at best at $\mathcal{O}(\epsilon^4)$.

A.1.3 Flow at $\mathcal{O}(\epsilon^3)$

The third order component of Eq. (3.9) is

$$\nabla^4\psi_3 = 0. \tag{A.24}$$

with the third order boundary conditions

$$\begin{aligned}\nabla\psi_3\,|_{y=0} &= -g(x)\left[\nabla\left(\frac{\partial\psi_2}{\partial y}\right) + \frac{g(x)}{2}\nabla\left(\frac{\partial^2\psi_1}{\partial y^2}\right)\right]|_{y=0} \\ &\quad - \mathbf{e}_x\frac{g'(x)}{2}\left[g'(x)^2 - \frac{1}{2\pi}\int_0^{2\pi} g'(x)^2dx\right], \end{aligned}\tag{A.25}$$

$$\begin{aligned}\nabla\psi_3\,|_{y=\bar{h}} &= \mathbf{e}_y U_{\Delta 3} - g(x+\phi)\times \\ &\quad \left[\nabla\left(\frac{\partial\psi_2}{\partial y}\right) + \frac{g(x+\phi)}{2}\nabla\left(\frac{\partial^2\psi_1}{\partial y^2}\right)\right]|_{y=\bar{h}} \\ &\quad - \mathbf{e}_x\frac{g'(x+\phi)}{2}\times \\ &\quad \left[g'(x+\phi)^2 - \frac{1}{2\pi}\int_0^{2\pi} g'(x+\phi)^2dx\right]. \end{aligned}\tag{A.26}$$

The force again takes the form

$$F_{3x} = \frac{2\pi}{\bar{h}} \left(u_{30} - u_{3h} - U_{\Delta 3} \right). \tag{A.27}$$

If the swimmers are force free we see $U_{\Delta 3} = u_{30} - u_{3h}$ but due to the $\epsilon \to -\epsilon$ symmetry of the geometry we must have $U_{\Delta 3} = 0$ (in the example we consider in Sec. 3.7 $u_{30} = u_{3h} = 0$).

A.1.4 Flow at $\mathcal{O}(\epsilon^4)$

The fourth order component of Eq. (3.9) is

$$\nabla^4 \psi_4 = 0. \tag{A.28}$$

The boundary conditions at fourth order are given by

$$\begin{aligned}
\nabla\psi_4 \mid_{y=0} &= -g(x) \left[\nabla \left(\frac{\partial \psi_3}{\partial y} \right) + \frac{g(x)}{2} \nabla \left(\frac{\partial^2 \psi_2}{\partial y^2} \right) + \frac{g(x)^2}{6} \nabla \left(\frac{\partial^3 \psi_1}{\partial y^3} \right) \right] \mid_{y=0} \\
&\quad - \mathbf{e}_y \frac{g'(x)^2}{4} \left[\frac{3}{2} g'(x)^2 - \frac{1}{2\pi} \int_0^{2\pi} g'(x)^2 dx \right] + \frac{\mathbf{e}_y}{16\pi} \int_0^{2\pi} g'(x)^4 dx, \qquad \text{(A.29)} \\
\nabla\psi_4 \mid_{y=\bar{h}} &= -g(x+\phi) \\
&\quad \times \left[\nabla \left(\frac{\partial \psi_3}{\partial y} \right) + \frac{g(x+\phi)}{2} \nabla \left(\frac{\partial^2 \psi_2}{\partial y^2} \right) + \frac{g(x+\phi)^2}{6} \nabla \left(\frac{\partial^3 \psi_1}{\partial y^3} \right) \right] \mid_{y=\bar{h}} \\
&\quad - \mathbf{e}_y \frac{g'(x+\phi)^2}{4} \left[\frac{3}{2} g'(x+\phi)^2 - \frac{1}{2\pi} \int_0^{2\pi} g'(x+\phi)^2 dx \right] \\
&\quad + \mathbf{e}_y U_{\Delta 4} + \frac{\mathbf{e}_y}{16\pi} \int_0^{2\pi} g'(x+\phi)^4 dx. \qquad \text{(A.30)}
\end{aligned}$$

The force on the upper sheet is

$$F_{4x} = \frac{2\pi}{\bar{h}} (u_{40} - u_{4h} - U_{\Delta 4}). \tag{A.31}$$

Setting $U_{\Delta 4} = 0$ gives rise to a phase-locking force in the static case and for free-swimming we set $F_{4x} = 0$ and solve for $U_{\Delta 4}$. As at all previous orders the force and swimming speed are identically zero, the fourth order results are the leading order terms in the asymptotic expansion.

Importantly, the formulae for u_{40} and u_{4h}, defined in Eq. (3.17), are too unwieldy for the most enterprising appendix even for simple $g(x)$, and hence are not stated explicitly (although straightforward to obtain with a symbolic calculation package).

A.2 Vertical force

In a manner similar to the horizontal force, the integral for the vertical force on the bottom sheet may be expanded on the x-axis as follows

$$F_y = \int_0^{2\pi} \left[\sigma_{yy} + \sum_{n=1}^{\infty} \epsilon^n \frac{\partial}{\partial x} \left(\frac{n-1}{n!} g^n \frac{\partial^{n-1} \sigma_{xy}}{\partial y^{n-1}} \right) \right]_{y=0} dx. \tag{A.32}$$

The term in the sum is a perfect derivative and hence zero for all n, so therefore

$$F_y(y) = -\int_0^{2\pi} \left[p + 2 \frac{\partial^2 \psi}{\partial x \partial y} \right]_{y=0} dx. \tag{A.33}$$

The second term is a perfect derivative in x, and hence in a 2π periodic system gives zero when integrated over a period. We thus have

$$F_y = -\int_0^{2\pi} p dx. \tag{A.34}$$

Upon integrating the Stokes equations using the Fourier form of the stream function (3.15) and matching we arrive at

$$F_y = -2\pi C \tag{A.35}$$

where C is an unknown constant of integration. This indicates that there is no dynamic contribution to the vertical force.

Appendix B

Finite swimmer terms

B.1 Flagellum equations

B.1.1 Local operator

The local operator $\boldsymbol{L}$ represents the local flagellar interaction with the flow field. For the swimmer 1 this is written below

$$\begin{aligned}\langle \mathcal{L}_1[\mathbf{f}_1]P_i\rangle &= -\frac{1}{8\pi}\left\langle \left[(\mathbf{I}+\mathbf{t}_1(s)\mathbf{t}_1(s))\ln(\epsilon^{-2})+\mathbf{I}-3\mathbf{t}_1(s)\mathbf{t}_1(s)\right]\sum_{j=0}^{N}\mathbf{a}_{1j}P_j(s)P_i(s)\right\rangle,\\ &= -\frac{1}{8\pi}\sum_j \langle P_iP_j\mathbf{L}_1\rangle\cdot\mathbf{a}_{1j},\end{aligned} \tag{B.1}$$

where we have labeled the term in the square brackets as $\mathbf{L}_1$. The equations the first and second swimmers are then written as a single the linear operator $\boldsymbol{L}$ acting on our vector of unknowns $\boldsymbol{a}$.

B.1.2 The non-local operator

The non-local operator $\boldsymbol{K}$ represents the interaction of each flagella with its own flow field. This interaction, for the first swimmer may be written as

$$\begin{aligned}\mathcal{K}_1[\mathbf{f}_1](s) = -\frac{1}{8\pi}\int_{-1}^{1}\left[\mathbf{S}_1(s,s')-\left(\frac{\mathbf{I}+\mathbf{t}_1(s)\mathbf{t}_1(s)}{|s-s'|}\right)\right]\cdot\mathbf{f}_1(s')ds'\\ -\frac{1}{8\pi}(\mathbf{I}+\mathbf{t}_1(s)\mathbf{t}_1(s))\int_{-1}^{1}\frac{\mathbf{f}_1(s')-\mathbf{f}_1(s)}{|s-s'|}ds.\end{aligned} \tag{B.2}$$

The first term is regular while the second term is singular and hence we deal with these two terms separately. We label the term in the square brackets as the tensor $\mathbf{K}_1$. Taking the inner product of the first term with the i$^{\text{th}}$ Legendre polynomial we obtain

$$\begin{aligned}\int_{-1}^{1} P_i(s) \int_{-1}^{1} \mathbf{K}_1(s,s') \cdot \mathbf{f}_1(s') ds' ds &= \sum_j \int_{-1}^{1}\int_{-1}^{1} P_i(s) P_j(s') \mathbf{K}_1(s,s') \cdot \mathbf{a}_{1j} ds' ds, \\ &= \sum_j \langle\langle P_i(s) P_j(s') \mathbf{K}_1(s,s') \rangle\rangle \cdot \mathbf{a}_{1j}. \end{aligned} \tag{B.3}$$

For the second term we use the Götz result

$$\int_{-1}^{1} \frac{\mathbf{f}(s') - \mathbf{f}(s)}{|s'-s|} ds' = \sum_{j=0}^{N-1} \lambda_j P_j(s) \mathbf{a}_j, \tag{B.4}$$

where $\lambda_j = \sum_{n=1}^{j} n^{-1}$ and $\lambda_0 = 0$. Hence the inner product of the second term with the i$^{\text{th}}$ Legendre polynomial is simply

$$-\frac{1}{8\pi} \left\langle P_i(s)(\mathbf{I} + \mathbf{t}_1(s)\mathbf{t}_1(s)) \cdot \sum_j \lambda_j P_j(s) \mathbf{a}_{1j} \right\rangle = -\frac{1}{8\pi} \sum_j \langle \lambda_j P_i(s) P_j(s) \mathbf{T}_1(s) \rangle \cdot \mathbf{a}_{1j}, \tag{B.5}$$

where $\mathbf{T} = \mathbf{I} + \mathbf{t}(s)\mathbf{t}(s)$. These two components together, for both swimmers combine to yield the non-local operator $\boldsymbol{K}$.

B.1.3 Flow from the flagellum

Now we tackle the flow field from one flagellum onto the next

$$\begin{aligned}\langle \mathbf{u}_{2f}[\mathbf{f}_2] P_i \rangle &= -\frac{1}{8\pi} \int_{-1}^{1}\int_{-1}^{1} \mathbf{G}(\mathbf{x}_1(s) - \mathbf{x}_2(s')) \cdot \mathbf{f}_2(s') ds' P_i(s) ds, \\ &= -\frac{1}{8\pi} \sum_j \langle\langle P_i(s) P_j(s') \mathbf{G}_1(s,s') \rangle\rangle \cdot \mathbf{a}_{2j}. \end{aligned} \tag{B.6}$$

The term $\boldsymbol{G}_f$ contains this interaction on each swimmer respectively.

B.1.4 Flow from the heads

The flows on the flagella from its own head and the other head are given respectively after projection onto the i$^{\text{th}}$ Legendre polynomial as

$$\langle \mathbf{u}_{1h}[\mathbf{F}_1, T_1] P_i \rangle = -\frac{1}{8\pi} \left\{ \left\langle P_i \mathbf{G}_h(\mathbf{x}_1(s) - \mathbf{x}_1^h) \right\rangle \cdot \mathbf{F}_1 + \left\langle P_i \mathbf{v}(\mathbf{x}_1(s) - \mathbf{x}_1^h) T_1 \right\rangle \right\}, \quad \text{(B.7)}$$

$$\langle \mathbf{u}_{2h}[\mathbf{F}_2, T_2] P_i \rangle = -\frac{1}{8\pi} \left\{ \left\langle P_i \mathbf{G}_h(\mathbf{x}_1(s) - \mathbf{x}_2^h) \right\rangle \cdot \mathbf{F}_2 + \left\langle P_i \mathbf{v}(\mathbf{x}_1(s) - \mathbf{x}_2^h) T_2 \right\rangle \right\}. \quad \text{(B.8)}$$

These effects, for both swimmers, comprise the operator $\boldsymbol{G}_h$.

B.1.5 Rigid body motion

The rigid body motion of the flagellum comes from the sum of the motion of the head and a rotation centered at the head. Projected onto the Legendre polynomials these terms are given

$$-\dot{\mathbf{x}}_1^h \langle P_i \rangle - \dot{\theta}_1 \left\langle \mathbf{r}_1^{\perp} P_i \right\rangle. \quad \text{(B.9)}$$

The only Legendre polynomial with nonzero mean is the $k = 0$ term. We collect this and the equivalent for the second swimmer into the operator $\boldsymbol{U}_f$.

B.2 Head equations

B.2.1 Flow from flagella

The head of the first swimmer interacts with the flow that is generated by its own flagella and flagella of the second swimmer as given below.

$$\mathcal{F}_1^t \mathbf{u}_{1f}[\mathbf{f}_1] = -\frac{1}{8\pi} \sum_j \left\langle \mathbf{G}_{hf}(\mathbf{x}_1^h - \mathbf{x}_1(s)) P_j \right\rangle \cdot \mathbf{a}_{1j}, \quad \text{(B.10)}$$

$$\mathcal{F}_1^t \mathbf{u}_{2f}[\mathbf{f}_2] = -\frac{1}{8\pi} \sum_j \left\langle \mathbf{G}_{hf}(\mathbf{x}_1^h - \mathbf{x}_2(s)) P_j \right\rangle \cdot \mathbf{a}_{2j}, \quad \text{(B.11)}$$

$$\mathcal{F}_1^\theta \mathbf{u}_{1f}[\mathbf{f}_1] \cdot \mathbf{e}_z = \frac{1}{8\pi} \sum_j \left\langle \mathbf{v}(\mathbf{x}_1^h - \mathbf{x}_1(s)) P_j \right\rangle \cdot \mathbf{a}_{1j}, \quad \text{(B.12)}$$

$$\mathcal{F}_1^\theta \mathbf{u}_{2f}[\mathbf{f}_2] \cdot \mathbf{e}_z = \frac{1}{8\pi} \sum_j \left\langle \mathbf{v}(\mathbf{x}_1^h - \mathbf{x}_2(s)) P_j \right\rangle \cdot \mathbf{a}_{2j}. \quad \text{(B.13)}$$

These terms and those for the second swimmer are captured by the operator $\boldsymbol{H}_f$.

B.2.2 Flow from head

The head of the first swimmer also interacts with the flow generated by the head of the second swimmer,

$$\mathcal{F}^t \mathbf{u}_{2h}[\mathbf{F}_2, T_2] = -\frac{1}{8\pi}\left[\mathbf{G}_{hh}(\mathbf{x}_1^h - \mathbf{x}_2^h)\cdot\mathbf{F}_2 + \mathbf{v}(\mathbf{x}_1^h - \mathbf{x}_2^h)T_2\right], \tag{B.14}$$

$$\mathcal{F}_1^\theta \mathbf{u}_{2h}[\mathbf{F}_2, T_2] = -\frac{1}{8\pi}\left[-\mathbf{v}(\mathbf{x}_1^h - \mathbf{x}_2^h)\cdot\mathbf{F}_2 + \frac{1}{2}\left|\mathbf{x}_1^h - \mathbf{x}_2^h\right|^{-3} T_2\right]. \tag{B.15}$$

These effects for both swimmers are rolled into the $\boldsymbol{H}_h$ operator. Note that we can use $\mathbf{G}_{hh}(-\mathbf{x}) = \mathbf{G}_{hh}(\mathbf{x})$ while $\mathbf{v}(-\mathbf{x}) = -\mathbf{v}(\mathbf{x})$ to reduce this computation.

B.2.3 Rigid body motion

The terms containing the force and motion of the first head are given below

$$-\mathcal{M}\cdot\tilde{\mathbf{F}}_1 - \mathbf{I}\cdot\mathbf{U}_1 \tag{B.16}$$

where $\mathbf{I}$ a 3×3 matrix and

$$\mathcal{M} = \begin{pmatrix} \mathcal{M}^t & 0 & 0 \\ 0 & \mathcal{M}^t & 0 \\ 0 & 0 & \mathcal{M}^\theta \end{pmatrix}. \tag{B.17}$$

For both swimmers these terms are represented by the $\boldsymbol{U}_h$ operator.

B.3 Forces and torques

Finally the each body is force and torque free, for example for swimmer 1 we write,

$$\langle \mathbf{f}_1 \rangle + \mathbf{F}_1 = \mathbf{0}, \tag{B.18}$$

$$\left\langle \tilde{\mathbf{r}}_1^\perp \cdot \mathbf{f}_1 \right\rangle + T_1 = 0. \tag{B.19}$$

While for both swimmers together we write $\boldsymbol{F}\cdot\boldsymbol{a} = \mathbf{0}$.

Appendix C

Droplet perturbation formulation

To satisfy the requirements on the functions F and G we expand them in a quarter range basis as

$$F(t,\phi) = \sum_{m,n} A_{m,n} \cos(m\phi) \sin\left(\frac{n\pi}{2}T\right), \tag{C.1}$$

$$G(t,\phi) = \sum_{m,n} B_{m,n} \cos(m\phi) \sin\left(\frac{n\pi}{2}T\right), \tag{C.2}$$

where n is odd and $T = (t - t_1)/\Delta t$.

Using the above definitions of F and G in Eq. (C.11) we obtain

$$\sum_n (-1)^{\frac{n-1}{2}} B_{m,n} = \sum_n (-1)^{\frac{n-1}{2}} A_{m,n} \tan\chi. \tag{C.3}$$

Unlike the analysis in Russo and Steen [97] we cannot use normal perturbations with zero magnitude at the endpoints, as we wish the droplet to be able to have a variable contact point on the upper surface (fixed contact angle condition). However, as shown in Ref. [97], the lowest modes are the ones with the largest increase in surface energy, therefore in order to establish an upper bound on the energy at the critical point we restrict our analysis to the lowest two modes in t and ϕ.

We first consider the case $\chi = 0$, then generalize. With Eq. (C.3) we have $B_{m,1} = B_{m,3}$. The boundary condition places no restriction on g and hence we let $A_{m,3} = 0$. As the surface energy is nonlinear in the shape perturbations, different modes couple and we must be careful in our selection of allowed perturbation shape. While we cannot make the perturbations normal to the shape everywhere, we

impose a related constraint by letting $B_{m,1} = \alpha A_{m,1}$, where α is a free parameter. This restriction on the shapes reduces the unknown coefficients by one to facilitate the analytical calculation, while the free parameter allows some flexibility on the shape of the perturbations, and we tune its value so as to give the earliest possible instability. Because our choice for the space of allowed perturbations may not optimally minimize the surface energy, our analysis is thus only able to derive an upper bound for the stability limit. However, as we will show, this upper bound will coincide with the lower bound, when $\chi = 0$. With these assumptions, our perturbations now take the form

$$F(t, \phi) = (A_{01} + A_{11} \cos \phi) f(t), \tag{C.4}$$

$$G(t, \phi) = (A_{01} + A_{11} \cos \phi) g(t), \tag{C.5}$$

where

$$f(t) = \sin\left(\frac{\pi}{2} T\right), \tag{C.6}$$

$$g(t) = \alpha \left[\sin\left(\frac{\pi}{2} T\right) + \sin\left(\frac{3\pi}{2} T\right)\right]. \tag{C.7}$$

For a general value of $\chi \neq 0$, we can rotate our perturbations to the χ plane $[f', g']^T = \mathbf{R}_\chi [f, g]^T$ where $\mathbf{R}_\chi$ is a two-dimensional rotation operator of angle χ. Hence, for all χ, we may write

$$f(t) = \left[(\cos \chi - \alpha \sin \chi) \sin\left(\frac{\pi}{2} T\right) - \alpha \sin \chi \sin\left(\frac{3\pi}{2} T\right)\right], \tag{C.8}$$

$$g(t) = \left[(\alpha \cos \chi + \sin \chi) \sin\left(\frac{\pi}{2} T\right) + \alpha \cos \chi \sin\left(\frac{3\pi}{2} T\right)\right]. \tag{C.9}$$

We see that $G_2 = F_2 \tan \chi$ for all α.

We require the asymmetric shapes to satisfy the contact angle condition at t_2 and hence $\dot{Z}_2 = \dot{R}_2 \tan(\theta + \chi)$ which leads directly to

$$\dot{G}_2 = \dot{F}_2 \tan(\theta + \chi). \tag{C.10}$$

Eq. (C.10) merely states that our asymmetric perturbations must preserve the slope imposed by the contact angle at t_2. To satisfy this for all θ and χ we set $\dot{F}_2 = \dot{G}_2 = 0$. Furthermore we require $F_1 = G_1 = 0$ so that the droplet remains

pinned at t_1. Additionally, our perturbations must be directed along the surface at the upper bound and hence we need

$$G_2 = F_2 \tan\chi. \tag{C.11}$$

We now expand $F = \sum \epsilon^j F^{(j)}$ and $G = \sum \epsilon^j G^{(j)}$ where ϵ is a small dimensionless parameter. We must ensure our perturbations, order by order, conserve volume

$$V_l = \frac{1}{2}\int_{t_1}^{t_2}\int_0^{2\pi} R^2 \dot{Z} dt d\phi - \frac{1}{6}\tan\chi \int_0^{2\pi} R_2^3 d\phi, \tag{C.12}$$

where the second term in Eq. (C.12) takes into account the inner cone. Expanding and subtracting off the unperturbed case we get to leading order

$$\Delta V_l = \epsilon\pi A_{01}^{(1)}\left[\int_{t_1}^{t_2} r\left(r\dot{g} + 2f\dot{z}\right) dt - f_2 r_2^2 \tan\chi\right] = 0, \tag{C.13}$$

so $A_{01}^{(1)} = 0$. The $\mathcal{O}(\epsilon^2)$ term yields the following relationship

$$A_{01}^{(2)} = -\left(A_{11}^{(1)}\right)^2 \frac{\int_{t_1}^{t_2} f\left(2r\dot{g} + f\dot{z}\right) dt - \frac{1}{2} f_2^2 r_2 \tan\chi}{2\int_{t_1}^{t_2} r\left(r\dot{g} + 2f\dot{z}\right) dt - f_2 r_2^2 \tan\chi}, \tag{C.14}$$

hence with $A_{01}^{(2)} = -\left(A_{11}^{(1)}\right)^2 I$, where I is the quotient in Eq. (C.14), volume is conserved to order $\mathcal{O}(\epsilon^2)$.

The perturbed surface energy is given by

$$\begin{aligned} E =& \gamma \int_{t_1}^{t_2}\int_0^{2\pi} \left[R^2(\dot{R}^2 + \dot{Z}^2) + (R_\phi \dot{Z} - \dot{R} Z_\phi)^2\right]^{1/2} dt d\phi \\ & - \frac{\gamma\cos\theta}{2\cos\chi}\int_0^{2\pi} R_2^2 d\phi. \end{aligned} \tag{C.15}$$

Expanding the integral and subtracting off the axisymmetric contribution, the leading order term of the difference is given by

$$\begin{aligned} \frac{\Delta E}{\epsilon^2\pi\gamma\left(A_{11}^{(1)}\right)^2} =& \int_{t_1}^{t_2}\Big\{ -2Ifv - \frac{rw^2}{2v^3} + \frac{1}{2rv}\Big(2rw(f - 2Ir) \\ & + r^2\left(\dot{f}^2 + \dot{g}^2\right) + (g\dot{r} - f\dot{z})^2\Big)\Big\} \\ & - \frac{1}{2}\frac{\cos\theta}{\cos\chi} f_2(f_2 - 4Ir_2), \end{aligned} \tag{C.16}$$

where

$$v(t) = \sqrt{\dot{r}^2 + \dot{z}^2}, \tag{C.17}$$

$$w(t) = \dot{f}\dot{r} + \dot{g}\dot{z}. \tag{C.18}$$

Note from Eq. (C.16) that our marginal stability curve will be independent of γ and A_{11}^2. We are interested in all outward bulging shapes, nodoids, and hence we check all $\Omega \in [\pi/2, \pi)$.

Bibliography

[1] Arkady Pikovsky, Michael Rosenblum, and Jurgen Kurths. *Synchronization: A Universal Concept in Nonlinear Science*. Cambridge University Press, 2002.

[2] R. E. Mirollo and S. H. Strogatz. Synchronization of pulse-coupled biological oscillators. *SIAM J. Appl. Math.*, 50:1645–1662, 1990.

[3] J. B. Buck. Synchronous rhythmic flashing of fireflies. *Q. Rev. Biol.*, 13:301–314, 1938.

[4] D. M. Woolley, R. F. Crockett, W. D. I. Groom, and S. G. Revell. A study of synchronisation between the flagella of bull spermatozoa, with related observations. *J. Exp. Biol.*, 212:2215–2223, 2009.

[5] F. Hayashi. Sperm co-operation in the fishfly, parachauliodes japonicus. *Functional Ecology*, 12:347–350, 1998.

[6] I. H. Riedel, K. Kruse, and J. Howard. A self-organized vortex array of hydrodynamically entrained sperm cells. *Science*, 309:300–303, 2005.

[7] Y. Yang, J. Elgeti, and G. Gompper. Cooperation of sperm in two dimensions: Synchronization, attraction, and aggregation through hydrodynamic interactions. *Phys. Rev. E*, 78:061903, 2008.

[8] J. Lighthill. Flagellar hydrodynamics: The John von Neumann lecture, 1975. *SIAM Rev.*, 18:161–230, 1976.

[9] C. Brennen and H. Winet. Fluid mechanics of propulsion by cilia and flagella. *Annu. Rev. Fluid Mech.*, 9:339–398, 1977.

[10] E. Lauga and T. R. Powers. The hydrodynamics of swimming microorganisms. *Rep. Prog. Phys.*, 72:096601, 2009.

[11] H D Moore and D A Taggart. Sperm pairing in the opossum increases the efficiency of sperm movement in a viscous environment. *Biol. Reprod.*, 52:947–953, 1995.

[12] Y. Kuramoto. *International Symposium on Mathematical Problems in Theoretical Physics, Lecture Notes in Physics Vol. 39, edited by H. Araki.* Springer-Verlag, Berlin, 1975.

[13] G. I. Taylor. Analysis of the swimming of microscopic organisms. *Proc. R. Soc. Lond. A*, 209:447–461, 1951.

[14] L. J. Fauci. Interaction of oscillating filaments - A computational study. *J. Comput. Phys.*, 86:294–313, 1990.

[15] L. J. Fauci and A. McDonald. Sperm motility in the presence of boundaries. *Bull. Math. Biol.*, 57:679–699, 1995.

[16] J. R. Blake and M. A. Sleigh. Mechanics of ciliary locomotion. *Biol. Rev.*, 49:85–125, 1975.

[17] S. Gueron, K. Levit-Gurevich, N. Liron, and J. J. Blum. Cilia internal mechanism and metachronal coordination as the result of hydrodynamical coupling. *Proc. Natl. Acad. Sci. U.S.A.*, 94:6001–6006, 1997.

[18] M. Cosentino Lagomarsino, P. Jona, and B. Bassetti. Metachronal waves for deterministic switching two-state oscillators with hydrodynamic interaction. *Phys. Rev. E*, 68:021908, 2003.

[19] P. Lenz and A. Ryskin. Collective effects in ciliar arrays. *Phys. Biol.*, 3:285, 2006.

[20] A. Vilfan and F. Jülicher. Hydrodynamic flow patterns and synchronization of beating cilia. *Phys. Rev. Lett.*, 96:058102, 2006.

[21] R. E. Goldstein, M. Polin, and I. Tuval. Noise and synchronization in pairs of beating eukaryotic flagella. *Phys. Rev. Lett.*, 103:168103, 2009.

[22] R M Macnab. Bacterial flagella rotating in bundles: A study in helical geometry. *Proc. Natl. Acad. Sci. U.S.A.*, 74:221–225, 1977.

[23] L. Turner, W. S. Ryu, and H. C. Berg. Real-time imaging of fluorescent flagellar filaments. *J. Bacteriol.*, 182:2793–2801, 2000.

[24] H. Flores, E. Lobaton, S. Méndez-Diez, S. Tlupova, and R. Cortez. A study of bacterial flagellar bundling. *Bull. Math. Biol.*, 67:137–168, 2005.

[25] G. J. Elfring and E. Lauga. Hydrodynamic phase locking of swimming microorganisms. *Phys. Rev. Lett.*, 103:088101, 2009.

[26] M. Kim and T. R. Powers. Hydrodynamic interactions between rotating helices. *Phys. Rev. E*, 69:061910, 2004.

[27] C. M. Pooley, G. P. Alexander, and J. M. Yeomans. Hydrodynamic interaction between two swimmers at low Reynolds number. *Phys. Rev. Lett.*, 99:228103, 2007.

[28] V. B. Putz and J. M. Yeomans. Hydrodynamic synchronisation of model microswimmers. *J. Stat. Phys.*, 137:13, 2009.

[29] G. J. Elfring, O. S. Pak, and E. Lauga. Two-dimensional flagellar synchronization in viscoelastic fluids. *J. Fluid Mech.*, 646:505–515, 2010.

[30] R. Rikmenspoel. Tail movement of bull spermatozoa: Observations and model calculations. *Biophys. J.*, 5:365–392, 1965.

[31] J. Lighthill. *Mathematical Biofluiddynamics*. SIAM, Philadelphia, 1975.

[32] S. Childress. *Mechanics of Swimming and Flying*. Cambridge University Press, 1981.

[33] J. Wilkening and A. E. Hosoi. Shape optimization of a sheet swimming over a thin liquid layer. *J. Fluid Mech,*, 601:25–61, 2008.

[34] J. Wilkening. Practical error estimates for Reynolds' lubrication approximation and its higher order corrections. *SIAM J. Math. Anal.*, 41:588–630, 2009.

[35] B. Chan, N. J. Balmforth, and A. E. Hosoi. Building a better snail: Lubrication and adhesive locomotion. *Phys. Fluids*, 17:113101, 2005.

[36] C. Pozrikidis. A study of peristaltic flow. *J. Fluid Mech.*, 180:515–527, 1987.

[37] J Happel and H Brenner. *Low Reynolds Number Hydrodynamics*. Prentice-Hall, Inc., 1965.

[38] C. Pozrikidis. *Boundary Integral and Singularity Methods for Linearized Viscous Flow*. Cambridge University Press, 1992.

[39] C. Pozrikidis. Creeping flow in two-dimensional channels. *J. Fluid Mech.*, 180:495–514, 1987.

[40] Jonathan J. L. Higdon. Stokes flow in arbitrary two-dimensional domains: Shear flow over ridges and cavities. *J. Fluid Mech.*, 159:195–226, 1985.

[41] Saverio E. Spagnolie and Eric Lauga. The optimal elastic flagellum. *Physics of Fluids*, 22:031901, 2010.

[42] T. S. Yu, E. Lauga, and A. E. Hosoi. Experimental investigations of elastic tail propulsion at low Reynolds number. *Phys. Fluids*, 18:091701, 2006.

[43] R. G. Cox. The motion of long slender bodies in a viscous fluid part 1. general theory. *J. Fluid Mech.*, 44:791–810, 1970.

[44] G. K. Batchelor. Slender-body theory for particles of arbitrary cross-section in stokes flow. *J. Fluid Mech.*, 44:419–440, 1970.

[45] Joseph B. Keller and Sol I. Rubinow. Slender-body theory for slow viscous flow. *J. Fluid Mech.*, 75:705–714, 1976.

[46] Robert E. Johnson. An improved slender-body theory for stokes flow. *J. Fluid Mech.*, 99:411–431, 1980.

[47] Thomas Götz. *Interactions of fibers and flows: asymptotics, theory and numerics*. Ph.D. Thesis, University of Kaiserslautern, Germany, 2000.

[48] Anna-Karin Tornberg and Katarina Gustavsson. A numerical method for simulations of rigid fiber suspensions. *J. Comput. Phys.*, 215:172 – 196, 2006.

[49] J F Brady and G Bossis. Stokesian dynamics. *Annu. Rev. Fluid Mech.*, 20(1):111–157, 1988.

[50] James W. Swan, John F. Brady, Rachel S. Moore, and ChE 174. Modeling hydrodynamic self-propulsion with stokesian dynamics. or teaching stokesian dynamics to swim. *Phys. Fluids*, 23:071901, 2011.

[51] D.C. Guell, H. Brenner, R.B. Frankel, and H. Hartman. Hydrodynamic forces and band formation in swimming magnetotactic bacteria. *J. of Theor. Biol.*, 135:525 – 542, 1988.

[52] I. H. Riedel-Kruse, A. Hilfinger, J. Howard, and F. Jülicher. How molecular motors shape the flagellar beat. *HFSP J.*, 1:192–208, 2007.

[53] M. Argentina, J. Skotheim, and L. Mahadevan. Settling and swimming of flexible fluid-lubricated foils. *Phys. Rev. Lett.*, 99:224503, 2007.

[54] N. J. Balmforth, D. Coombs, and S. Pachmann. Microelastohydrodynamics of Swimming Organisms Near Solid Boundaries in Complex Fluids. *Q.J. Mechanics Appl. Math.*, 63:267–294, 2010.

[55] A. E. Hosoi and L. Mahadevan. Peeling, healing, and bursting in a lubricated elastic sheet. *Phys. Rev. Lett.*, 93:137802, 2004.

[56] E.M. Purcell. Life at low Reynolds number. *Am. J. Phys.*, 45:11, 1977.

[57] K. E. Machin. Wave propagation along flagella. *J. Exp. Biol.*, 35:796–806, 1958.

[58] C. H. Wiggins and R. E. Goldstein. Flexive and propulsive dynamics of elastica at low Reynolds number. *Phys. Rev. Lett.*, 80:3879–3882, 1998.

[59] E. Lauga. Propulsion in a viscoelastic fluid. *Phys. Fluids*, 19:083104, 2007.

[60] S. Camalet, F. Jülicher, and J. Prost. Self-organized beating and swimming of internally driven filaments. *Phys. Rev. Lett.*, 82:1590–1593, 1999.

[61] S. Camalet and F. Jülicher. Generic aspects of axonemal beating. *New J. Phys.*, 2:24, 2000.

[62] R. Dreyfus, J. Baudry, M. L. Roper, M. Fermigier, H. A. Stone, and J. Bibette. Microscopic artificial swimmers. *Nature*, 437:862–865, 2005.

[63] M. Reichert and H. Stark. Synchronization of rotating helices by hydrodynamic interactions. *Eur. Phys. J. E*, 17:493–500, 2005.

[64] T. Niedermayer, B. Eckhardt, and P. Lenz. Synchronization, phase locking, and metachronal wave formation in ciliary chains. *Chaos: An Interdisciplinary Journal of Nonlinear Science*, 18:037128, 2008.

[65] B. Qian, H. Jiang, D. A. Gagnon, K. S. Breuer, and T. R. Powers. Minimal model for synchronization induced by hydrodynamic interactions. *Phys. Rev. E*, 80:061919, 2009.

[66] O. Reynolds. On the Theory of Lubrication and Its Application to Mr. Beauchamp Tower's Experiments, Including an Experimental Determination of the Viscosity of Olive Oil. *Phil. Trans. R. Soc. Lond.*, 177:157–234, 1886.

[67] L. D. Landau and E. M. Lifshitz. *Theory of Elasticity: Vol. 7 of Course of Theoretical Physics*. Butterworth-Heineman, 1986.

[68] G. J. Elfring and E. Lauga. Passive hydrodynamic synchronization of two-dimensional swimming cells. *Phys. Fluids*, 23:011902, 2011.

[69] S. S. Suarez and A. A. Pacey. Sperm transport in the female reproductive tract. *Human Reprod. Update*, 12:23–37, 2006.

[70] P. F. Dunn and B. F. Picologlou. Viscoelastic properties of cumulus oophorus. *Biorheol.*, 13:379–384, 1976.

[71] L. J. Fauci and R. Dillon. Biofluidmechanics of reproduction. *Annu. Rev. Fluid Mech.*, 38:371–394, 2006.

[72] T. K. Chaudhury. On swimming in a visco-elastic liquid. *J. Fluid Mech.*, 95:189–197, 1979.

[73] L. D. Sturges. Motion induced by a waving plate. *J. Non-Newtonian Fluid Mech.*, 8:357 – 364, 1981.

[74] G. R. Fulford, D. F. Katz, and R. L. Powell. Swimming of spermatozoa in a linear viscoelastic fluid. *Biorheology*, 35:295–309, 1998.

[75] H. C. Fu, T. R. Powers, and C. W. Wolgemuth. Theory of swimming filaments in viscoelastic media. *Phys. Rev. Lett.*, 99:258101, 2007.

[76] J. G. Oldroyd. On the formulation of rheological equations of state. *Proc. R. Soc. Lond. A*, 200:523–541, 1950.

[77] R. B. Bird, C. F. Curtiss, R. C. Armstrong, and O. Hassager. *Dynamics of Polymeric Liquids*, volume 2. Wiley-Interscience, 2 edition, 1987.

[78] P. Y. Tam, D. F. Katz, and S. A. Berger. Nonlinear viscoelastic properties of cervical mucus. *Biorheol.*, 17:465–478, 1980.

[79] J. E. Drummond. Propulsion by oscillating sheets and tubes in a viscous fluid. *J. Fluid Mech.*, 25:787–793, 1966.

[80] Bin Liu, Thomas R. Powers, and Kenneth S. Breuer. Force-free swimming of a model helical flagellum in viscoelastic fluids. *Proc. Natl. Acad. Sci. U.S.A.*, 108:19516–19520, 2011.

[81] Joseph Teran, Lisa Fauci, and Michael Shelley. Viscoelastic fluid response can increase the speed and efficiency of a free swimmer. *Phys. Rev. Lett.*, 104:038101, Jan 2010.

[82] X. N. Shen and P. E. Arratia. Undulatory swimming in viscoelastic fluids. *Phys. Rev. Lett.*, 106:208101, May 2011.

[83] S. Kim and S. J. Karrila. *Microhydrodynamics: Principles and Selected Applications*. Butterworth-Heineman, 1991.

[84] P.-G. de Gennes, F. Brochard-Wyart, and D. Quéré. *Capillarity and Wetting Phenomena*. Springer Science + Business Media, Inc., New York, 2004.

[85] Y. Pomeau and E. Villermaux. Two hundred years of capillarity research. *Phys. Today*, 59:39–44, 2006.

[86] T. Young. An essay on the cohesion of fluids. *Proc. Roy. Soc.*, 95:65, 1805.

[87] P. S. Laplace. *Traîté de mécanique céleste*, volume 10 (supplement). Courcier, Paris, 1806.

[88] P. G. de Gennes. Wetting: statics and dynamics. *Rev. Mod. Phys.*, 57:827–863, 1985.

[89] D. Quéré. Non-sticking drops. *Rep. Prog. Phys.*, 68(11):2495, 2005.

[90] J. Plateau. *Statique Expérimentale et Théoretique des liquides Soumis et Seules Forces Moléculaires*. Gauthier-Villars, New York, 1873.

[91] L. Rayleigh. On the instability of jets. *Proc. Lond. Math. Soc.*, 10:4–13, 1878.

[92] J. Eggers. Nonlinear dynamics and breakup of free-surface flows. *Rev. Mod. Phys.*, 69:865–930, Jul 1997.

[93] D. H. Michael. Meniscus stability. *Annu. Rev. Fluid Mech.*, 13:189–216, 1981.

[94] W. Howe. *Die Rotations-Flächen*. Ph.D. Thesis, Universität zu Berlin, Germany, 1887.

[95] R. D. Gillette and D. C. Dyson. Stability of fluid interfaces of revolution between equal solid circular plates. *Chem. Eng. J.*, 2:44 – 54, 1971.

[96] R. D. Gillette and D. C. Dyson. Stability of axisymmetric liquid-fluid interfaces towards general disturbances. *Chem. Eng. J.*, 3:196 – 199, 1972.

[97] M. J. Russo and P. H. Steen. Instability of rotund capillary bridges to general disturbances: Experiment and theory. *J. Colloid Interface Sci.*, 113:154 – 163, 1986.

[98] J. Meseguer, L. A. Slobozhanin, and J. M. Perales. A review on the stability of liquid bridges. *Adv. Space Res.*, 16(7):5 – 14, 1995.

[99] B. J. Lowry and P. H. Steen. Capillary surfaces: Stability from families of equilibria with application to the liquid bridge. *Proc. R. Soc. A*, 449(1937):411–439, 1995.

[100] L. A. Slobozhanin, J. Iwan, D. Alexander, and Andrew H. Resnick. Bifurcation of the equilibrium states of a weightless liquid bridge. *Phys. Fluids*, 9(7):1893–1905, 1997.

[101] B. J. Lowry. Modes of nonaxisymmetry in the stability of fixed contact line liquid bridges and drops. *J. Colloid Interface Sci.*, 224:28 – 46, 2000.

[102] G. Bradley and D. Weaire. Instabilities of two liquid drops in contact. *Computing in Science Engineering*, 3:16–21, 2001.

[103] S. Bohn. Bubbles under stress. *Eur. Phys. J. E*, 11:177–189, 2003.

[104] M. A. Fortes, M. E. Rosa, M. F. Vaz, and P. I. C. Teixeira. Mechanical instabilities of bubble clusters between parallel walls. *Eur. Phys. J. E*, 15:395–406, 2004.

[105] A. D. Myshkis, V. G. Babskii, N. D. Kopachevskii, L. A. Slobozhanin, and A. D. Tyuptsov. *Low-gravity fluid mechanics*. Springer-Verlag, New York, 1987.

[106] Peter T. Nagy and G. Paul Neitzel. Failure of thermocapillary-driven permanent nonwetting droplets. *Phys. Fluids*, 21:112106, 2009.

[107] G. Paul Neitzel and Pasquale Dell'Aversana. Noncoalescence and nonwetting behavior of liquids. *Annu. Rev. Fluid Mech.*, 34:267–289, 2002.

[108] P. Dell'Aversana and G.P. Neitzel. Behavior of noncoalescing and nonwetting drops in stable and marginally stable states. *Exp. Fluids*, 36:299–308, 2004.

[109] K. Brakke. The surface evolver. *Exp. Math.*, 1:141–165, 1992.

[110] I. Müller and H. Struchtrup. Inflating a rubber ballon. *Math. Mech. Solids*, 7:569–577, 2002.

[111] L. Bocquet and E. Lauga. A smooth future? *Nat Mater*, 10:334–337, 2011.

[112] K. Brakke. Hessian, eigenvalues, eigenvectors, and stability in the surface evolver, 1999.

[113] G. I. Barenblatt. *Scaling, self-similarity, and intermediate asymptotics*. Cambridge University Press, New York, 1996.